Final Technical Report: Metrology for Fuel Cell Manufacturing

Contract Number: DE-EE0001047

Award Recipient: National Institute of Standards and Technology

DOE Managers: Nancy Garland and Jesse Adams

Subproject #1: Fuel Cell Manufacturing Variability and Its Impact on Performance

Principle Investigator: Eric Stanfield (NIST)

Team Members: James Filliben (NIST), Brian Pries (NIST), Alkan Donmez (NIST), Manny Hahn (NIST, Retired/Deceased), David Bergman (Brookhaven Labs), Tommy Rockward (LANL), Dusan Spernjak (LANL), Rod Borup (LANL), Rangachary Mukundan (LANL), Jeffrey Allen (Michigan Technical University)

Subproject #2: Non-Contact Sensor Evaluation for Bipolar Plate Manufacturing Process Control and Smart Assembly of Fuel Cell Stacks

Principle Investigator: Eric Stanfield (NIST)

Team Members: Bala Muralikrishnan (NIST), Wei Ren (NIST), Dennis Everett (NIST), Ted Doiron (NIST)

Subproject #3: Optical Scatterfield Metrology for Online Catalyst Coating Inspection of PEM Soft Goods

Principle Investigator: Michael Stocker (NIST)

Team Members: Eric Stanfield (NIST), Richard Silver (NIST), Bryan Barnes (NIST), Martin Sohn (NIST), Jing Qin (NIST), Francois Goasmat (NIST), Hui Zhou (NIST), Richard Quintanilha (NIST)

Subproject #1: Fuel Cell Manufacturing Variability and Its Impact on Performance

Executive Summary

This objective of this project was to determine if flow field channel dimensional variability, in a polymer electrolyte fuel cell (PEFC), as a result of typical manufacturing imperfections associated with one step high-speed manufacturing methods (i.e., compression molding, injection molding, and chemical etching) has an impact on the fuel cell performance. Ideally this project would produce engineering data that would be available to PEFC designers when making manufacturing tolerance decisions and to two-phase flow modelers for validation purposes; however these results have not yet been obtained.

This investigation focused specifically on the cathode side due to the two-phase flow issues and it was specific to a triple-channel parallel co-flow serpentine design (i.e. triple-serpentine flow field). The plate material was a carbon-based composite. To minimize cost and experiment complexity, experiments were limited to single cell versus a short-stack design. The dimensional parameters examined included:

- Sidewall straightness
- Variation in channel width
- Bottom straightness (variation in channel depth)
- Vertical sidewall taper (open side of the channel intentionally made wider, resulting with a trapezoidal channel cross-section)

Note that this list of parameters chosen for this study is not all inclusive. The major challenge of this study, which made it best suited for the National Institute of Standards and Technology (NIST), was ensuring that ALL other potential sources of variability were controlled to a negligible level.

Qualitatively, the results of this project suggest that in-channel vertical side wall taper, often an unintentional result of high-speed molding processes, improves water management and fuel cell performance. The results also suggest that the mere existence of the other dimensional parameters such bottom straightness and a variation-in-width on the order of 0.05 mm and 0.1 mm respectively, incorporated in a controlled repetitive pattern as done in this project, further improves fuel cell performance. This is evidenced by the improved performance of the plates exhibiting these characteristics versus the nominal rectangular design with the least amount of variability. Additional work is required for definitive quantification to produce desired engineering data relating performance to the specific individual parameters tested.

Performance differences were observed from the plate variability studies; however they may not be cause for concern. **This suggests that channel dimensional tolerances may be unnecessarily constrained** as the variation tested was equal to and in some cases much greater than the 0.012 mm to 0.05 mm tolerances gleaned from our discussions with industry. The reader is cautioned that this statement is made with the understanding that different operating

conditions, channel design, flow field configurations, and material selections may yield different sensitivities.

Introduction/Background

In December of 2004, NIST together with the Center for Automobile Research (CAR) co-hosted a workshop at NIST aimed at identifying precompetitive manufacturing/measurement problems related to manufacturing of hydrogen technologies. One of the problems identified was that fuel cell bipolar plate manufacturers were being pressured to reduce product costs associated with high-speed fabrication without real engineering tolerance data upon which to make educated quality control inspection decisions. Most plate manufacturers are not the fuel cell designers thus they are saddled with what they felt were "inferred" engineering drawing specifications that they were told could not be altered. This institutional separation between the plate manufacturers and designers combined with the proprietary nature of technical information in this field seems to prevent an environment where trade-offs between tolerances and performance could be assessed to enable cost reduction. Ideally designers and manufacturers should be able to work together to assess the performance impact of less stringent tolerances on particular parameters that if made less stringent would enable cost reduction by reduced inspection and mold replacement intervals and mold fabrication costs while maintaining an acceptable level of performance.

Developing publically available engineering data that related performance to flow field dimensional tolerances is the objective of this project. Initially, this project was proposed and selected for intramural funding through the NIST Advanced Technology Program (ATP). ATP was a NIST Program which funded external projects that were high-risk but high-payoff. ATP also funded "Intramural Projects" that were aimed at developing information/technologies within NIST to support their external project portfolios either directly or indirectly. This project aimed to provide information that would enable fuel cell commercialization as well as develop NIST capabilities to test the performance of fuel cells. ATP's funding of the project over the next two years was less than requested thus the original scope of the project was trimmed and progress was paced accordingly. The DOE Hydrogen and Fuel Cells Program began funding the project in 2008. As originally intended NIST acquired single cell testing equipment and developed a demonstrated competency to test single cell fuel cells, however due to staffing and programmatic changes the single cell performance testing at NIST in support of this project was discontinued and contracted out to Los Alamos National Laboratory (LANL).

Design of Experiments

The intent of this project was to adopt a commercially available single cell fuel cell then fabricate experimental cathode side flow field plates with precise dimensional perturbations in the flow field channels (refer to Figure 1), as prescribed by a statistically based design of experiments. Given the effort that could be invested and the desired outcome, the NIST

Statistical Engineering Division recommended a Fractional Factorial $2^{(n-1)}$ Design of Experiments with center point replication with four factors (n) that would be varied between two levels.

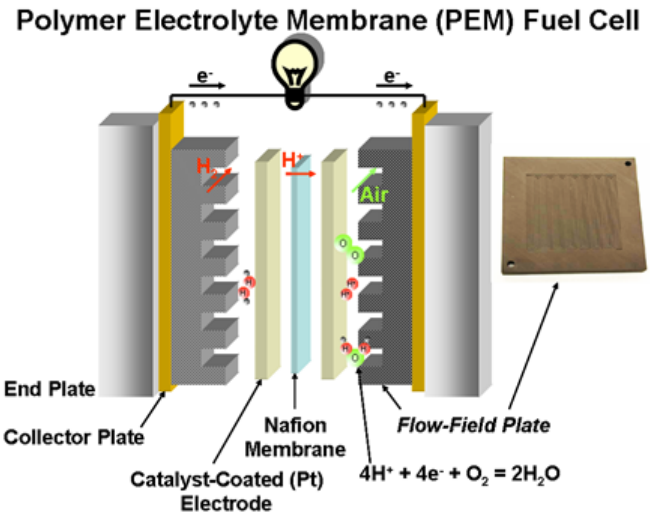

Figure 1

Based on interactions with industry and review of available literature, we identified the following critical fabrication and assembly related parameters:

- Variation in channel width
- Variation in channel depth
- Channel vertical sidewall taper
- Channel sidewall straightness
- Plate and/or in-channel surface finish
- Channel-to-channel alignment (parallelism)
- Plate flatness

At the time, there was no publically available information about the tolerances required for such parameters. Industry interactions suggested tolerances as tight as 0.012 mm up to 0.05 mm. Therefore, in constructing our design of experiments we had to cover a relatively wide range of variations for the chosen parameters. Every experimental cathode plate had to be fabricated, inspected, and performance tested. With this, we down-selected to the following four factors, which were independent of assembly (sealing) issues and believed to have an impact on water management within the cathode channels:

- Sidewall straightness
- Variation in channel width
- Bottom straightness (variation In depth)
- Vertical sidewall taper

The first three parameters were varied along the length of the channel. Perturbations were not incorporated in the turns, only the long straight sections. It is acknowledged that surface finish is probably a critical parameter, but due to the increased fabrication difficulties we chose not to include it.

To further substantiate the variation in these parameters we acquired and dimensionally inspected numerous sample plates fabricated by machining, injection molding, and compression molding (refer to Figure 2).

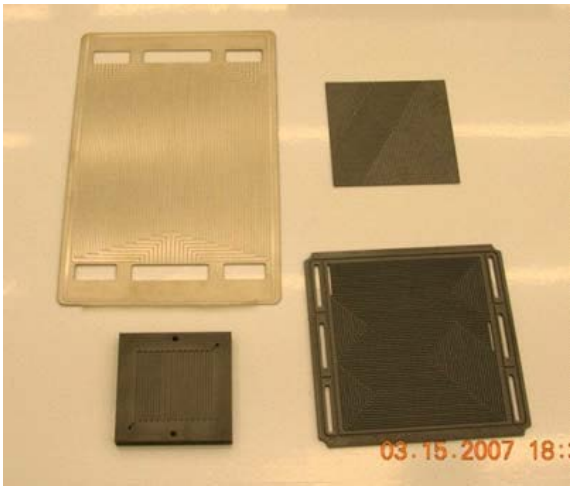

Figure 2 – sample plates fabricated by various methods

The data revealed variations between 0.025 mm and about 0.05 mm which fell within the range previously identified. One of the compression molded bipolar plates inspected was carbon based, very thin, and the channel directions from one side to the other were orthogonal. This produced what appeared to be bleed-through of the channel pattern from one side to the other, visible in the bottom of the channels. Measurements revealed that the unaided visual observation corresponded to a sinusoidal straightness variation in the bottom of the channels along their length with amplitude of 0.05 mm and period of 2 mm. With this being the largest observed in-channel dimensional variation from a very "typical" high-speed fabrication method this was chosen as the upper amplitude limit for straightness with the same 2 mm period. With this, intentional sinusoidal straightness errors were incorporated along both channel sidewalls and the bottom. When the sidewall straightness from one side to the other was in-phase, the mean straightness was 0.05 mm with no variation in width. Alternatively, when the side wall straightness from one side to the other was out-of-phase by 90°, this produced a variation-in-width of 0.100 mm, which resembled a repetitive hour-glass shape.

Recognizing again that high-speed manufacturing methods like compression or injection molding would ultimately be used, we realized that the vertical side walls would never be square to the bottom and that the degree of taper could vary depending on the material and process parameters. Based on studies performed by Owejan [1,2] at the NIST Center for Neutron Research (NCNR) it was already known that cross-section channel shape affected performance, however it was not known if small side wall tapers of 5 or 10 degrees resulting from the molding

process would have a noticeable impact. With the down selection of parameters and limits of variability established, the following design of experiments was developed (Table 1). As noted previously, the dimensional perturbations were only incorporated in the long straight channel sections but not in the U-turn regions of the channels.

	2^{4-1} Fractional Factorial Design with replicated center point (k=4,n=10)							
	Sidewall Straightness	Sidewall Straightness	Bottom Straightness	Sidewall Taper				
	Amplitude	Phase	Amplitude			Sequence		Drawing
Part	*X1*	*X2*	*X3*	*X4*	*Machining*	*Measuring*	*Perf. Testing*	*Cross-Section* *Top*
9	0(25µm)	0(90)	0(25µm)	0(5)	1	1	1	
3	-1(0)	+1(180)	-1(0)	+1(10)	2	2	2	
2	+1(50µm)	-1(0)	-1(0)	+1(10)	3	3	3	
4	+1(50µm)	+1(180)	-1(0)	-1(0)	4	4	4	
8	+1(50µm)	+1(180)	+1(50µm)	+1(10)	5	5	5	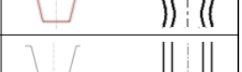
5	-1(0)	-1(0)	+1(50µm)	+1(10)	6	6	6	
7	-1(0)	+1(180)	+1(50µm)	-1(0)	7	7	7	
10	0(25µm)	0(90)	0(25µm)	0(5)	8	8	8	
6	+1(50µm)	-1(0)	+1(50µm)	-1(0)	9	9	9	
1	-1(0)	-1(0)	-1(0)	-1(0)	10	10	10	

Table 1 – Design of Experiments

The reference cell chosen was the Teledyne CH-50 (Figure 3) which is a 50 cm^2 single cell fuel cell design and had been used for intercomparison testing in support of the development of the US Fuel Cell Council's (USFCC) Single Cell Testing Protocol (2004). At the time this was one of the only single cell fuel cells commercially available. This is a triple-channel parallel co-flow serpentine design (triple serpentine) using carbon based flow field plates, stainless steel end plates, and integrated cartridge heaters. Each channel has its own inlet and outlet rather integrated manifold design.

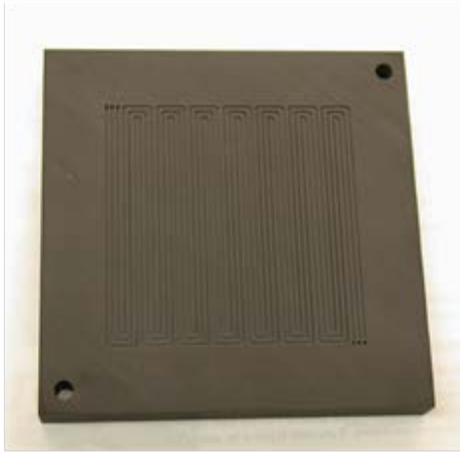

Figure 3 – Teledyne CH-50 Single Cell Fuel Cell (left) and Teledyne carbon-based flow field plate (right)

Reverse Engineering

The NIST Dimensional Metrology Group (DMG) and Manufacturing Metrology Group (MMG) possess unique capabilities which made this project a perfect fit for execution by NIST. These capabilities include high-accuracy micro-feature measurement and error compensated precision machining. For reverse engineering of the reference cell, flow field plates and dimensional evaluation/verification of NIST fabricate experiment cathode flow field plates; DMG used the Mitutoyo UMAP Ultra, a special dual-probe micro-feature coordinate measuring machine (CMM) (Figure 4). With the combination of DMG measurements and an extremely well characterized Makino A55 3-Axis CNC milling machine (Figure 5), MMG was able to compensate for error motions of the machine tool and tool wear often encountered when machining graphite. This compensation helped ensure that unwanted flow field channel dimensional variability across each individual experimental cathode plate and between plates was held to less than 0.01 mm.

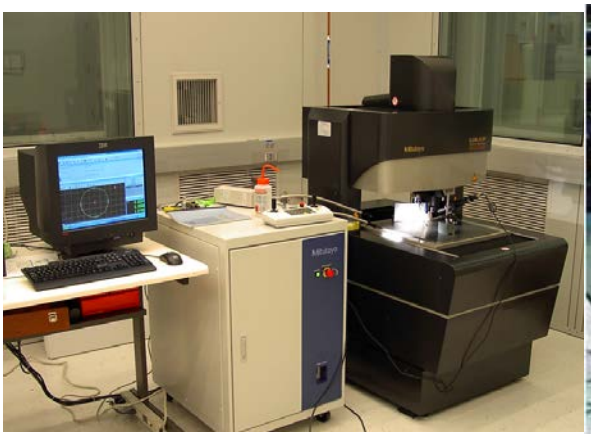

Figure 4 – Micro-Feature CMM

Figure 5 – Makino A55

The reverse engineering of the reference cell plates included determination of size and location of all flow field plate features. Three CH-50 reference single cells were purchased providing six plates for inspection, which in turn yielded enough data to determine intended nominal sizes and locations. Figure 6 shows the reverse engineering process. Nominal channel depth and width was determined to be 0.8 mm and 0.763 mm respectively with an average channel spacing of 1.524 mm.

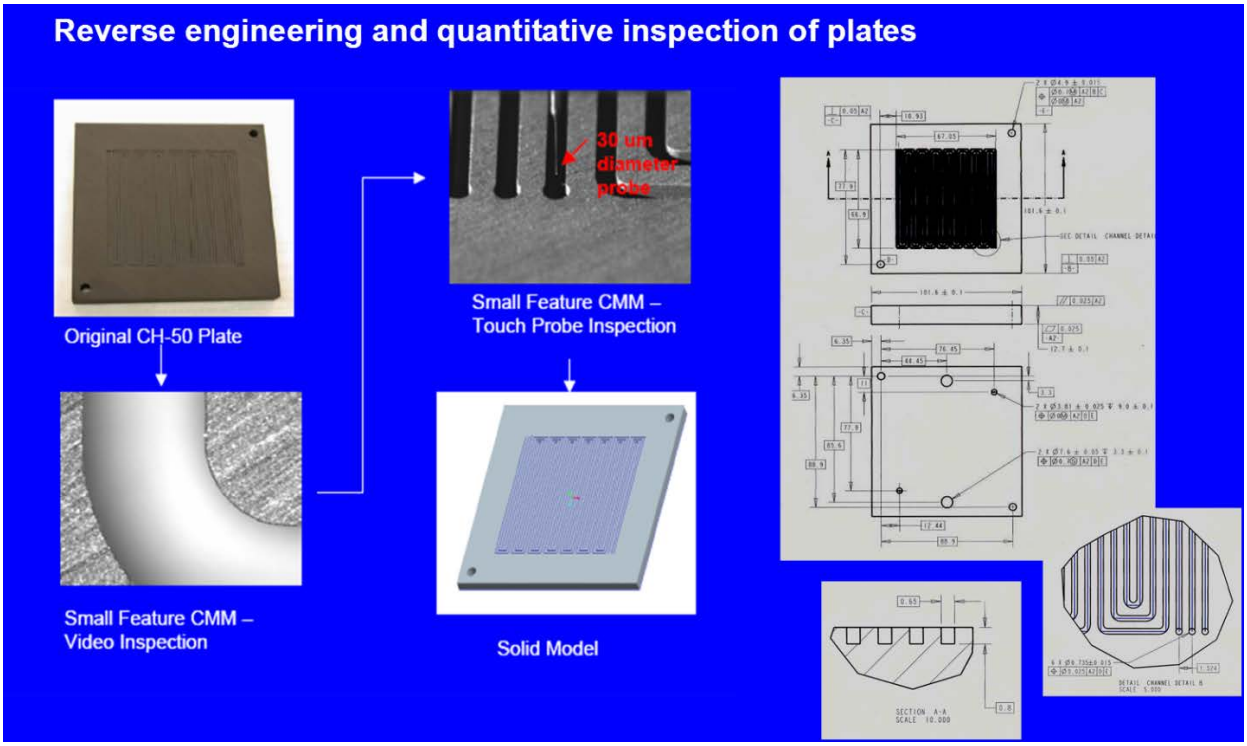

Figure 7 – Reverse Engineering

Fabrication

Using dimensional measurements of the channels of the flow field plates from the originally purchased Teledyne CH-50 cells numerous benchmark measures for fabricating experimental plates were established. These included: variation in average channel width and average channel depth across the plate and between the individual channels, average channel sidewall and bottom straightness, average roughness (Ra) in both the bottom of the channel and the faces of the plates, and overall flatness of the plate faces. The objective was to fabricate experimental plates to equal or better than these measures. In order to do so, we conducted experiments to determine the optimal tool cutter material, machine feeds and speeds, and whether or not cutting coolant was warranted. After numerous iterations with different cutting tools we converged on the use of a carbide cutting end mill, no coolant, 15,000 rpm spindle speed, a 200 mm/min feed rate, and no finish cut. Channels were cut to the full depth of 0.8 mm.

In addition to determining the optimal machining parameters to produce suitable experimental flow field plates, we had to fabricate and verify that the channels had a constant cross-section

throughout the flow field and that the cross-sectional area of tapered channels was the same as the nominally rectangular channels.

Both the Teledyne CH-50 flow field plates and the NIST experimental plates were fabricated from POCO AXF-5QCF, a graphite-based material. This material is graphite impregnated with copper for improved conductivity and furan which makes the material impermeable to gas and liquid. These material compositions are represented by the C and F respectively at the end of the material designation, following the base graphite material notation, 'AXF-5Q'.

Dimensional Verification

Once the fabrication capability was developed and verified, 10 experimental cathode plates were produced and the intended dimensional perturbations were verified using the dual-probe micro-feature CMM. To guarantee a consistent and thorough plate-to-plate evaluation a sampling strategy was developed. As previously mentioned the flow field design has three individual channels arranged in a serpentine design producing what effectively looks like 45 vertical columns. The three-channel vertical pattern repeats 15 times across the plate from left-to-right (Figure 8). The measurement strategy evaluated each of the three channels 4 times, equally spaced across the plate. Each channel was fabricated in its entirety from inlet to outlet using a new cutting tool for each channel where differences in cutting tool diameters were compensated. The sampling strategy provided an approach to monitor tool wear from beginning of the channel to the end by looking at the depth and width as a function of channel and position across the plate, as well as, any remaining channel-to-channel differences. In total, 12 of 45 columns (repeating channels) were measured across the flow field. Refer to Figure 8.

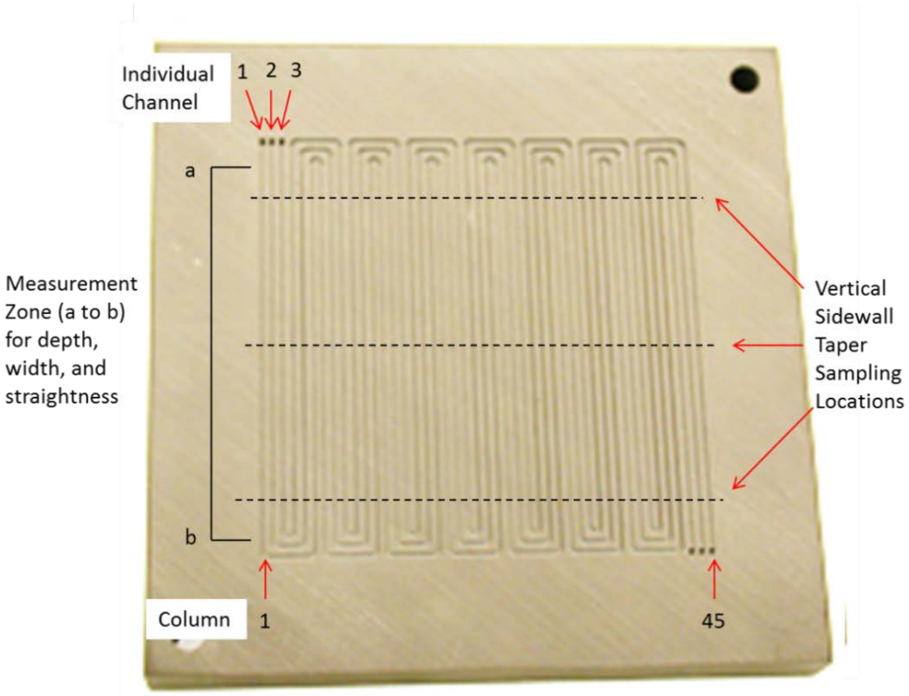

Channel	1	2	3	3	2	1	1	2	3	3	2	1	1	2	3	3	2	1	1	2	3	3	2	1	1	2	3	3	2	1	1	2	3	3	2	1	1	2	3	3	2	1	1	2	3
Column	1	2	3	4	5	6	7	8	9	10	11	12	13	14	15	16	17	18	19	20	21	22	23	24	25	26	27	28	29	30	31	32	33	34	35	36	37	38	39	40	41	42	43	44	45

Figure 8 – Measurement Sampling Strategy and Identification

Channel width, depth, bottom straightness and sidewall straightness for each channel was measured over 60 mm of the 67 mm total length of the flow field, from top-to-bottom (a to b), in Figure 8. The vertical sidewall taper was inspected near the top of the plate, midway, and near the bottom for each sampled channel/column, denoted by the dashed lines in Figure 8. As mentioned previously, the perturbations were only incorporated in the long straight channel sections so the measurement verification did not investigate the turns. Figures 9, 10, 11, and 12 are examples of the dimensional verification results. The material has naturally occurring cavities thus with a 30 um diameter probe it was not uncommon one was observed especially with the very high data density (high values at around 2mm along the channel length, Figs. 9 and 10). These spurious data points on the material side were ignored.

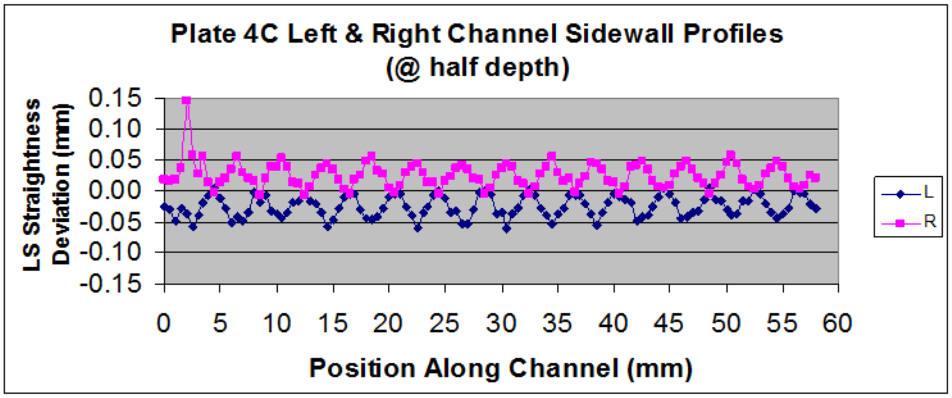

Figure 9 – straightness of both sidewalls, channel width suppressed.

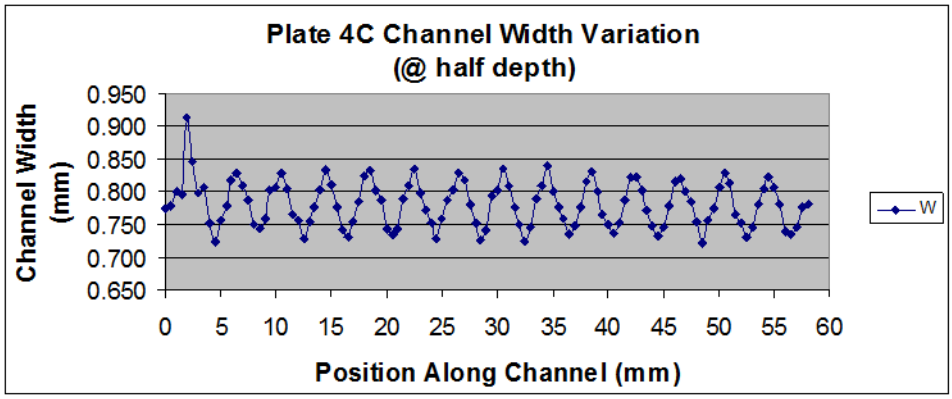

Figure 10 – channel variation in width

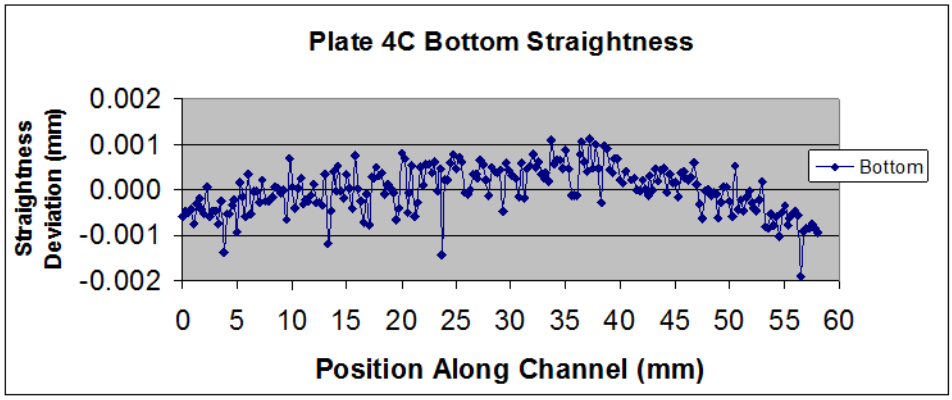

Figure 11 – bottom straightness/variation in depth (absolute depth suppressed)

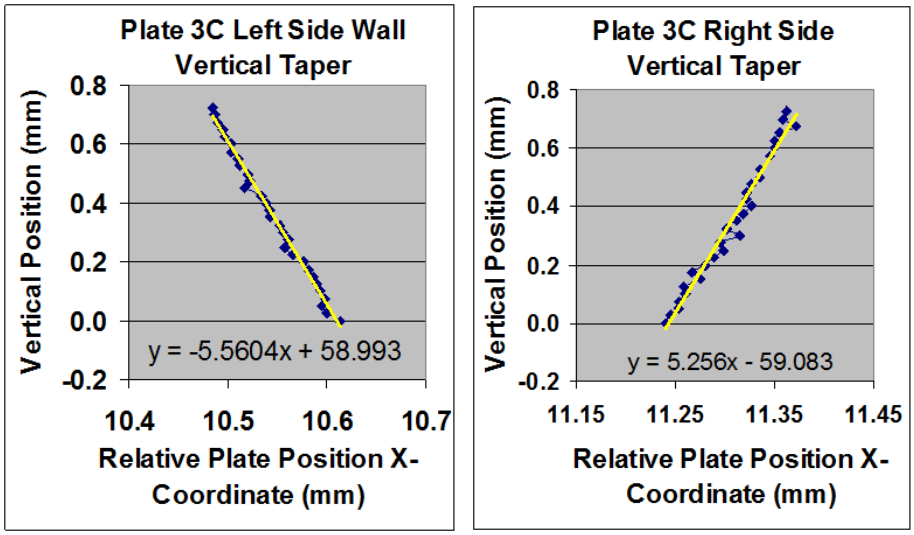

Figure 12 – vertical sidewall taper, 9.99° ± 0.25° (1 standard deviation)

Performance Testing Protocol

Under the original ATP intramural project objectives, NIST was to develop the competence in the area of fuel cell testing. NIST did in fact develop this capability for single cell testing, validated that capability by participating in both the second USFCC single cell round robin and the USFCC Joint Hydrogen Quality Task Force intercomparison, and contributed to the development of the IEC TC 105/241 International Single Cell Testing Protocol 62282-7-1. However, due to institutionally imposed operational constraints and programmatic changes, NIST decided to contract LANL to develop and execute the performance testing protocol. LANL recommended several reference cell changes, prescribed the testing parameters, and recommended inclusion of several ancillary tests as quality control checks.

Reference Single Cell Changes:

LANL recommended several reference cell soft good changes to not only make the cell design more current but also to help highlight the issues to be investigated. To start, LANL recommended changing the gasket material from what came with the CH-50 reference single cell and originally prescribed in the USFCC protocol, due to potential hydrogen permeability issues. Unfortunately, the new gasket material was less compliant making the assembly much less tolerable to flow field plate flatness errors. The less compliant new gasket material combined with the poor flatness of the original Teledyne anode plate was found to be the cause of unacceptable leak rates. To address this, NIST fabricated a replica anode side plate with nominally rectangular cross-section channels with no intentional geometric perturbations, so essentially equivalent to original anode plate, in design, and the experimental cathode plate "1C", in geometric quality. The overall plate flatness of NIST fabricated plates was on the order of 0.01 mm or better versus 0.1 mm for the original CH-50 plates. LANL also prescribed using membrane-electrode assemblies (MEAs) with catalyst loadings lower than the 0.2 mg/cm^2 and 0.4 mg/cm^2 for the anode and cathode respectively so as to be more aligned with current lower loading levels. The carbon-cloth gas diffusion layer (GDL) was changed to a carbon paper. Ultimately LANL used 25 BC GDLs by SGL Carbon and commercial MEA (catalyst-coated membrane) by W.L.Gore with 0.1 mg/cm^2 anode and 0.2 mg/cm^2 cathode Pt catalyst loading. For recent neutron imaging experiments we used the same Gore MEA type but with 0.1/0.1 mg/cm^2 Pt loading.

Performance Testing Protocol Development:

The original testing conditions were chosen to highlight performance differences between plates with the understanding that they may not reflect the most realistic conditions. At the time of development, test conditions were adopted from the March 2007 version of the DOE Cell Component Accelerated Stress Test Protocols for PEFC. The basic performance testing included polarization curves recorded at cell temperature of 80°C and 60°C and at both 50% and 100% RH (relative humidity of the inlet gases). Polarization data were collected in current-control mode with two-minute settling times. Utilization rates were set at 83.3% for H_2 and 50% for air. The outlet pressure (i.e. the backpressure) was 172.4 KPa (25 psi) gauge for both the anode and

cathode side. For MEA quality control LANL incorporated beginning-of-test (BOT) and end-of-test (EOT) diagnostics. Besides polarization curves, tests included cyclic-voltammetry (CV) to measure hydrogen crossover and active catalyst surface area on the cathode side. AC-Impedance measurements (EIS, electrochemical impedance spectra) were also incorporated to investigate cell behavior in the mass-transport limited region (high current).

Similar to our concerns regarding performance variation related to unintentional dimensional variation, NIST and LANL were concerned with unintended variation related to performance testing. With performance testing the concern was variation between results due to inconsistent execution of the testing protocol, testing equipment variability, gas stream contamination, and the primary concern of cell assembly-disassembly. To minimize gas stream contamination, electrolysis-grade hydrogen and air supplied from an oil-less compressor was used.

Given the starting parameters defined, LANL recorded several polarization curves to get an idea of the general performance behavior of the cell for the baseline plate, #1 (Figure 13). Figures 14 (a) and (b) show three CV cycles run at 80°C, H_2/N_2 at 500 sccm, 172.4 KPa (25 psi) gauge back pressure, with a scan rate of 20 mV/s from 0.1 to 1.1 V at 25% RH and 100% RH respectively.

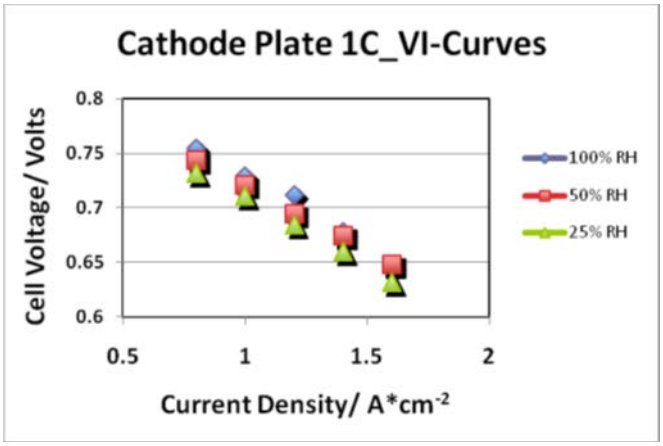

Figure 13 – Reference cell with NIST cathode plate 1C and anode plate 1A at 80°C with 172.4 KPa (25 psi) gauge back pressure.

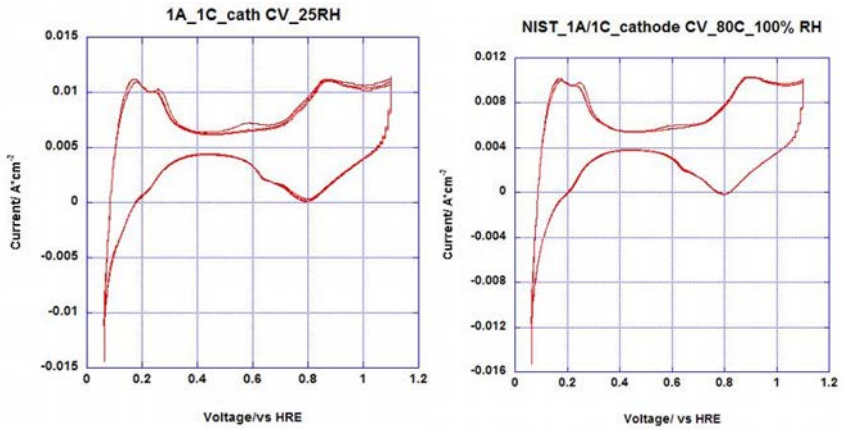

(a) (b)

Figure 14 – CV's at (a) 25% RH and (b) 100% RH

Since the polarization curves in Figure 13 did not show a visible mass transport region, LANL recommended increasing the air utilization rate from 50% to 71% and concluded that the cell would have to be run to higher current densities. By way of a separate repeated assembly-disassembly experiment, LANL quickly determined that the MEA could not be reused from one setup to another to facilitate switching experimental cathode plates. With this, LANL then proposed that it should be possible to still achieve excellent repeatability using a new CCM for each experimental cathode plate assembly, if all required CCMs were cut from the same manufacturer's batch to minimize lot-to-lot variation.

The benchmark for repeatability was based on USFCC intercomparisons where the points on the polarization curve produced by different labs using the same procedure agreed in general to the 5 mV level increasing to twice this in the extreme mass transport region.

After making the recommended changes, testing was repeated as shown in Figure 15. This shows three average reference cell polarization curves where the reference cell was disassembled, MEA replaced with a new one, then reassembled between each. After each disassembly-assembly the cell was first subjected to the standard break-in protocol (repeated voltage cycling), followed by three repeated polarization curves which were then averaged. The results showed excellent repeatability, with the expected increased scattering of the results at high currents due to cathode catalyst layer flooding.

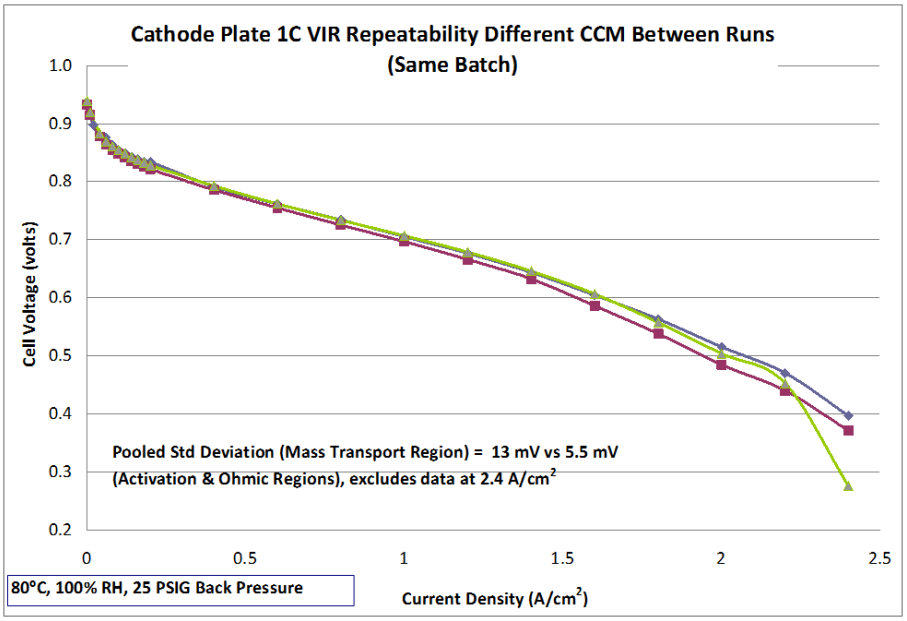

Figure 15 – Repeatability with disassembly/assembly and new CCM between runs

Performance Testing of Experimental Cathode Plates:

With the satisfactory repeatability and confidence, the experimental plates were tested using the same protocol. All plates were run at 80 °C and 172.4 KPa (25 psi) gauge back pressure at 100% RH (Figure 16) and 50% RH (Figure 17). For six of the ten plates the results seem unremarkable but the remainders seem to stand out visually. Specifically, plate 7C is the worst performer while plate 5C seems to be the top performer at both 50% RH and 100% RH. Although Figures 16 and 17 show plate 3C as having noticeably poor performance, this was not repeated during later testing suggesting that the poor performance was most likely due to a damaged MEA. Plate 8C looks to have the best performance at 100% RH, but tails off in comparison to plate 5C at higher current densities and is not a top performer at 50% RH.

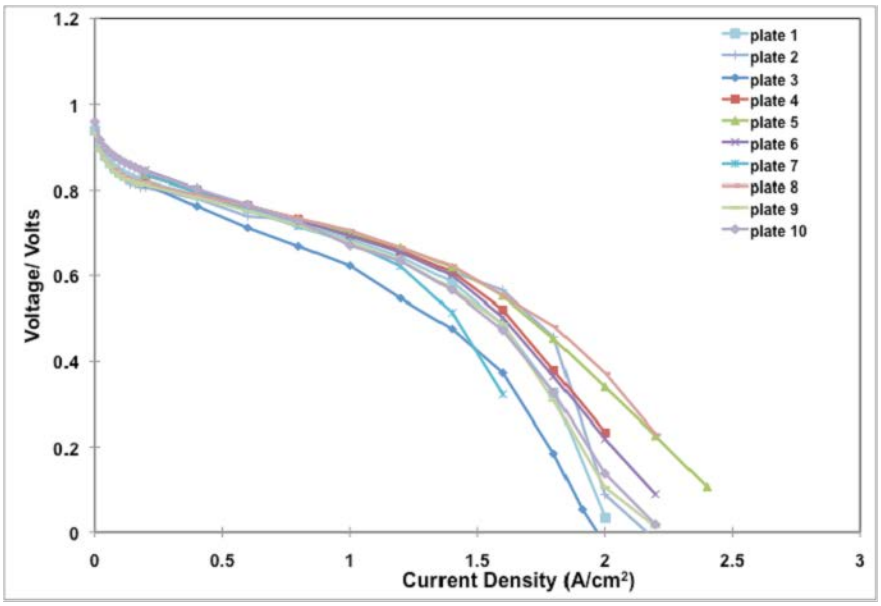

Figure 16 – polarization curves for experimental plates at 80°C and 100% RH

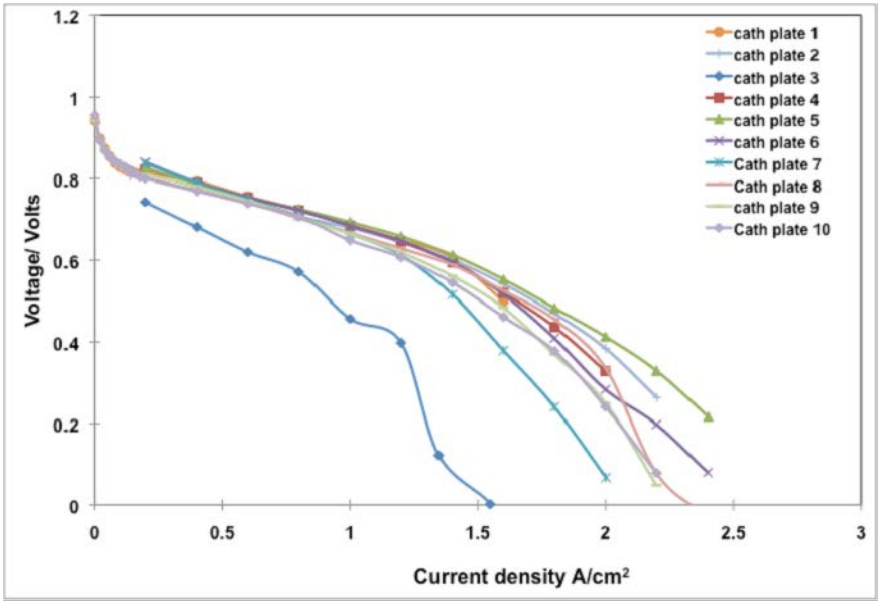

Figure 17 - polarization curves for experimental plates at 80°C and 50% RH

To address a reviewer's concern at the 2010 DOE Annual Merit Review, additional testing was incorporated for a few selected plates to demonstrate that the performance differences also existed at ambient back pressures. Testing was performed on the two worst performers at back pressures of 172.4 KPa (25 psi) and 68.9 KPa (10 psi) gauge as well as ambient. As expected the polarization curves shifted lower with lower back pressures, however the plate-to-plate performance differences remained showing the differences agreed with initial results regardless of the back pressure. Refer to Figure 18 (results are the average of two scans, with increasing and decreasing current).

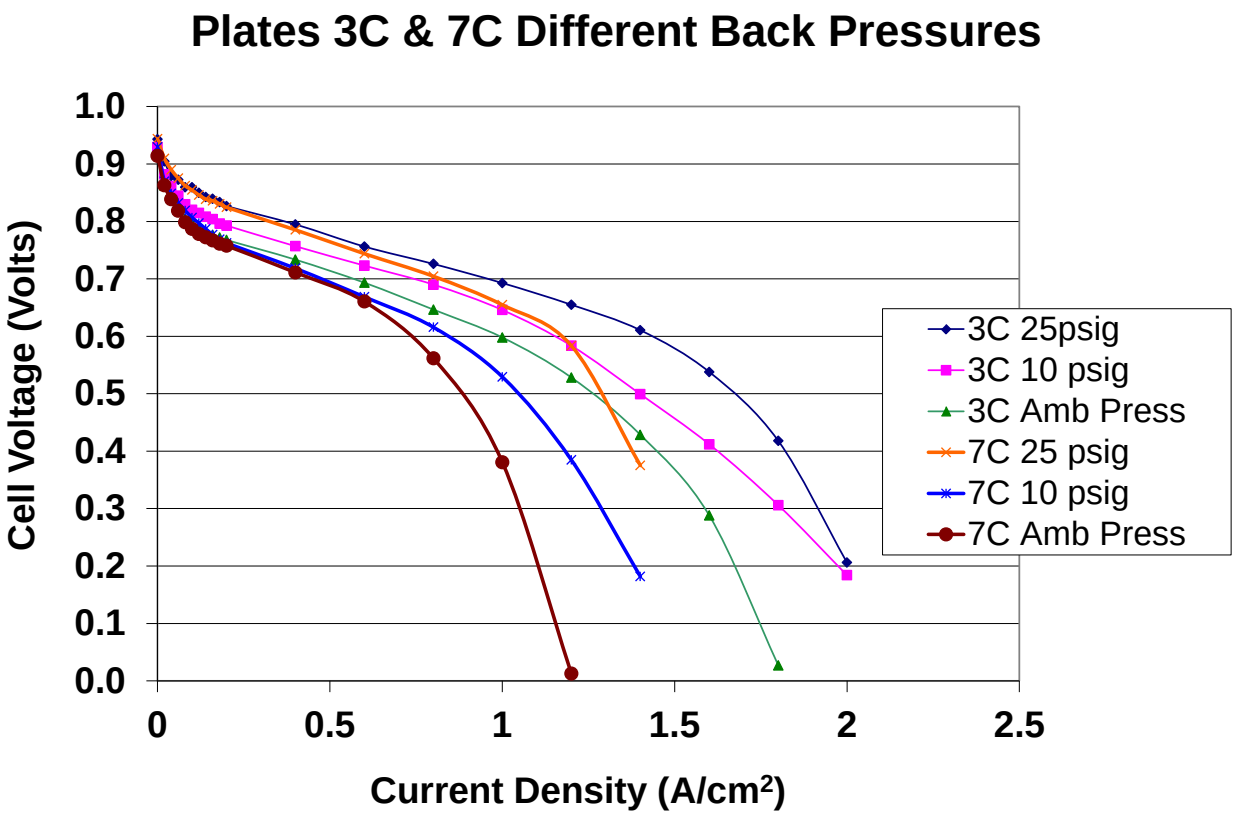

Figure 18 – polarization curves at 80C and 100% RH at various back pressures

Intermediate Conclusions:

A correlation between performance differences and the design of experiments seems apparent, but is based on speculation. The only conclusion that seems clear is the nominal design plate 1C with no intended dimensional variation is not the best performer thus it is believed that the performance differences are tied to experimental factors in some manner. For clarity, without referring back to the DOE chart, the factors were (1) side wall straightness, (2) side wall straightness phase (variation-in-width), (3) bottom straightness (variation-in-depth), and (4) vertical sidewall taper.

To gain further insight, the NIST Statistical Engineering Division performed a statistical analysis of the data but it did not yield statistically significant conclusions yet our statisticians classified them as strongly suggestive. To be statistically conclusive the F-distribution cumulative density function or probability needed to be 95 % or greater for a main factor. Unfortunately due to the fractional-factorial nature of the experiment this statistic could not be determined for the two-factor interactions because of their "confounded" nature. To explain this further in a simple manner, the number of tests was reduced to keep the work to a manageable level as mentioned previously, therefore a potential outcome is that if an interaction is significant then there is not enough data to determine precisely which interaction is indeed the most important. In our

experiment, a two factor interaction was dominate but there was not enough data to determine if the two factor interaction was 1 and 2 or 3 and 4. The ranked order of significant factors and two-factor interactions is shown in Figure 19. It is important to note; (1) 3 and 4 factor interactions were not tested and (2) The "effect" in the table and subsequent plots represent the voltage difference multiplied by 100 to make the whole number results more visual.

Ranked Order

Factor	Effect (V*100)	Rel. Eff %	Fcdf Stat %	
12 + 34	18.59			*
3	16.17	106	82.4	**
1	15.28	101	79.4	**
4	6.02	40	36.1	
14 + 23	-5.67			
2	-3.71	24	22.6	
13 + 24	-2.74			

Figure 19 – statistically ranked order of factors and interactions

Although, the first three results were not statistically significant the main factors were not far off thus the classification of strongly suggestive. Figures 20 and 21 are two different graphical representations of the statistical results. In Figure 20 each factor and interaction has a box plot and the greater the slope, the more significant the factor or interaction is. The confounding for the interactions can be seen by identical plots for three different two-factor interactions. Figure 21 is more intuitive and clearly shows one of the intended characteristics of the design of experiments, in that the experiment included a center replication point to test for consistency. Plates 9 and 10 were identical with all factors set mid-range, performing as expected, with both producing nearly the same output; with an output ranking near the mean relative to the other plates.

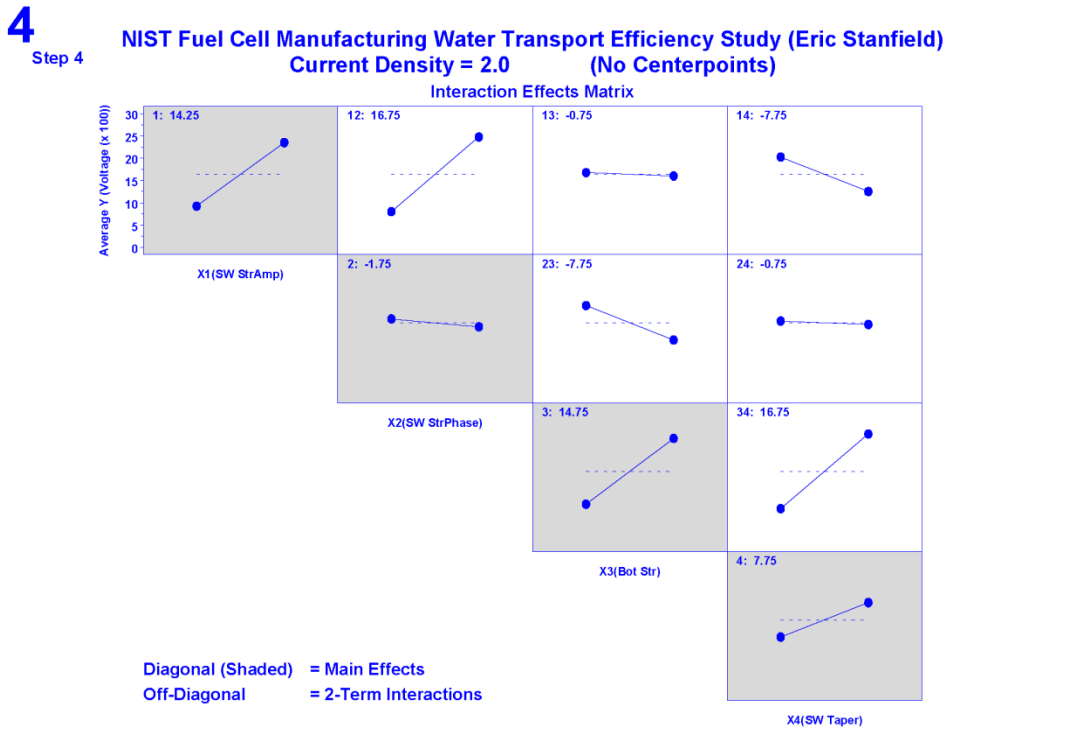

Figure 20 – Interaction Matrix Plot

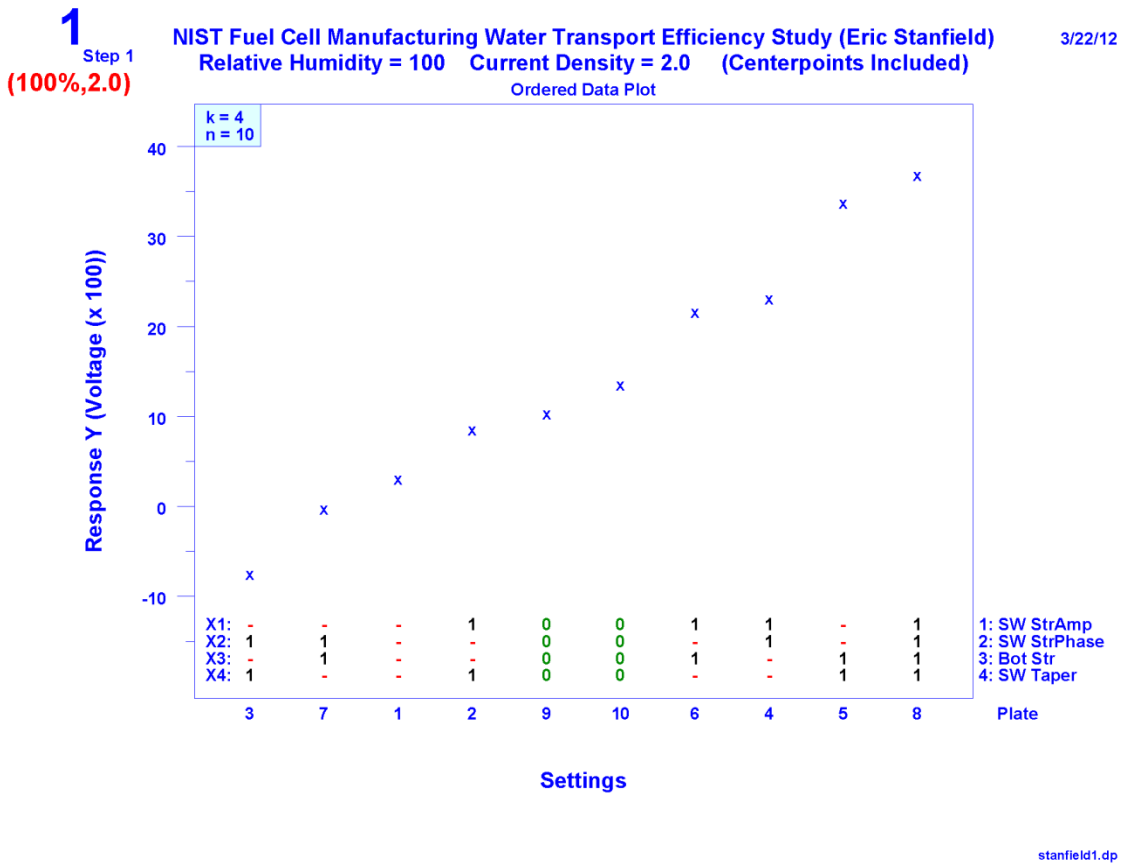

Figure 21 – performance plot voltage (x100) versus plate relative to the DoE (design of experiments)

Further Testing:

At this point without physics based insight any definitive conclusions remained elusive. To gain further understanding we proposed two approaches; (1) obtain a physics-based explanation of the results in relation to the experiment from a fuel cell and two-phase flow expert and (2) obtain visual insight into the water management of the different single cell configurations by means of neutron imaging.

Neutron Imaging and Expert Insight:

In October of 2011, NIST and LANL submitted a proposal to the NIST NCNR for beam time approval to conduct an experiment involving a five plate subset of the original ten experimental cathode plates. The five plates to be tested included the two worst performers (3C and 7C), the nominal design (1C, baseline), and the two best performers (5C and 8C). The experiment involved running polarization curves for each of the experimental plates while simultaneously imaging the water content and distribution within the fuel cell. The imaging experiments would be run by LANL researchers. The NIST NCNR Team approved the proposal with recommendations that involved modifications to the single cell fuel cell and experimental plates to ensure optimal image quality. These modifications included replacing the stainless steel end

plates with ones made from aluminum and refabricating the five experimental cathode plates and one reference anode plate with ones made of a material that did not contain any hydrocarbons. The furan in the composition of the original experimental plates was a hydrocarbon thus would interfere with the imaging of the water.

With the need to replace the original experimental plates, the concern became finding an alternative with nearly the same operational critical material properties of the original plates (i.e. wettability, in-plane and through-plane conductivity). This was critical to ensure correlation with the performance differences identified using the original experimental plates. It was determined that the most suitable approach was to fabricate experimental plates from POCO AXF-5Q material then send these plates back to POCO to have the plate surface sealed using their proprietary "pyrosealing" process. In this process, the surface of naturally porous AXF-5Q graphite is sealed with the same carbon material from which the plate was made. This process could be comparable to nitriding. Sealing the plates is required so the gases (especially hydrogen) would not leak out of the cell through the pores, and so the water from the cell would not penetrate the plate pores and therefore affect the water measurement via neutron imaging. NIST fabricated both aluminum endplates and the five replacement experimental plates. The experimental plates were dimensionally inspected to ensure the intended perturbations were present with the same magnitude of the original experimental plates. The fabrication process had to be resurrected as almost three years had gone by since the originals were produced. The machinability and resulting surface finish quality of the experimental plates made of the POCO AXF-5Q material was nearly identical to the originals made from the POCO AXF-5QCF, however surface wettability differences were still a concern, but this could not be addressed until the plates were pyrosealed by POCO.

Concurrent with these activities, NIST consulted Dr. Jeffrey Allen from Michigan Technological University who was highly recommended based on his two-phase flow expertise and fuel cell work, to aid in the understanding of the performance results. From his review of the performance data and the channel design there was nothing glaringly obvious from a theoretical standpoint that would explain the differences. Based on flow rates and channel dimensions the type of flow within the channel could not be determined without more information about the wettability of the surface. With this, he offered to conduct static contact angle measurements on both the original experimental plates and then again on the alternative material plates after being pyrosealed by POCO. Not only might this help explain the original performance data, but help us determine the consistency between the original and alternative material plates.

Dr. Allen's lab at Michigan Tech has one of the more precise and sophisticated setups for measuring static water contact angle. Their test method involves water drop deposition with precise volume control followed by image acquisition of each drop using a long-distance microscope fitted with a CCD camera. The Laplace curves are fit to each drop profile. These fits are obtained from numerical integration of the Laplace Young equation, which relates the pressure difference that exists across an interface due to interfacial tension and hydrostatic pressure. Dr. Allen and his colleague V. Konduru provided detailed reports for their analysis of both material plates and those reports are considered a part of this final report *(Static Contact Angle Measurements on AXF-5QCF Flow Field, Report No. NIST-2012-06-MichiganTech, 6-28-*

2012 and Static Contact Angle Measurements on AXF-5Q Part #5 Cathode Flow Field, Report No. NIST-2012-08-MichiganTech, 8/21/2012).

For the AXF-5QCF sample, visual inspection and the static contact angle data revealed a very inhomogeneous material. Data from drops placed at multiple locations showed a large variation in water contact angle of 75° to 90°. Refer to Figure 22 for the static contact angle measurement locations and Figures 23a and 23b for images of drops at two different locations showing the observable differences. This was not surprising with the visual observation of light and dark areas. Surface wettability is not only a function of surface roughness but also non-uniform material composition. From the data Dr. Allen's primary concern was that this large contact angle variation could have a significant impact on the movement of liquid water through the channels during fuel cell operations and cause what he termed as "pinning" of the water droplets. Although all plates were made from the same material, the in-channel inhomogeneous pattern "could" be different from plate-to-plate.

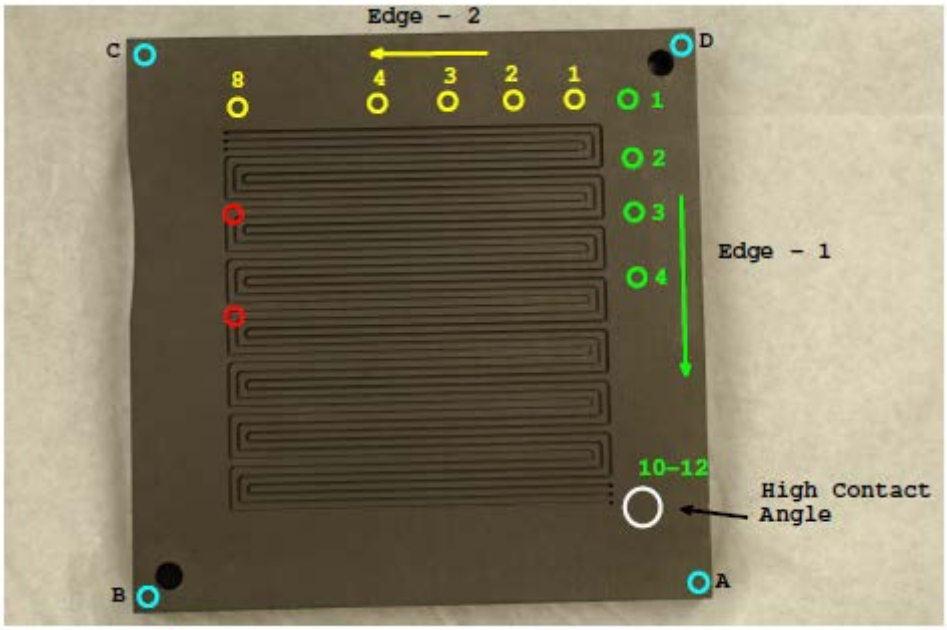

Figure 22 – static contact angle sampling locations for AXF-5QCF sample

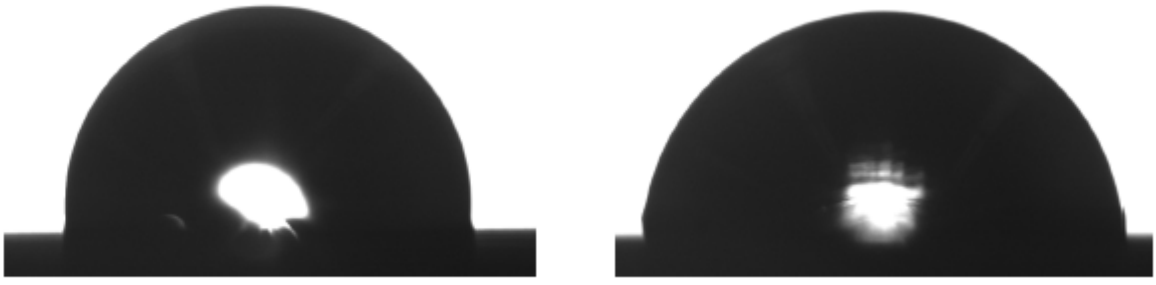

(a) (b)

Figure 23 – (a) profile at location "C" from Figure 22 (b) profile at location "D" from Figure 22

Static contact angle testing of the AXF-5Q plate was delayed because upon receipt of the plates back from POCO there was a significant difference in the visual appearance of the plates. Visual inspection of the plates with the dual-probe micro-feature CMM revealed a very different looking surface with random black spots. With closer inspection these spots appeared to be holes in the surface as they had a depth of approximately 0.1 mm. It almost appeared like the plate had a crust with random inclusions. These spots could be found on the large smooth surfaces of the plate but could not be found within the channels. Because of this significant difference in look, it immediately became a concern that the perturbations were no longer what they were expected to be. To verify, the dimensional inspection using the micro-feature CMM was repeated and surprisingly the perturbations and channel dimensions were indistinguishable from the original to the 0.001 mm level.

From measurements of the pyrosealed AXF-5Q plate a range of 90° to 104° was determined for the static contact angle, which was higher than the original AXF-5QCF sample. Thus the surface of pyrosealed AXF-5Q plates, used for subsequent testing and neutron imaging experiments, is more hydrophobic than the surface of the AXF-5QCF plates, used in the first part of this study. The pyrosealed sample appeared much more uniform than the original AXF-5QCF plates. Refer to Figure 24.

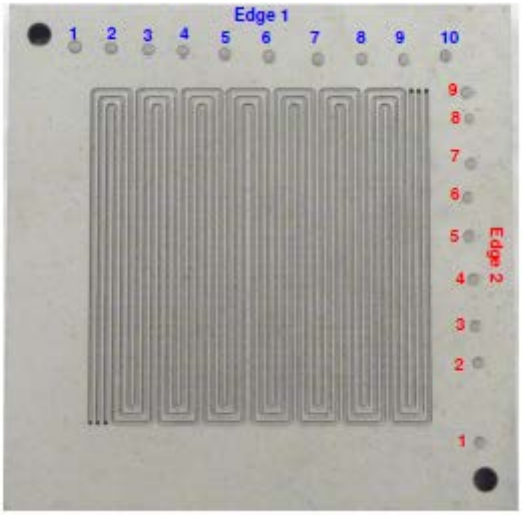

Figure 24 –static contact angle measurement locations for pyrosealed AXF-5Q sample

Figure 24 not only shows the static contact angle measurement location, but also shows a distinct "silver/grey" image which is significantly different than the AXF-5QCF sample. This difference in appearance is the result of the pyrosealing process

Neutron Imaging Experiment with NIST Experimental Plates (August 2013)
Los Alamos National Laboratory (LANL)

Research Team:

Dusan Spernjak
Tommy Rockward
Rod Borup
Rangachary Mukundan

The time allotment for the neutron imaging experiment was such that it was carried out with 3 of the 5 substitute experimental plates; including the worst performer (3C), best performer (5C), and the nominal design (1C). The MEA was a W.L. Gore A510.1/M710.18/C510.1 with 0.1 mg/cm^2 platinum loading on both the anode and cathode side. The cathode loading was reduced from the previous experiments by a factor of 2. The GDL used was an SGL Carbon (SGL25BC) on both sides. Flow rates were 1.2 stoich on the anode side and 1.4 stoich on the cathode side with a minimum 100 sccm on anode side and 250 sccm on the cathode. The back pressure was set to 48.7 KPa (7.1 psi) gauge or 150 kPa (21.8 psi) absolute. The cell was vertical, in a co-flow configuration, with inlets high. Figure 25 shows a neutron radiograph of the dry fuel cell revealing the hardware (channel orientation is the same as in Figure 22).
Compared to the initial hardware materials and design (Figure 3), several modifications were made to accommodate the requirements of neutron imaging:

- End plates were made of Al alloy T6061 instead of stainless steel (safety requirement to reduce the material activation).
- Instead of a single heater in each end plate, located above the central region of the flow field, each end plate had two heaters, placed outside the field of view so as not to obstruct the neutron imaging measurement.
- Pyrosealed AXF-5Q material was used for bipolar plates, instead of AXF-5QCF. AXF-5Q is hydrogen-free material (neutrons are attenuated by hydrogen), and they need to be sealed to prevent gas leakage as well as water penetration into the pores of the unsealed AXF-5Q graphite.

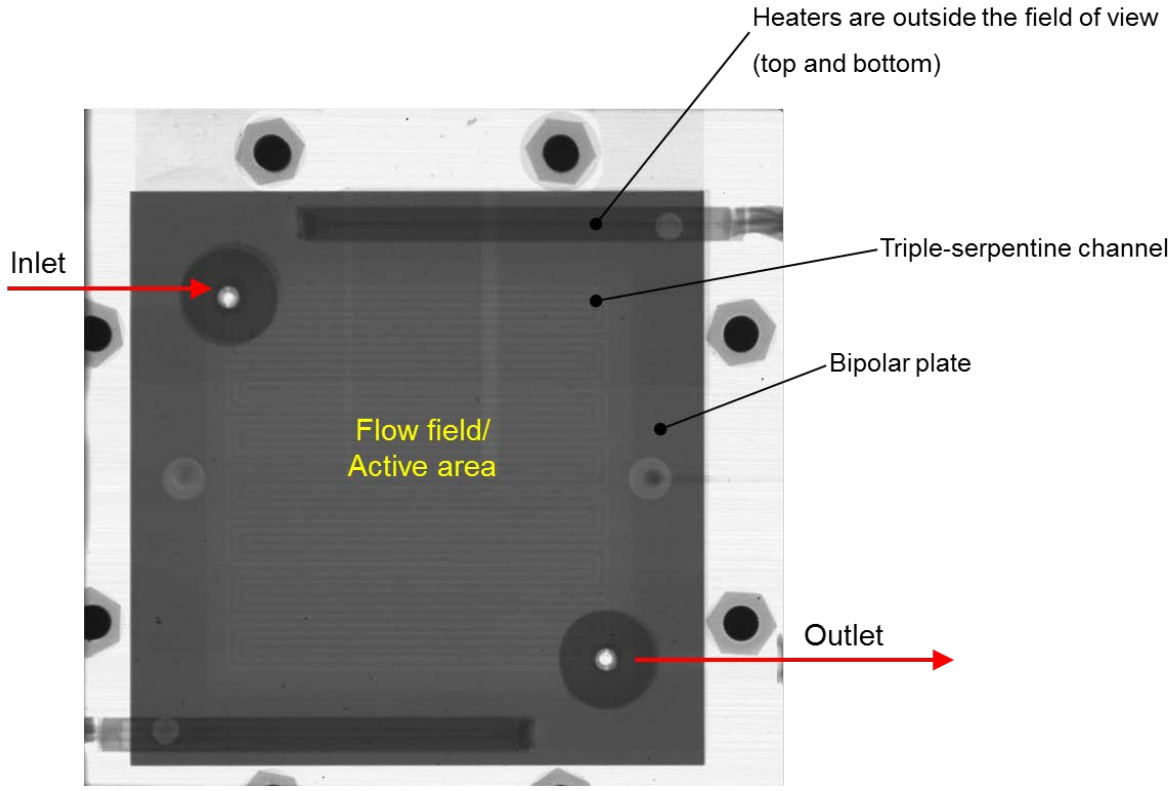

Figure 25 – neutron radiograph of a dry fuel cell showing the hardware configuration

The experiments performed were as follows. Water distribution was recorded in-situ (i.e. with cell operating) at several conditions, at a steady state, after 20-minute operation at fixed current (i.e. fixed water production rate). Second, EIS (electrochemical impedance spectra) were recorded at each steady state to evaluate different loss contributions to the fuel cell performance. In addition, polarization curves were recorded in current-control mode (each polarization curve presented hereafter is an average of two current scans, with increasing and decreasing current). All experiments were performed with identical materials and hardware; only the cathode plates were varied.

Figure 26 displays the processed neutron images showing liquid-water distribution for each of the experimental flow field plates at different current densities (color bar denotes water thickness). Note that the water content from neutron images is integrated in the direction of the cell thickness, hence it is challenging to distinguish between anode and cathode sides as well as between individual cell components (membrane, catalyst layers, gas diffusion layers). Moreover, water residing in the channels (typically on the cathode side) often represents the major portion of the overall water content. The image at 0.4 A/cm2 for Plate 5C (circled in Figure 26), which is expected to be the best performing plate, has higher overall water content than other two plates at the same conditions. This situation at first glance might lead one to believe that with more overall water the performance should be worse than for the other plates but polarization curve data suggests otherwise. Therefore, in addition to measuring the total water content, water content in the channel region is subsequently excluded from calculations in order to estimate

water content under the lands only. This is done by masking the channels in the images processing.

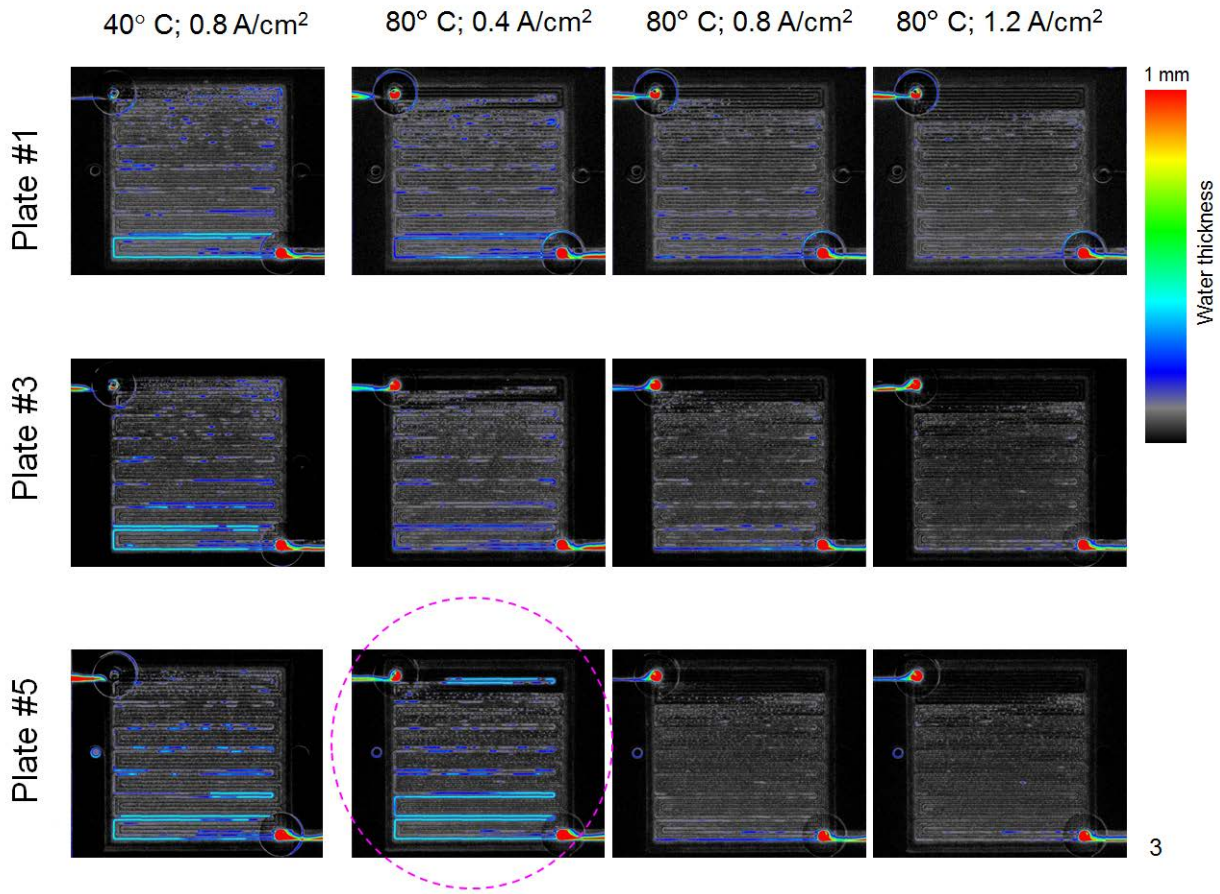

Figure 26 – Liquid water distribution of the fuel cell with different experimental cathode plates at 100% RH: Plate #1 (top row), Plate #3 (middle row), and Plate #5 (bottom row).

An example of masking procedure for Plate 5C at 0.4 A/cm2 (circled in Figure 26) is displayed in Figure 27. Shown side by side are the original unmasked neutron image (left) and the neutron image with masked channels and U-turns (right). The image on the right shows the semi-transparent mask overlaid on top of the original neutron image shown to the left. The images are rotated by 90 degrees and aligned with the plots below that show the average water thickness as a function of pixel location (left-to-right). The water content is averaged in the direction of channels and lands.

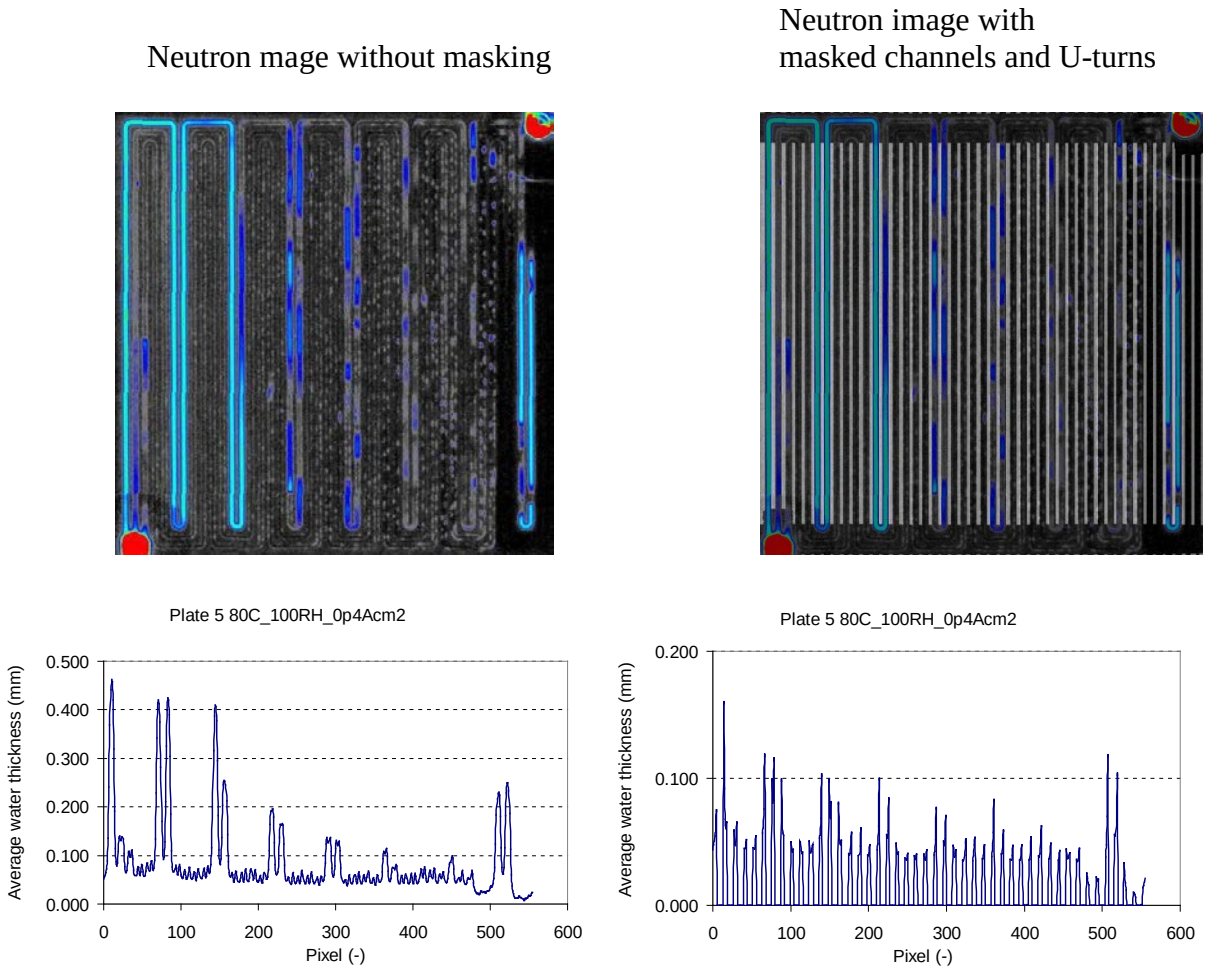

Figure 27 – plate 5C at 80 °C and 100RH at 0.4 A/cm^2: Water content without masking (left) and water content under the lands only (right, with channels masked). Water thickness averaged in the direction of channels and lands.

Figure 28 provides a simplified graphical summary of the total water content (Figure 28a) and the portion of that total water content under the lands only (Figure 28b) for the three plates at three current densities, at 80 °C and 100RH. Comparison of the average water thickness with and without masking confirms that the majority of the water content is in the channels and not trapped under the lands Although the water in the channels often represents the major part of the total water content, water in the channels does not necessarily significantly affect the performance (unless we have severe blockage by water slugs in the channels). More channel water could often mean that the water has been efficiently removed from the gas diffusion layer (GDL) and the catalyst layer (CL), which may result in better performance although the channels are flooded [1,2].

Although plate #1 has more overall water than the other two cathode plates at high currents (Figure 28a), to conclusively evaluate the level of GDL/CL flooding under the lands, for the second graph, Figure 28b, the channels and U-turn regions have been masked and plotted to show the water content under the lands only (i.e. this water is located in anode and cathode GDLs, catalyst layers and the membrane). Plate 1C consistently has more water under the lands, which agrees well with the performance and EIS measurements, to be discussed next.

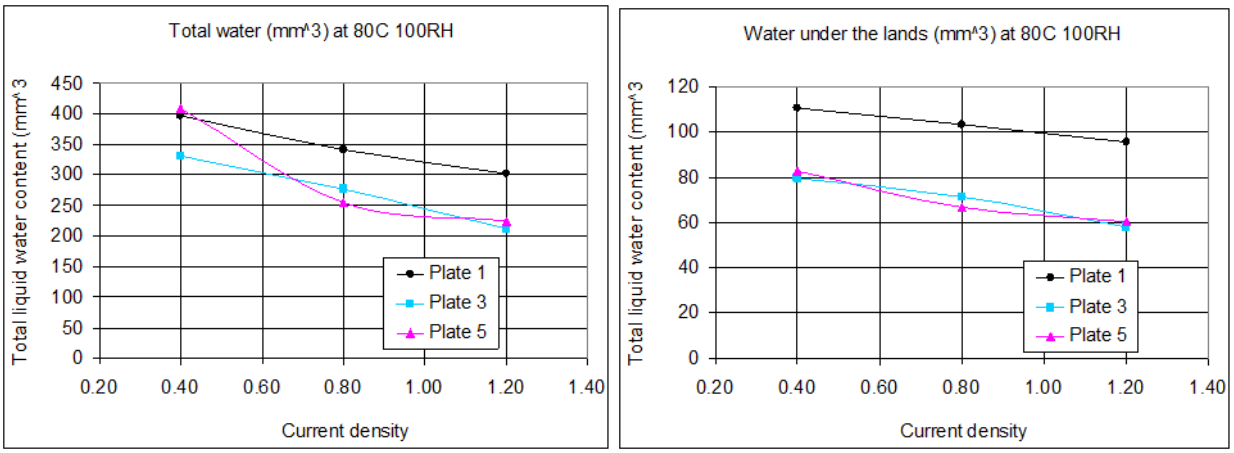

(a) (b)

Figure 28 (a) total water content and (b) water content under the lands only (i.e. with channels masked in the image processing) for the three plates at 0.4, 0.8, and 1.2 A/cm^2

Figure 29 displays the polarization curves for the three plates at 80°C and 100% RH that correspond to the previous neutron images and water content shown in Figure 28. The polarization data clearly shows performance differences between the plates. The difference in performance increases with current density. The performance curves show that plate 5C performs the best, while the baseline plate, 1C, performs the worst at high current. Note that plate 3C does not show the inferior performance relative to the nominal plate design 1C as it did in the original performance experiments; we suspect that the earlier test with plate 3C suffered from a damaged MEA (Figures 16 and 17). As a quality check the open circuit voltage (OCV) region of Figure 29 is magnified in Figure 30 to confirm that the MEA was the same in all tests. For the present tests, we also made sure that the MEAs were the same by checking the impedance data for kinetic region.

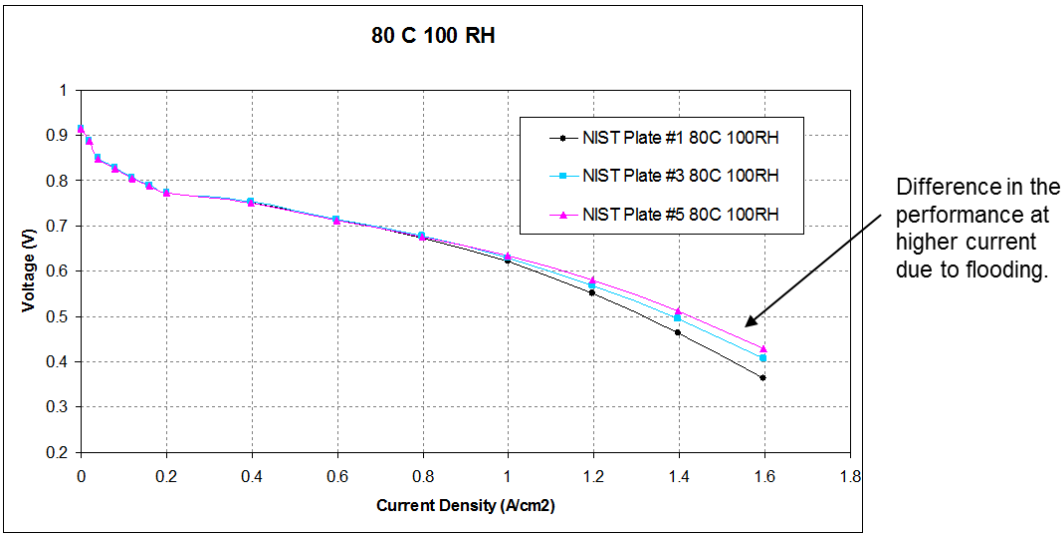

Figure 29 – polarization curves at 80 °C and 100 % RH

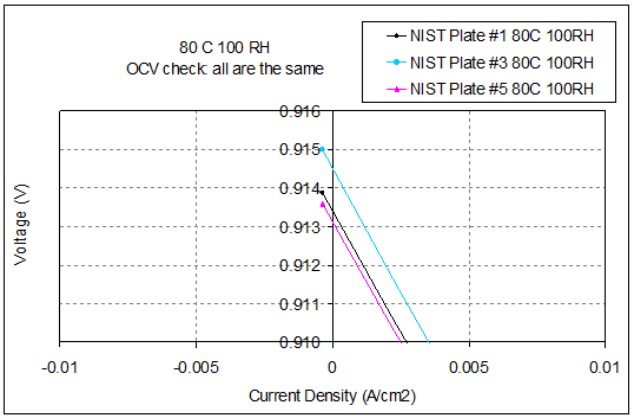

Figure 30 – Enlarged portion of the plot in Figure 29 to resolve OCV and to additionally verify that the cells are behaving the same in the kinetic region.

The electrochemical impedance spectra (EIS) was done at 3 different current densities (following each neutron imaging sequence), and is displayed in Figures 31a, b, and c. In addition, the EIS was modeled using a simple equivalent circuit to confirm that the charge-transfer resistance was the same for all 3 plates and that the difference in the EIS comes from the different mass-transport resistances with the three cathode plates. The EIS plots clearly show the resistance is the lowest for plate 5C and the highest for plate 1C. This is consistent with the voltage data, polarization curves, and the water content under the lands. The steady state cell voltages, measured after 20 minutes at set conditions, at these 3 current densities, are shown in Figure 31.

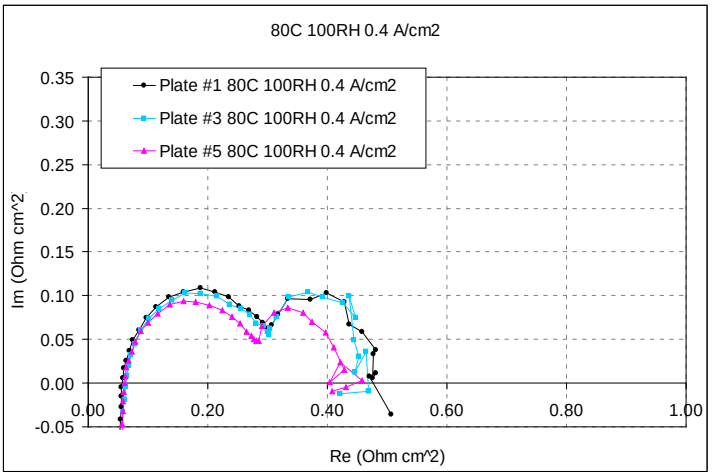

Figure 31(a) – EIS at 0.4 A/cm^2

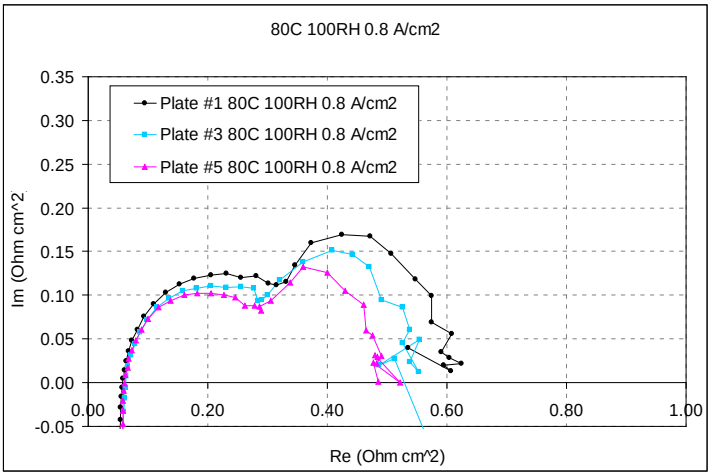

Figure 31(b) – EIS at 0.8 A/cm^2

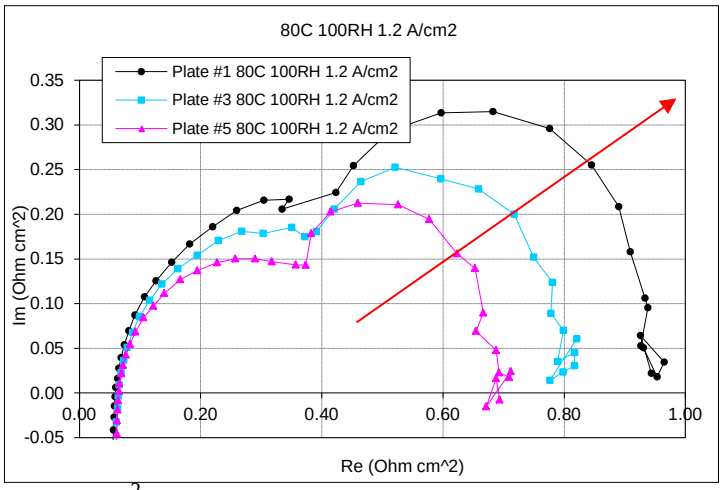

Figure 31(c) - EIS at 1.2 A/cm^2. The red arrow indicates the increase in mass-transport resistance going from Plate #5 to Plate #1, due to increased flooding under the lands.

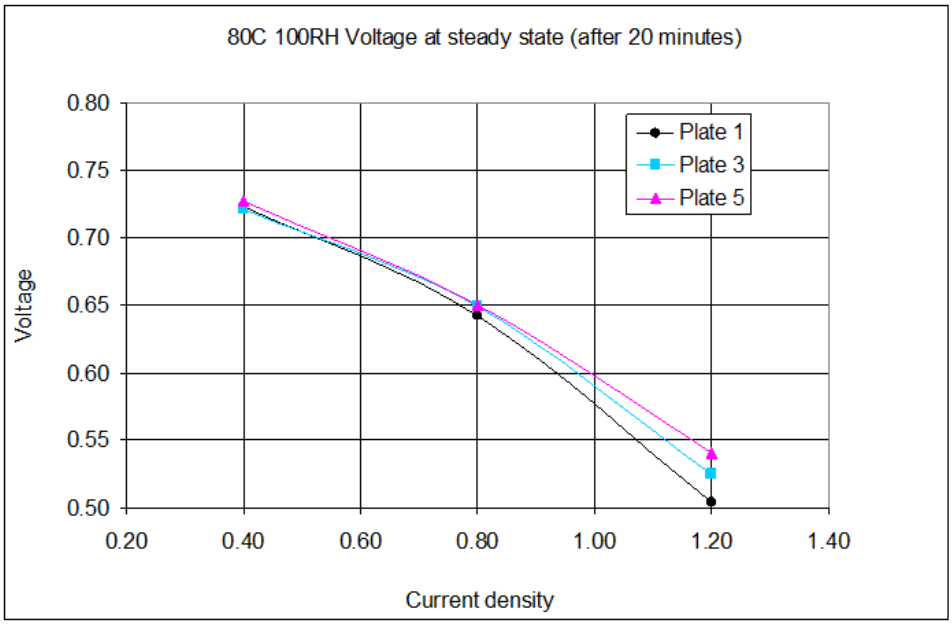

Figure 32 – voltage at steady state for the three cathode plates, at three current densities corresponding to EIS data and water measurements.

The experimental cathode plates were also tested at 80 °C and 50 % RH. The performance as shown in Figure 33 was very close for all three plates. The difference in the performance with three plates showed similar trend as observed at 100 %RH, however the difference was very small between the plates as the flooding levels were significantly lower with drier inlet gases. Although desired, the plates could not be tested at 40°C because the cell would overheat at higher current densities without the liquid cooling which is necessary to keep the cell temperature steady.

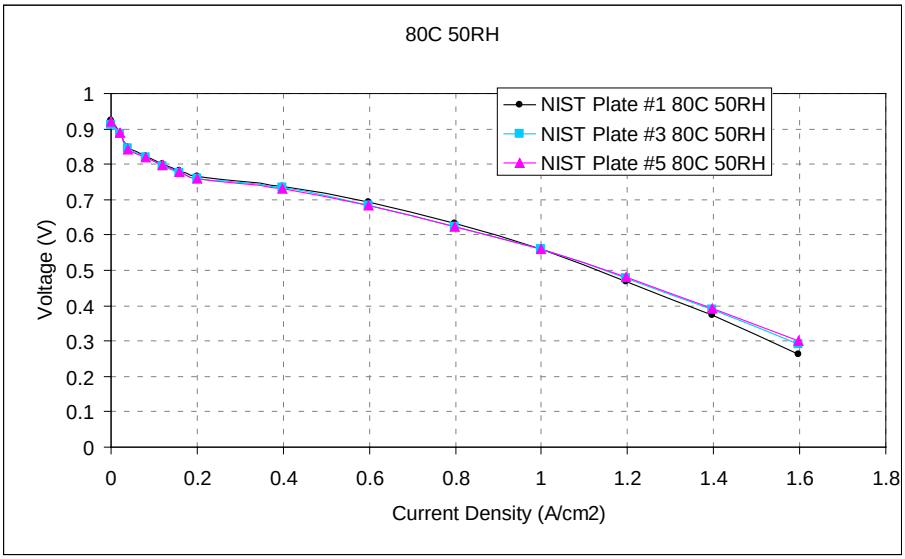

Figure 33 – polarization curves at 80°C and 50 % RH

LANL concluded the neutron imaging experiment by acknowledging there was a small but measurable performance difference at 80°C and 100 % RH. Performance data from polarization curves, steady-state measurements, EIS data, and water content measurements suggest that the difference in performance stems from higher mass-transport resistance with plate 1C. This is further evidenced by the higher water content in the GDL and CL under that lands for this plate, compared to the other two plates tested. LANL suggests that since plates 3C and 5C have tapered vertical channel sidewalls, while plate 1C does not, that this indicates having this unintentional taper could be beneficial for excess water transport from the GDL into the channels at certain conditions and with certain materials. This further depends on the GDL/MEA combination and the surface wetting properties of the bipolar plates [1]. In addition, the effects of manufacturing variations may differ for different flow field configurations (e.g. parallel channels instead of the serpentine channels), where high levels of channel flooding could be disadvantageous for the cell performance [2]. Lastly, LANL points out that the inferior performance of plate 3C did not repeat itself in these experiments thus a damaged MEA in the original experiments is suspected.

Conclusions

From the neutron imagining, LANL concluded that the 10° tapered sidewalls appear to be beneficial for excess water removal; at least with the materials used and under the conditions specified in these experiments. At the onset of this project this was considered a possibility based on the results reported by Owejan [3,4] where triangular cross-section channel designs were determined to be superior to rectangular cross-sections with regards to water management within the channel. This finding is good news for fuel cell manufacturing with regards to cost as the most viable high-speed manufacturing processes for either carbon or steel plates are often based on molding/stamping where perfectly orthogonal feature sidewalls are difficult, if not impossible, to achieve.

Another important observation is that the nominal plate design with almost no deviation from perfect geometry, 1C, was not the best performer. Rather plates like 3C, 5C and 8C dominated with their combination of precisely controlled geometric perturbations. With this, even in the absence of detailed engineering data, there is possibly enough quantitative information provided that two-phase flow modelers might be able to validate the sensitivity of their models.

Last and possibly the most important conclusion is that performance differences were observed, but the magnitude of these differences may not be cause for concern. If not, this suggests that channel dimensional tolerances may be unnecessarily constrained as the variation tested was equal to and in some cases much greater than the 0.012 mm to 0.05 mm tolerances gleaned from our discussions with industry. The reader is cautioned that this statement is made with the understanding that different operating conditions, channel design, flow field configurations, and material selections may yield different sensitivities.

The ideal outcome of this project would have been results that supported the generation of engineering data that related performance differences to individual manufacturing variabilities at specific magnitudes (i.e., sidewall taper, bottom straightness, sidewall straightness, and variation-in-channel width). The original data obtained on all the experimental cathode plates

suggest a potentially dominant two-factor interaction that cannot be specifically discerned due to the limitations of fractional nature of the design of experiments. Even if the design of experiments had been a full versus fractional factorial design and the results more specific, the latter neutron imaging experiments casts doubt on the initial results for one of the plates. Unfortunately, in total, the body of results described in this report does not support specific quantitative conclusions, however qualitatively there is value.

Lessons Learned:

How could this project have been executed differently to obtain better results?

(1) A full versus fractional factorial design of experiments would have provided the data necessary to evaluate both the main (single) factor influences and two-factor interactions. Unfortunately the required resources, especially in this case, might prevent this as the number of experimental plates to be fabricated, verified, and performance tested would have almost doubled.
(2) Although it was demonstrated that excellent performance data repeatability could be achieved between run disassembly, CCM replacement, and re-assembly, this does not prevent outliers like plate 3C. Although very time consuming, each of the ten experimental plates should have been run a minimum of three times with a new CCM between each run.
(3) Plate 3C's original erroneous performance should have been identified much earlier. LANL's finding, from the neutron imaging experiment that plate 3C as originally tested must have had a damaged MEA in the initial ten plate performance testing correlates with the performance data obtained from the back pressures sensitivity experiment. Unfortunately the opportunity was lost to test the other poor performing plate 7C. This supports the need for (2).
(4) Ideally, a complete comparison (with all plates) would have been performed using identical hardware design and materials. Had the neutron imaging been part of the original project plan this would have been adequately addressed, however since it was not several issues were encountered.
    a. The wetting properties of the plate material between the early tests and recent neutron imaging experiments were not identical. As identified through Dr. Allen's static contact angle testing, the pyrosealed POCO AXF-5Q plates were more hydrophobic than the original POCO AXF-5QCF plates. Although the mean difference was small, the variability in results across the POCO AXF-5QCF plate tested could be enough to alter the cell performance.
    b. Replacing the stainless steel by Aluminum alloy (better thermal conductor) for end plate material altered the thermal response of the cell.
    c. Changing the location of the heaters to satisfy the neutron imaging requirement likely affected the temperature distribution (and in turn water transport).

Publications:

E. Stanfield, Metrology for Fuel Cell Manufacturing, U.S. DOE Hydrogen and Fuel Cells Program 2008 Annual Progress Report, November 2008

http://www.hydrogen.energy.gov/pdfs/progress08/vi_3_stanfield.pdf

E. Stanfield, Cause-and-Effect: Flow Field Plate Manufacturing Variability and its Impact on Performance, U.S. DOE Hydrogen and Fuel Cells Program 2010 Annual Progress Report, February 2011
http://www.hydrogen.energy.gov/pdfs/progress10/vi_6_stanfield.pdf

E. Stanfield, Cause-and-Effect: Flow Field Plate Manufacturing Variability and its Impact on Performance, U.S. DOE Hydrogen and Fuel Cells Program 2011 Annual Progress Report, November 2011
http://www.hydrogen.energy.gov/pdfs/progress11/vi_6_stanfield_2011.pdf

E. Stanfield, Cause-and-Effect: Flow Field Plate Manufacturing Variability and its Impact on Performance, U.S. DOE Hydrogen and Fuel Cells Program 2012 Annual Progress Report, December 2012
http://www.hydrogen.energy.gov/pdfs/progress12/vi_7_stanfield_2012.pdf

Presentations:

Stanfield, NIST Fuel Cell Manufacturing Research Project Metrology for Fuel Cell Manufacturing, Presentation at U.S. DOE Hydrogen and Fuel Cells Program Annual Merit Review and Peer Evaluation, June 2008
http://www.hydrogen.energy.gov/pdfs/review08/mf_7_stanfield.pdf

Stanfield, Metrology for Fuel Cell Manufacturing, Presentation at U.S. DOE Hydrogen and Fuel Cells Program Annual Merit Review and Peer Evaluation, June 2010
http://www.hydrogen.energy.gov/pdfs/review10/mn006_stanfield_2010_o_web.pdf

Stocker, Stanfield, and Muralikrishnan, Metrology for Fuel Cell Manufacturing, Presentation to FreedomCar Tech Team, March 16, 2011

Stanfield, Metrology for Fuel Cell Manufacturing, Presentation at U.S. DOE Hydrogen and Fuel Cells Program Annual Merit Review and Peer Evaluation, May 2011
http://www.hydrogen.energy.gov/pdfs/review11/mn006_stanfield_2011_o.pdf

Stanfield, Cause and Effect: Flow Field Plate Manufacturing Variability and its Impact on Performance, Poster Presentation at U.S. DOE Hydrogen and Fuel Cells Program Annual Merit Review and Peer Evaluation, May 2012
http://www.hydrogen.energy.gov/pdfs/review12/mn011_stanfield_2012_p.pdf

Future Work:

Further performance testing might yield more definitive conclusions if it was done using all five experimental POCO AXF-5Q plates together with the investigative tools employed during the neutron imaging experiment, with the exception of the imaging itself. A revised statistical analysis cannot be done without all the plates being retested, which is not possible without further experimental plate fabrication and verification work.

Prior to conducting a similar experiment a re-evaluation should be done to determine the most suitable plate material and flow field design as the fuel cell technology has evolved significantly since the inception of this project.

As a starting point for similar experiments, this project at least identified the sources of unwanted variability and the tremendous level of diligence needed to control them, along with the value of multiple repetitions.

References:

[1] Spernjak D, Prasad A, Advani S, 2007, 'Experimental investigation of liquid water formation and transport in a transparent single-serpentine PEM fuel cell', Journal of Power Sources 170 334-344

[2] Spernjak D, Prasad A, Advani S, 2010, 'In situ comparison of water content and dynamics in parallel, single-serpentine, and interdigitated flow fields of polymer electrolyte membrane fuel cells', Journal of Power Sources 195 3553-3568

[3] Owejan J, 2003 'Neutron Radiography Study of Water Transport in an Operating Fuel Cell: Effects of Diffusion Media and Cathode Channel Properties', M.S. Thesis, Rochester Institute of Technology http://hdl.handle.net/1850/5279

[4] Owejan J, Trabold T, Jacobson D, Arif M, Kandlikar S, 2007, 'Effects of flow field and diffusion layer properties on water accumulation in PEM fuel cell', Int. J. Hydrogen Energy 32 4489-450

Subproject #2: Non-Contact Sensor Evaluation for Bipolar Plate Manufacturing Process Control and Smart Assembly of Fuel Cell Stacks

EXECUTIVE SUMMARY

The objective of this project is to enable cost reduction in the manufacture of fuel cell plates by providing a rapid non-contact measurement system that can be used for in-line process control. Manufacturers currently either visually inspect plates or use machine vision systems for verifying tolerances. Such methods do not provide the sub-10 μm accuracy that manufacturers are targeting. In this context, we have studied available non-contact sensors in the market for their suitability to be used for fuel cell plate metrology. From our studies, we have short-listed laser spot triangulation probes as one of the promising candidates for further exploration. We have since incorporated these probes in a unique two-probe system to develop a rapid yet high accuracy non-contact system that manufacturers can adopt towards process control and metrology. The key technical features and method are as follows. Our system is developed using commercially obtained stages and probes for a total cost of less than $50,000. Measurement capability includes channel profiles, height, width, side wall, top surface flatness, plate thickness, variation in thickness, etc. We have extensively documented error sources and constructed detailed uncertainty budgets. Measurement uncertainty on channel height and width of graphite bipolar plates are 6 μm (k = 2) on channel width and 3.8 μm (k = 2) on channel height. Measurement uncertainty on thickness are 20 μm (k = 2) on artifacts with high quality surfaces. We have tested measurement speeds from 30 mm/s to 500 mm/s, with no noticeable degradation in accuracy until 400 mm/s. And finally, we have developed mathematical techniques to process high density non-contact data across channels to determine features of interest such as height and width. All of this information is available in the public domain in the form of peer-reviewed journal and conference papers.

COMPARISON BETWEEN ACTUAL ACCOMPLISHMENTS WITH THE GOALS AND OBJECTIVES

The objectives of this study were to

- Identify and evaluate the capability and uncertainty of commercially available non-contact, high-speed scanning technologies for applicability to bi-polar plate manufacturing process control.
- Using capabilities identified in the first objective, demonstrate smart assembly concept (new under revised interagency agreement).

During the project, we identified numerous candidate technologies and conducted a thorough study to assess the feasibility of their use for rapid dimensional metrology of bipolar plates. We then identified laser triangulation probes as the most promising technology of them all. We then developed a prototype system using these probes to measure features on a fuel cell plate. We performed numerous experiments to study the different error sources and developed detailed

uncertainty budgets for these measurements. These experiments and results have been documented in numerous quarterly reports, annual reports and journal/conference publications. We therefore clearly met the stated objectives in bullet 1 above.

The second objective was added in 2009 under a revised interagency agreement. It pertains to the demonstration of the smart assembly concept where plate parallelism information was to be used to show how individual plates can be selected and stacked so that the overall stack parallelism is maintained within tolerance. During the course of the work, after discussions with numerous manufacturers and feedback from the merit review cycles, it was decided that our expertise in the area of measurement science could be better utilized to develop, demonstrate, and optimize the system's ability to measure thickness and variation in thickness, which can later be used by others to demonstrate smart assembly concept. Therefore, over the course of the last year of the project, we modified our system to perform thickness measurements, studied error sources, and created a detailed error budget for these measurements. We therefore clearly demonstrated that plate thickness and variation in thickness can be measured rapidly and accurately. Plates can therefore be tagged with this information allowing careful selection of plates for purposes of smart assembly.

SUMMARY OF THE WORK

The summary is organized as follows. We present an overview of the work in section 1. In section 2, we describe error sources in laser triangulation probes and their impact on dimensional measurements. In section 3, we describe the prototype system developed to measure plate channel features. In section 4, we describe a different arrangement of probes for the measurement of plate thickness and parallelism. In section 5, we present an overview of methods developed to analyze free form channel profiles. We present conclusions in section 6, references in section 7 and products developed under the award in section 8. The contents are as listed below.

1. Technology identification
2. Error sources in laser triangulation probes
   - 2.1. Introduction
   - 2.2. Repeatability and noise levels
   - 2.3. Linearity errors
   - 2.4. Influence of material/optical properties on height measurements
   - 2.5. Influence of material/optical properties on width measurements
   - 2.6. Effect of spot size on width measurements
   - 2.7. Side wall reflections
   - 2.8. Secondary reflections
   - 2.9. Measurements at grazing angle
3. Bipolar plate channel metrology
   - 3.1. System prototype
   - 3.2. System parameters and calibration
   - 3.3. System validation using gage blocks

3.4. Comparison of non-contact probe measurements with UMAP system (contact probe)
3.5. Uncertainty in height and width
3.6. Errors as a function of measurement speed, tests at 30 mm/s and 100 mm/s
3.7. Summary
4. Plate thickness metrology
4.1. System prototype
4.2. System parameters and calibration
4.3. Uncertainty budget for thickness measurements
4.4. System validation using gage blocks
4.5. Comparison of non-contact probe measurements with contact probe CMM
4.6. Summary
5. Analysis of non-contact channel data from free-form profiles
6. Conclusions
7. References
8. Products developed under the award and technology transfer activities

1. **TECHNOLOGY IDENTIFICATION**

To achieve the objectives of this project we surveyed both the fuel cell plate manufacturing industry and the measurement equipment manufacturing industry. With regards to the fuel cell plate manufacturing industry, we identified the current measurement inspection technologies being employed, the dimensional parameters of interest, and the applicable tolerance levels encountered. Using this information we researched commercially available high-speed non-contact measurement technologies that might be suitable based on published literature. These included photogrammetry, laser conoscopy, digital holography, phase measuring interferometry, structured light projection, laser spot triangulation, and laser line triangulation. We identified laser spot triangulation probes as the most suitable and assembled the probe into a measurement system (test bed) capable of performing detailed single-sided vertical and lateral channel dimensional inspection. This was followed by the expansion of the system to achieve the ultimate goal of dual-sided evaluation enabling thickness and variation-in-thickness measurement capability. In subsequent sections, we present the details of our research procedures, key outcomes and accomplishments.

2. ERROR SOURCES IN LASER TRIANGULATION PROBES

2.1 **Introduction**

Laser spot triangulation probes have numerous sources of error [1-8]. In this section, we describe the different sources of error and demonstrate their impact on linear dimensional measurements through carefully constructed experiments. The experiments described in this section along with the results are important in understanding measurement errors when bipolar fuel cell plates are inspected using triangulation probes.

2.2 **Repeatability and noise levels**

The single point repeatability of the probe for data acquired over several seconds (at a sampling rate of 50 μs) is slightly less than 1 μm (one standard deviation) for the probe that we tested. The manufacturer's specification of 50 nm is valid when a moving average filter of 256 data points is applied. The data from the analog output port has a noise level in the ±2 μm range.

Implications for dimensional measurements: The repeatability of the probe is not anticipated to be a major source of error in height and width measurements because of the significant averaging that occurs in their calculation.

2.3 Linearity errors

The linearity error of the probe is specified to be ±5 μm over the full travel of 10 mm for the Keyence LK-G32. This specification is based on normal incidence on a white ceramic target. Most applications will involve situations where neither the normal incidence nor the white ceramic criteria is met. We therefore performed some tests to determine the linearity error of the probe for a variety of situations. The experiments and results are discussed next.

For these experiments, the probe was mounted as shown in Fig. 1 (see side view) with the plane of the probe's measurement triangle in the *XZ* plane. A part was positioned on the linear stage and as close as possible to the probe. The part was then moved along the *X* axis in increments of 0.2 mm over the full travel of 10 mm, and the probe reading was obtained at each position. Because the positioning accuracy of the stage was verified previously with a laser interferometer to be less than 0.5 μm over 10 mm, the errors in the probe are simply the difference between the probe's readings and the *X* axis encoder readings.

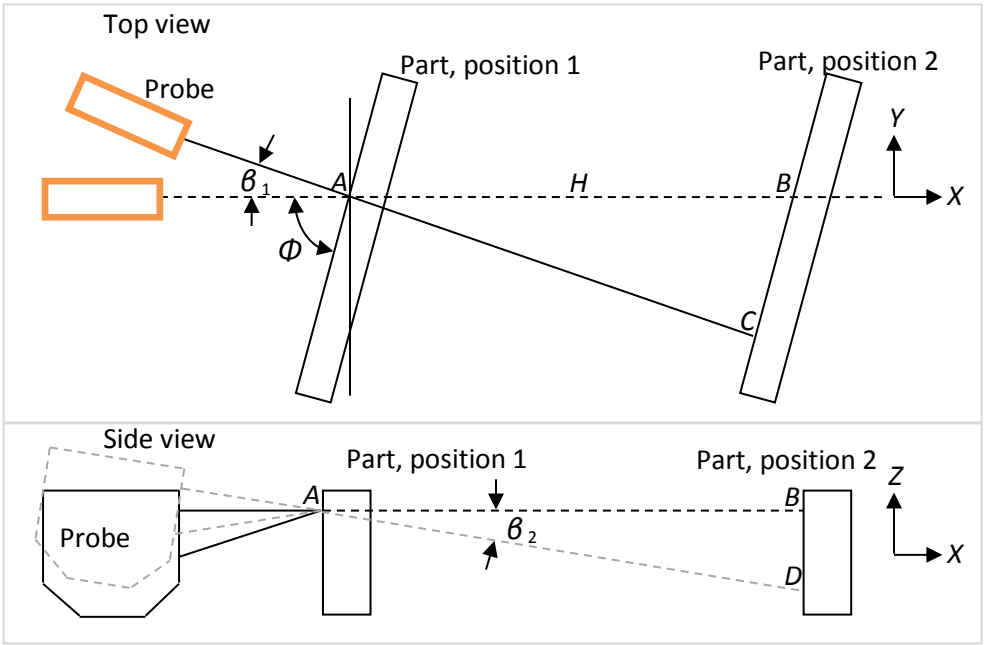

Fig. 1 *Schematic of the setup to determine linearity errors for different part orientations*

One of the objectives in our testing was to determine linearity errors when the probe's laser is not normally incident on the surface. We therefore intentionally rotated the part by an angle Φ in the *XY* plane as shown in Fig. 1 (top view). This rotation simulates the measurement of the side wall of a part with the probe tilted as in Fig. 1. A consequence of this intentional rotation is that considerable care must now be taken in aligning the probe in the *XY* plane because even small misalignments can cause large errors. If the probe is misaligned by angle β_1 with the *X* axis as shown in Fig. 1 and the measurement surface of the part makes an angle Φ with the *Y* axis, then the error *e*, given by *AC-AB*, can be shown to be

$$e = \frac{H}{\cos\beta_1}\left(\frac{1}{1+\tan\beta_1/\tan\phi}\right) - H \qquad (1)$$

For the case of normal incidence, Φ = 90°, the error *e* is simply given by $e = H/\cos\beta_1$ as expected. If the probe is misaligned by a small amount, say β_1 = 0.1°, the error *e* over the travel of 10 mm is less than 15 nm. However, if the part were intentionally rotated so that Φ = 25°, and the probe were misaligned in the *XY* plane by 0.1°, the error is -37.3 µm. This error is due to a misalignment in the setup and should not be interpreted as the probe's linearity error. Misalignment of the probe in the *XZ* plane (⏥ in Fig. 1 sideview) produces a small error given by $e = H/\cos\beta_2$. This error is not influenced by the angle Φ.

For the case of normal incidence, we show the linearity error without removing the slope in the data because the contribution from β_1 and β_2 to the overall error is extremely small (less than ±0.4 µm) when the part is aligned so that the angle Φ is within 90° ±0.5°. We can attribute any slope in the data to the actual scale error in the probe. Figs. 2 and 3 show the errors for two identical probes from the same manufacturer and for two different materials. Notice that the linearity error is different for both probes and exceeds the manufacturer's specification of ±5 µm for the non-ceramic case (graphite).

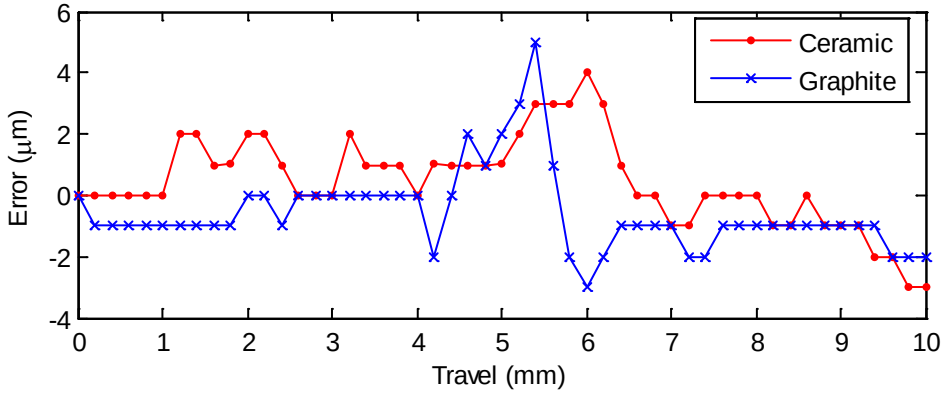

Fig. 2 *Linearity errors when Φ = 90° for probe # 1*

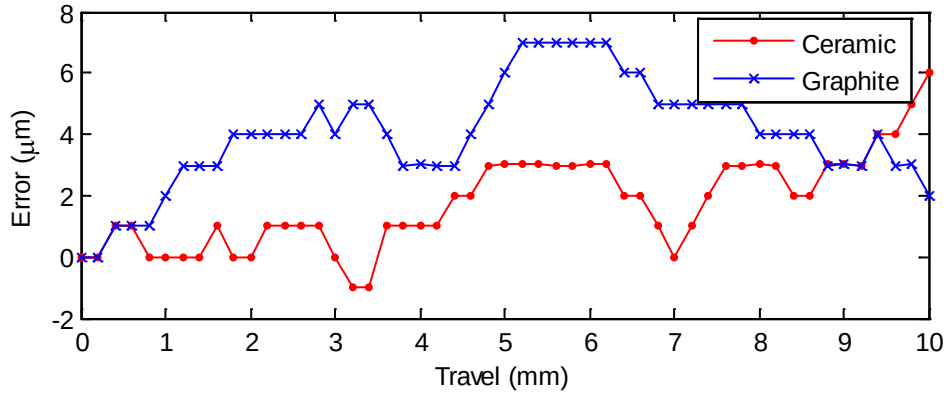

Fig. 3 *Linearity errors when Φ = 90° for probe # 2*

For the case where Φ = 25°, we show the measured errors before removing the slope in Fig. 4 and after removing the slope in Fig. 5. As explained earlier, we attribute the slope in Fig. 4 to a misalignment of the probe; a 1° misalignment can produce errors as large as 400 µm over 10 mm. Fig. 5 shows that the linearity errors can be larger than the manufacturer's specification for non-ceramic surfaces.

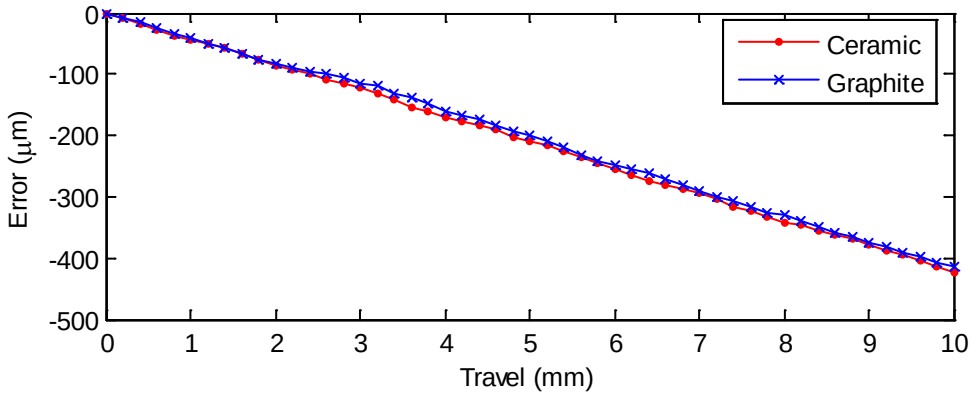

Fig. 4 *Linearity errors when Φ = 25° for probe # 1 before removing the slope*

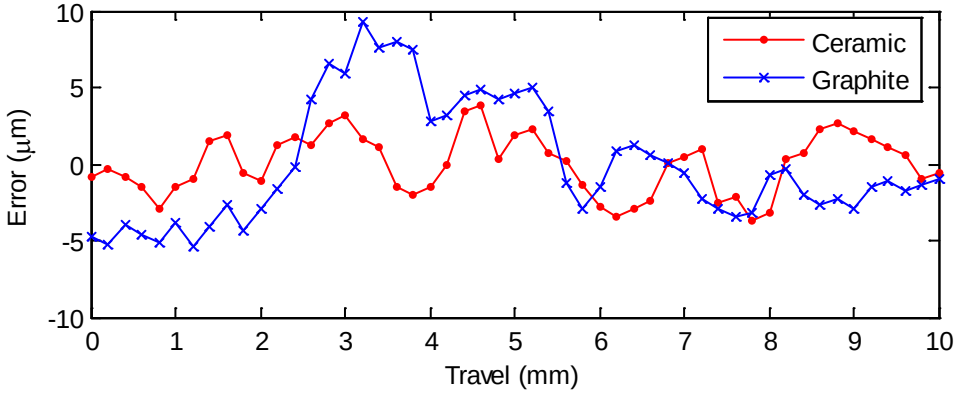

Fig. 5 *Linearity errors when Φ = 25° for probe # 1 after removing the slope*

Implications for dimensional measurements: The results show large changes in the linearity error over short travel distances. Fig. 2 shows an error of almost 8 μm over a range that is less than 1 mm for the graphite surface. Therefore, the positioning of the part within the probe's range will have substantial effect on the accuracy of the results. The manufacturer's specification is only valid for ceramic surfaces under normal incidence. It is likely that the linearity error will exceed the specifications for most practical measurement applications.

2.4 **Influence of material/optical properties on height measurements**

It is well known that laser triangulation probes are very sensitive to material/optical properties of the components under measurement. The problem of laser surface penetration is pointed out by [6, 8] while volumetric scattering is discussed by [2].

To demonstrate the influence of subtle changes in material/optical properties of the test component on linear dimensional measurements, we considered four ceramic gage blocks that appeared to be visually similar (in terms of color and surface texture). The objective of our experiment is to measure the height of one the blocks under two different conditions as discussed below.

In the first case, we wrung the block on another ceramic block (they were both European blocks but possibly not from the same set) to form a cross-block pair as shown in Fig. 6(a). We obtained a profile across the blocks and calculated the height from that data.

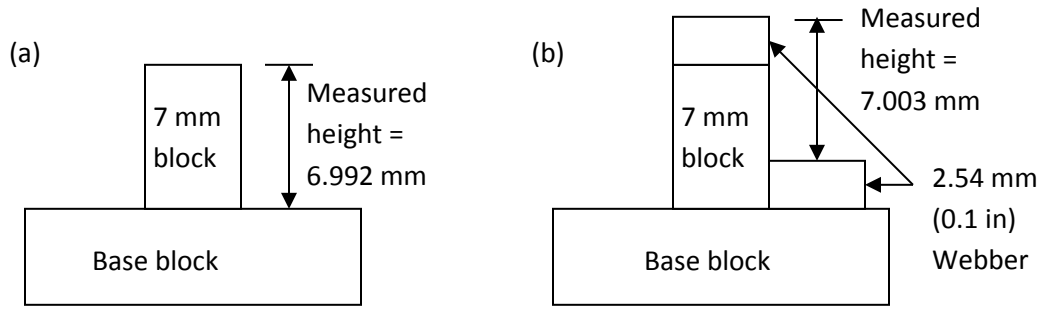

Fig. 6 *(a) A crossed block pair to generate a nominal 7* mm *height (b) Realizing the same physical length but with different ceramic blocks presented to the probe for measurement*

In the second case, we choose two different ceramic blocks of the same height (each is a Webber 0.1-inch) and wrung them to both the bottom and the top block of the cross-block pair. The purpose of doing this is to present a different material to the sensor while maintaining the same physical length. This is shown in Fig. 6(b). We then measured a profile across the blocks and calculated the height. The measured height for case (a) in Fig. 6 was 6.992 mm while the

measured height for case (b) was 7.003 mm. There is a difference of 11 μm in the measured height simply by changing the material presented to the probe.

It should be pointed out that if the material/optical properties of the base block and the 7-millimeter ceramic block were identical, then any error will be common-mode between the top and bottom surface and therefore cancel out. The results should then indicate a smaller deviation from the nominal value (which is within a few tens of nanometers of the true value) of 7 mm. That is however not the case here suggesting that the material/optical properties of the base block are different from that of the 7-millimeter block. It is reasonable to assume that the two 0.1-inch blocks are identical in terms of their material/optical properties because the result of that measurement is much closer to the nominal value (the discrepancy of 3 μm is possibly due to error sources in the probe such as its linearity).

Implications for dimensional measurements: Material/optical properties can have a significant influence on the measurement errors as our experiments on visually similar gage blocks reveal. In measuring height, it is extremely critical that the material/optical properties at the two ends of the measurement be identical; otherwise large errors on the order of tens of micrometers are possible.

2.5 **Influence of material/optical properties on width measurements**

We performed a similar experiment on width measurements using ceramic blocks. For this experiment, we tilted the probe as shown in Fig. 13(b) (in section 3) and obtained a profile from which we determined the position of one side wall of the gage block. A second probe with an opposing tilt was used to acquire data from the opposing side wall. We calculated the width as the difference between the edge positions. However, the probe offset (distance between the probes) is an unknown quantity and therefore this process has to be first performed on a calibrated width. Subsequent to this calibration, we can measure the width of other test blocks.

Three ceramic blocks, a 1-inch, 2-inch and 3-inch, were considered for the experiment. Instead of directly measuring the width of the blocks across their side walls, we wrung two thin ceramic blocks to their gaging surfaces and measured the internal distance between the two thin blocks as shown in Fig. 7. The purpose of wringing the thin blocks is to present the same surface for all three gage blocks; therefore, we removed the two thin blocks from the 1-inch block after the measurement and subsequently wrung the same blocks to the 2-inch and 3-inch block for the measurement.

Subsequently, we chose two other sets of two thin blocks and repeated the measurements on the 1-inch, 2-inch and 3-inch blocks. Although all three sets of thin blocks appear to be visually similar, the widths obtained using the different blocks varied considerably. We refer to the thin blocks as European (British Standards blocks), Mitutoyo, and Webber.

The results are shown in Table 1. The offset between the probes was calibrated using the 1-inch gage block measured with the thin European blocks. Therefore, that entry (in the first row and first column) has a zero error.

The results indicate that the errors in the measurement of the 1-inch, 2-inch and 3-inch gage blocks are small (less than ±1 μm) if the probe offset calibration is performed using blocks of similar material. For example, the errors when using the Mitutoyo blocks are -4.5 μm, -4.6 μm and -5.1 μm for the 1-inch, 2-inch and 3-inch blocks respectively when using the European 1-inch block as the master. If a Mitutoyo 1-inch block were instead used as the master, the errors for the 2-inch and 3-inch blocks would only be -0.1 μm and -0.6 μm respectively. That is, the range of the errors is small across any row in the table; but the range of errors is large across a column indicating that changing the material seen by the probe can have a large influence on the measured length. For example, the first column shows that if the same 1-inch gage block is measured with three different thin gage blocks of slightly different material properties, we can potentially see large errors, up to 7 μm, between measurements.

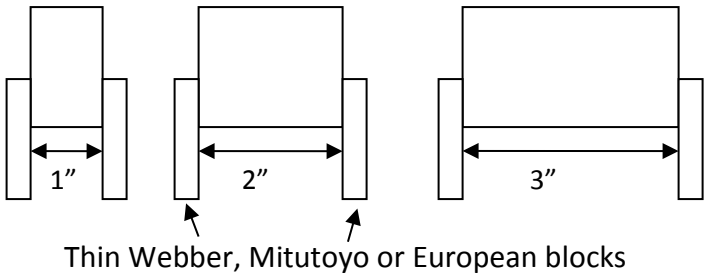

Fig. 7 *Width measurements across the gap created using thin blocks*

Table 1: Width errors in micrometers

Nominal	1-inch	2-inch	3-inch
European	0	0.4	1.1
Mitutoyo	-4.5	-4.6	-5.1
Webber	-7.1	-5.6	-6.1

Implications for dimensional measurements: When using the probe in the configuration shown in Fig. 13(b) for width measurements, it is necessary to calibrate probe offset using a master made of identical material to the part. Otherwise, large errors on the order of 10 μm in width measurements are possible.

2.6 **Effect of spot size on width measurements**

Although the spot sizes of different laser triangulation probes are specified at the center of the range, the size varies significantly at the extremes of the range because the beam is generally conical in shape. In probably its most common setup, the probe is mounted vertically to look straight down on the object under measurement. As the object is scanned, a profile is generated from which height measurements are generally made. Attempting to infer width information from such profiles will be prone to errors because some portion of the beam will still strike the top surface of the block (and therefore be sensed by the probe) even as the center of the beam is just outside the block. This is shown for three different cases in Fig. 8 for a nominal 0.3 in (7.62 mm) gage block. The measured widths for the three cases are shown in Table 2. The measured widths could deviate from the expected width (column 4 in Table 2) for several reasons: chamfer in the gage block, probe not positioned exactly at the range values indicated in the table, spot size of the probe deviating from the expected values in the table, etc.

Table 2: Effect of finite spot size on measured width of gage blocks, all units in millimeters

Case	Range	Spot size[1]	True width	Approximate expected width	Measured width	Width error (Measured-True)
a	0	0.03	7.62	7.68	7.664	0.044
b	+5	0.25	7.62	7.87	7.848	0.228
c	-5	0.25	7.62	7.87	7.864	0.244

[1] Note that the spot sizes are the nominal values as specified by the manufacturer

For these experiments, we note that the part is mounted on another block so that any reflection of the beam from the side walls of the gage block does not strike another surface. Secondary reflections are therefore avoided, at least in our case where we have noticed the absence of a second peak in the intensity graph of the return beam. We should note however that Buzinski et al [1] have indicated that some triangulation probes can in fact sense scattered light even from a vertical side wall.

Implications for dimensional measurements: The edge detection capability is limited by the finite size of the spot. In addition, features in the part such as edge chamfer can further deteriorate the

probe's ability to detect edges accurately when the probe is mounted to look straight down on the part. We have shown that errors on the order of 250 μm in the width are possible simply by measuring the same width at different ranges of the probe where the spot sizes are different. The measured width appears larger than the true width due to this error source.

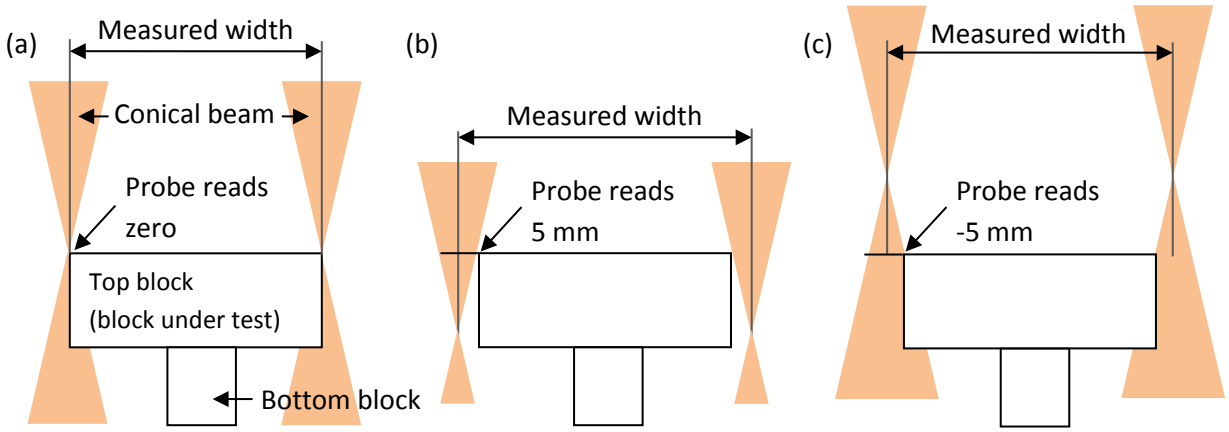

Fig. 8 *The effect of different spot sizes on width measurements (a) The probe is focused on the top surface (b) The probe is positioned so that it reads 5* mm *at the top surface. The spot size is 250* μm *at this position. (c) The probe is positioned so that it reads -5* mm *at the top surface. The spot size is 250* μm *at this position also.*

2.7 **Side wall reflections**

We describe here another set of experiments where we attempt to measure the width of gage blocks under different mounting conditions than described in the preceding section. While in the previous case, there was an apparent expansion of the block, there is an apparent contraction in the block in this case. Unlike in the previous section where the block under test (the top block) was mounted in such a manner as to avoid any reflection from the bottom block, here we mount the test gage block (the top block) on another gage block (the bottom block) so that the reflected beam from the side wall of the top block strikes the bottom block and the resulting scattered light is sensed by the probe. Two cases where the errors in the measured width are substantially larger than those described in the previous section are shown in Fig. 9.

Case a: The probe is positioned so that the top surface of the bottom block is at the center of the probe's range. The top surface of the block under test is out of the probe's measurement range. From Fig. 9 (a), it can be seen that even if the center of the beam is inside the block under test, some portion of the converging beam strikes the side wall and is reflected to the top surface of the bottom block. The light scattered from this surface is then sensed by the probe. The measured width is therefore much smaller than the true width. We experimentally determined the width to be 7.22 mm, which is 0.4 mm smaller than the nominal. Attributing half the error to each side of the gage block, the apparent contraction on either side is 0.2 mm. The half angle of the conical beam is 1.26° (calculated from the spot sizes of 30 μm and 250 μm at the center of the probe's range and at 5 mm respectively). The height of the block under test is about 8.8 mm. Therefore, the calculated contraction in width at either end is 8.8tan(1.26) = 0.194 mm, which is comparable to the experimentally determined value of 0.2 mm.

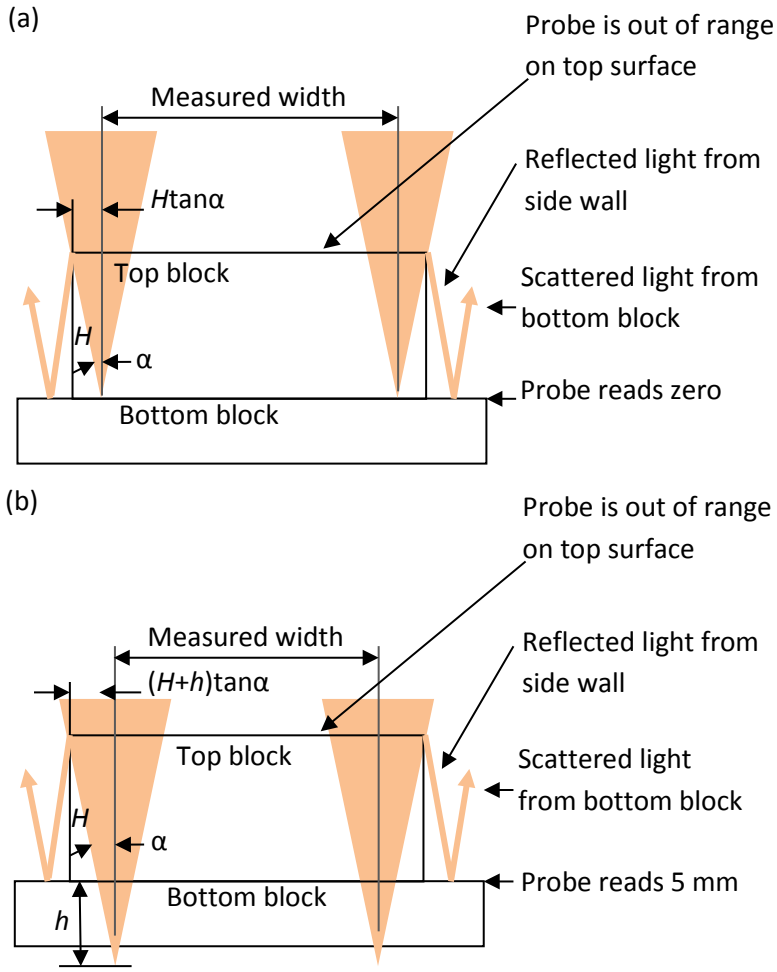

Fig. 9 *Side wall reflection resulting in an apparent contraction of the measured width (a) the probe is positioned so that the top surface of the bottom block is at the center of the probe's range. (b) The probe is positioned so that the top surface of the bottom block reads 5* mm *(one end of the probe's range).*

Case b: The problem described in the previous case is further accentuated when the probe is lowered so that the top surface of the bottom block is at the end of the probe's range (5 mm). We experimentally determined the width to be 7.006 mm for this case, which is 0.614 mm smaller than the nominal. The apparent contraction on either side is 0.307 mm. From the geometry in Fig. 9(b), the calculated contraction is the sum of the value determined in case (a) and half the spot size at 5 mm, which is 0.194 + 0.125 = 0.319 mm. This value is comparable to the experimentally determined value of 0.307 mm.

Implications for dimensional measurements: Determining the edge position in presence of side wall reflections followed by scattering from a secondary surface can lead to even larger errors than that described in section 3.5. If the reflected beam from the side wall has an opportunity to strike another surface, the errors in the width can be as large as 2*H*tan*α*. For a part that is 25 mm

tall, the error can be as large as 1 mm. The measured width appears to be smaller than the true width due to this error source.

2.8 **Secondary reflection**

Secondary reflection near the intersection of surfaces produces a second peak in the intensity graph of the return beam. While probe manufacturers generally provide some scheme to detect the dominant peak and therefore attempt to eliminate the effect of the secondary reflection, the problem nevertheless persists in many practical applications.

Example 1: Gage block width measurement

In an experiment that combines the issues described in the previous two sections, we attempt to measure the width of a gage block under the situation shown in Fig. 10(a) where the center of the probe is approximately at the half-height of the block. Under this situation, the probe can sense both the top surface of the top block and also the top surface of the bottom block (due to reflection from the side wall). In an ideal case, the apparent expansion due to a finite spot size and the apparent contraction due to side wall reflection serve to cancel each other. In practice, there is still some small error.

In Fig. 10, as the center of the beam is aligned with the vertical edge of the side wall, exactly half the beam (of width equal to $(H\text{-}h)\tan\alpha$) strikes the top surface and the resulting scattered light is sensed by the probe. The other half of the beam is reflected off of the side wall and strikes the bottom surface. The scattered light from this surface is also sensed by the probe. There are therefore two peaks in the return intensity graph of the beam. Fig. 10(a) shows the schematic of the setup while Fig. 10(b) shows the dual peak in the intensity graph of the return beam.

In an ideal case, the software identifies the dominant peak to determine where the center of the spot actually lies. But this determination may be influenced by many other factors such as edge chamfer, subtle changes in optical properties between the bottom and top surface, the reflectivity of the side wall, etc. In our experiments, we measured a width of 7.583 mm in this case, which is only 37 μm smaller than the nominal width. Given the number of factors that can potentially influence the edge determination, and therefore the width, this appears to be a reasonably small error.

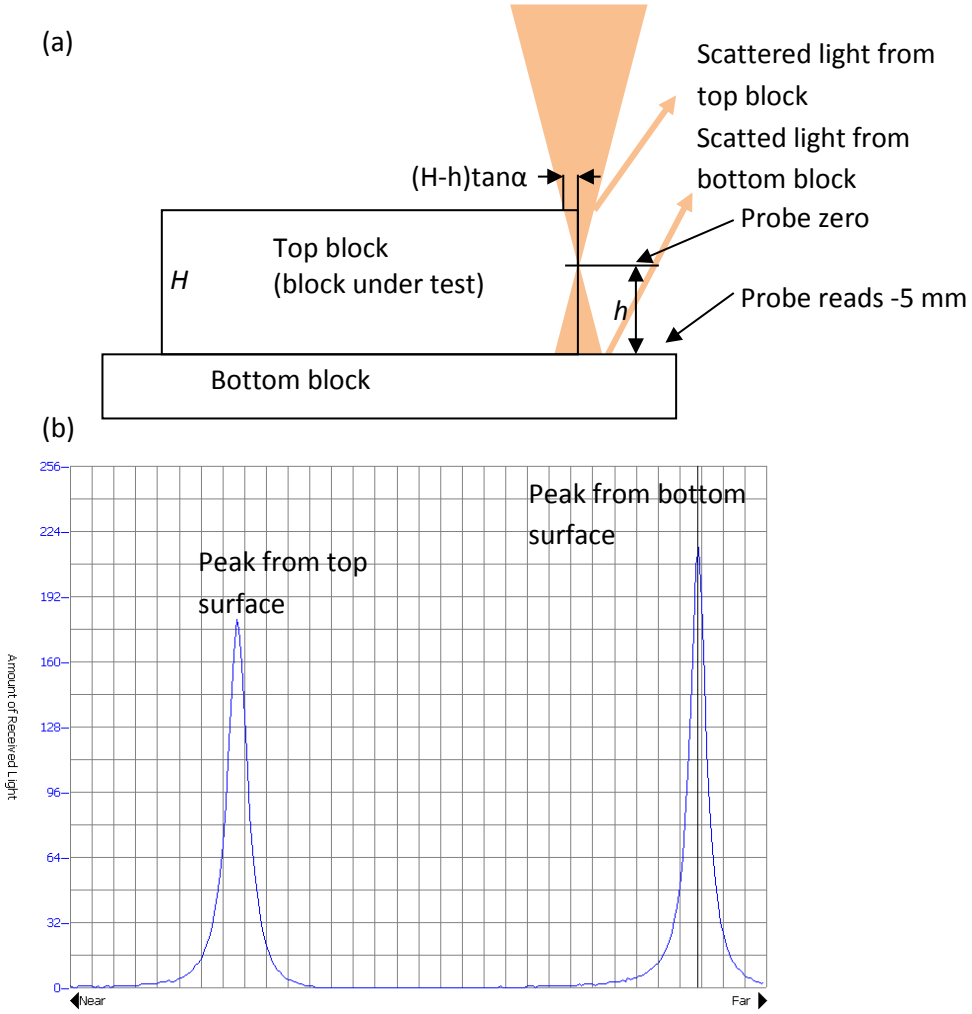

Fig. 10 *(a) Width measurement in presence of secondary reflections (b) Dual peak in the intensity graph of the return beam*

Example 2: Fuel cell channel measurement

In Fig. 11, we show the data acquired near the intersection of two perpendicular surfaces. The curvature in the vertical surface is an artifact of the measurement (other independent measurements confirm this). The intensity graph of the return beam did demonstrate two peaks in that region but the software could not clearly discern the true surface location, as the resulting data suggests. This data near the intersection demonstrates a limitation of triangulation probes.

Implications for dimensional measurements: Avoiding secondary reflections is a major challenge when attempting to perform high accuracy measurements with triangulation probes. In the example of the fuel cell plate, the data on the vertical wall clearly reveals the extent of the problem. If only the top part of the vertical edge is considered in determining the location of the edge, that value is approximately 407.1 mm. If however, some portion of the bottom part is considered instead, that value may be as small as 407.05 mm, or a difference of about 50 µm.

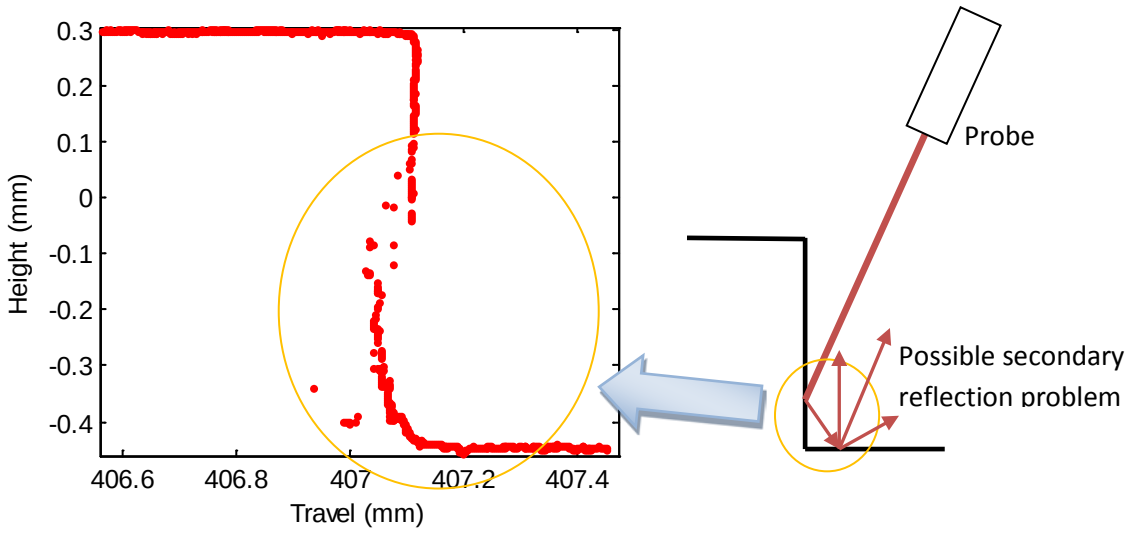

Fig. 11 *Data near the intersection of two perpendicular surfaces shows an error in the measurement due to possible secondary reflections.*

2.9 **Measurements at grazing angle**

We mentioned earlier that the linearity specification for the probe is only valid for the case of normal incidence and a white ceramic target. We showed how the linearity error can increase when the part is inclined at steep angles. We presented data for the case of normal incidence where Φ = 90° and for the case when Φ = 25°. Here, we present the results of measurements made on even steeper angles.

Fig. 12 shows the deviations from a least squares best fit line of profiles measured on a white ceramic gage block (the gaging surface is vertical, i.e, it is in the *YZ* plane) with the probe inclined at different angles (as in Fig. 13(b)). Because the block itself has negligible flatness, the deviations shown in the data can be attributed to the probing system. It can be seen that as the angle decreases (the beam tends to be grazing the surface), the amplitude of the deviations increases significantly. The range of the data for the case of 10° is more than 40 µm. For the 30° case, the range is approximately 10 µm which is just within the specification for the probe.

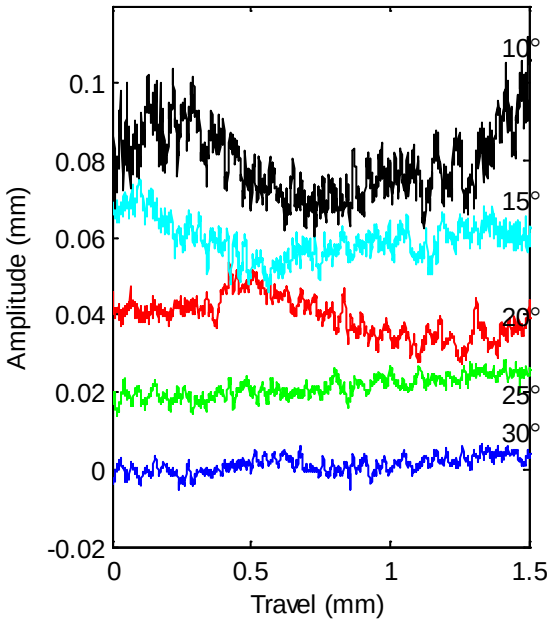

Fig. 12 *Profile measurements of a vertical surface (ceramic gage block) with different tilt angles of the probe as in Fig. 13(b). A tilt angle of zero implies that the incident beam is grazing the surface while a tilt angle of 90° implies that the beam is normal to the surface.*

Implications for dimensional measurements: If measurements are made at near-grazing angles, the results must be interpreted with caution as a significant portion of the error may be due to the probing system. We have demonstrated errors as large ±20 μm in profile measurements made at 10° angle on white ceramic surfaces.

3. BIPOLAR PLATE CHANNEL METROLOGY

3.1 System prototype

Laser spot triangulation probes offer both the required range (a few millimeters) and the necessary resolution (sub-micrometer) to perform accurate dimensional measurements on fuel cell plates. A laser spot triangulation probe in conjunction with an *XY* stage, provides a convenient way of performing dimensional measurements on different artifacts. If only a single probe is used, and this probe is set up to look straight down on a fuel cell plate as it is scanned across, the finite spot size of the probe limits the ability to detect the transition from horizontal to vertical surface near the channel's side wall and therefore limits the accuracy with which channel width can be detected. Further, a single probe looking straight down provides no information on the side walls of the channel, such as its taper and form. We therefore utilize two probes that are tilted in opposing directions so that each probe can capture data on one side wall and some part of the bottom of the channel. This dual-probe scheme is shown in Fig. 13. Our system utilizes two Keyence LK-G32 laser spot triangulation probes, an Aerotech ALS 50060 stage for the *X* axis and an Aerotech PRO 115 stage for the *Y* axis.

Having two probes necessities the determination of six system parameters (tilt angles and offsets) shown in Fig. 13(b). Determining these system parameters accurately is essential in superimposing the data from the two probes into a common frame of reference. While it may appear that the tilt angle θ of the probes can be determined by measuring a calibrated height block, such measurements are corrupted by misalignment angle α and are therefore not very accurate. We further demonstrate that vertical profile measurements (measurements on the vertical face of a gage block) can yield much higher accuracies because the misalignment angle α can be separated out.

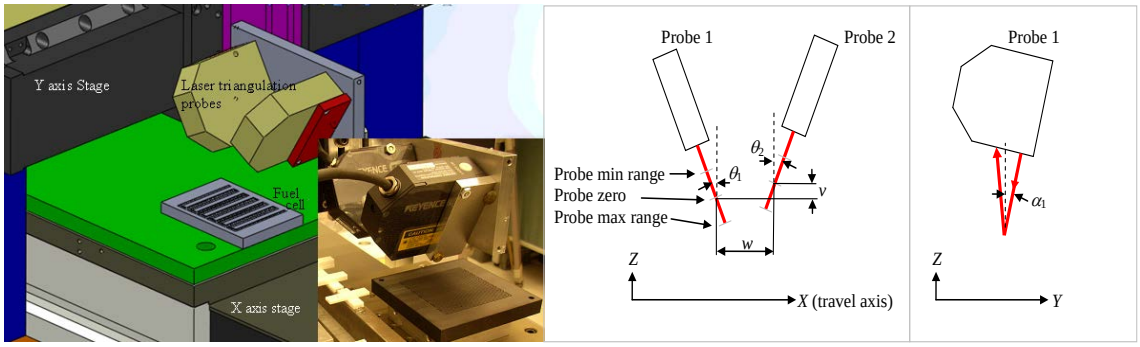

(a) (b)

Fig. 13 *(a) The fuel cell metrology station showing two laser triangulation probes, each tilted in opposing directions to obtain side wall information (b) Six system parameters to be determined by calibration*

3.2 System parameters and calibration

Six system parameters have to be determined for our dual-probe system by prior calibration before the system can be used for the measurement of bipolar fuel cell plates. These are:

θ_1: tilt of the first probe in the *XZ* plane. This is nominally set to -25°, see Fig. 13.

θ_2: tilt of the second probe in the *XZ* plane. This is nominally set to 25°, see Fig. 13.

w: horizontal offset measured as the distance between the probe's zero readings along the *X* axis, see Fig. 13.

v: vertical offset measured as the distance between the probe's zero readings in the vertical direction, see Fig. 13.

α_1: misalignment of the first probe in the *YZ* plane. This is nominally zero, see Fig. 13.

α_2: misalignment of the second probe in the *YZ* plane. This is nominally zero (not shown in Fig. 13).

Assuming the system parameters are completely known, the measured data which is in a non-orthogonal frame (because the probing direction is inclined at an angle θ with respect to the Z axis) has to be corrected to an orthogonal frame before any features of interest can be evaluated.

The geometry of the measurement is shown in Figs. 14 and 15. The laser is incident at point O and makes an angle θ in the XZ plane (we have dropped the subscript for θ and α because the description is valid for both probes) and an angle α in the YZ plane. Let the block under test have a height H (OB in Fig. 14). The probe measures range along the DO direction.

The projection of this figure on the XZ plane is shown in Fig. 15 for clarity. Let the X axis and the probe readings at O be zero. As the probe travels to B, let its reading be Hm. From the geometry shown in Fig. 14,

$$Hm = H(\sqrt{1+\tan^2\theta+\tan^2\alpha}) \qquad (1)$$

Also, because the probe has a tilt angle θ, the X axis reading at B, Xm, corresponds to that at M, OM being equal to $H\tan\theta$. Thus, the measured coordinates of the point B (Xm, Hm) is given by ($H\tan\theta$, $H(\sqrt{1+\tan^2\theta+\tan^2\alpha})$). We have to correct the measured data to obtain the true coordinates of point B (Xc, Zc) as

$$Xc = Xm - H\tan\theta = Xm - Hm\tan\theta/(\sqrt{1+\tan^2\theta+\tan^2\alpha}) \qquad (2)$$

$$Zc = Hm/(\sqrt{1+\tan^2\theta+\tan^2\alpha}) \qquad (3)$$

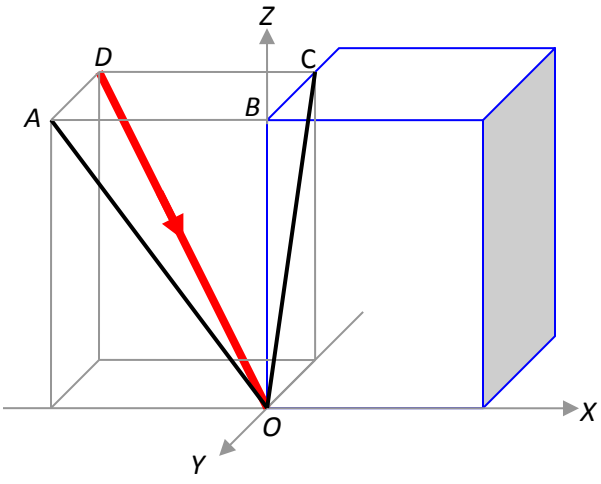

$OD = Hm$, the measured height of the block
$\angle AOB = \theta$
$\angle COB = \alpha$
$OB = H$, the true height of the block
$AB = H\tan\theta$
$BC = H\tan\alpha$

Fig. 14 *The laser is incident at an angle θ in the XZ plane and at an angle α in YZ plane.*

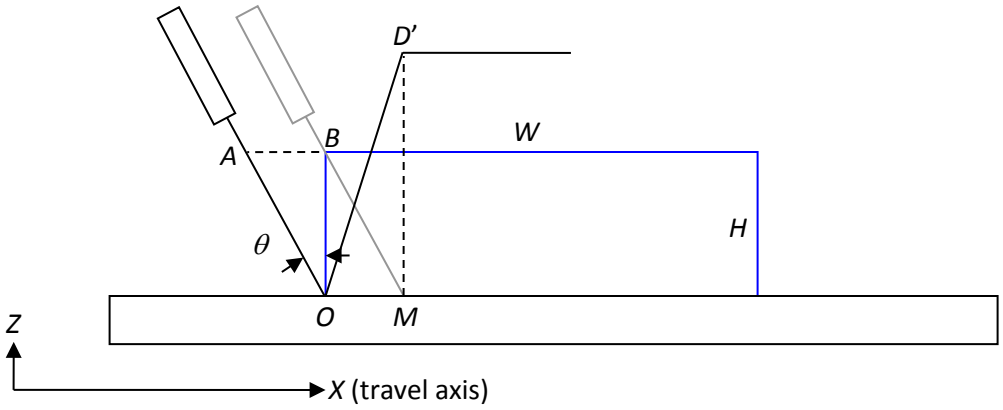

Fig. 15 *Projection on the XZ plane with the probe measuring points O and B. The X coordinate at B appears to be at M. The Z coordinate of B appears to be at D' (MD' = AO if α = 0, otherwise MD' in Fig.15 is equal to OD in Fig. 14).*

Estimating tilt angle θ from profile measurements on vertical surfaces

The tilt angle θ can be determined from vertical profile measurements as we show in this section, see Fig. 15. Let the probe read a value of zero at *O*. As the probe then travels to *B* (*OB* = *H*), let its reading be *Hm*. Because the probe has a certain tilt given by tilt angle θ, the *X* axis reading at *B* corresponds to that at *M*, *OM* being equal to $H\tan\theta$. If $\alpha = s = 0$, then $Hm = H/\cos\theta$. The apparent slope *m* in the measured data is given by

$$m = D'M/OM = AO/OM = (H/\cos\theta)/(H\tan\theta) = 1/\sin\theta \qquad (4)$$

Note that *m* is a known quantity because both *OM* (displacement along *X* as indicated by the *X* axis encoder) and *D'M* (= *AO* = *Hm*) are determined from experimental data. Therefore, an estimate θ' for tilt angle θ can be obtained as

$$\theta' = \sin^{-1}(1/m) \qquad (5)$$

When $\alpha \neq 0$ and, the measured height *Hm* is given by

$$Hm = H(\sqrt{1+\tan^2\theta+\tan^2\alpha}). \qquad (6)$$

We can then obtain an estimate θ' using Eq. 5 but that estimate will be in error. We can calculate that error for the assumptions stated in the preceding section (θ = 25°, α = 1°) using the following relation

$$\theta' = \sin^{-1}(1/m) = \sin^{-1}(\tan\theta/\sqrt{1+\tan^2\theta+\tan^2\alpha}) \qquad (7)$$

That error in θ' is -0.003°, and is substantially smaller than the 0.015° error obtained using the height block method.

A further interesting aspect of this approach is that this technique allows the separation of the effects of tilt angle θ and misalignment angle α on height measurements and therefore provides a way to estimate α also. Using the estimate θ', we can now transform the measured data into an orthogonal system as shown in section 2. Using the estimate θ', we can obtain an estimate for *Zc* as

$$Zc = Hm\cos\theta' = Hm\sqrt{(1+\tan^2\alpha)}/\sqrt{1+\tan^2\theta+\tan^2\alpha)} = H/\cos\alpha \quad (8)$$

The corrected *X* coordinate for point *B* (*Xc*) can then be obtained as

$$Xc = Xm - Zc\tan\theta' \quad (9)$$

Substituting Eqs. 10 and 11 into Eq. 12 we get,

$$Xc = Xm - Hm\sin\theta' = Xm - H\tan\theta \quad (10)$$

Implications of correcting measured data with estimate θ': Eq. 10 shows that the corrected *X* coordinate of point *B*, *Xc*, is in fact the true coordinate of point *B* (from the geometry in Fig. 15, it can be seen that $OM = H\tan\theta$). There is no error after the correction process. The *Z* coordinate of point *B* does suffer from an error. That error is inversely proportion to $\cos\alpha$. Therefore an estimate for misalignment angle α can be determined by measuring a calibrated height block. The estimate for α can then be used to revise the value of θ'. We showed earlier that assuming α = 1°, the error in θ' is -0.003°. Assuming we now measure a calibrated height block (say, 5 mm height), the estimate for the misalignment angle α is 1°. Applying this value for the misalignment angle, we can now refine the estimate for θ'; that value turns out to be exactly 25°. Therefore, in theory, we can estimate the values of α and θ accurately using the vertical profile method. Real measurements suffer from noise and other sources of uncertainty.

3.3 System validation using gage blocks

Tables 3 and 4 shows width and height errors on gage blocks using our dual-probe system. It can be seen that the errors are less than 1 μm in all instances. This suggests that we can potentially achieve extremely high accuracy in our measurements.

Table 3: Width errors on thin Mitutoyo blocks

Nominal Inches (millimeters)	Measured value (mm)	Errors (in micrometers)
0.1 (2.54)	2.5402	0.2
0.125 (3.175)	3.1744	-0.6
0.2 (5.08)	5.0791	-0.9
0.25 (6.35)	6.3501	0.1
0.3 (7.62)	7.6199	-0.1

Table 4: Height errors in μm on Webber blocks

Nominal Inchs (millimeters)	Measured value (mm)	Error (in micrometers)
0.11 (2.794)	2.7939	-0.1
0.15 (3.81)	3.8109	0.9
0.19 (4.826)	4.8251	-0.9

3.4 Comparison of non-contact probe measurements with UMAP system (contact probe)

Two graphite bipolar fuel cell plates with nominally vertical side walls were measured using both a Mitutoyo UMAP touch-probe CMM and the dual-probe laser triangulation system. The data obtained using the UMAP system is considered the reference data for the triangulation probe measurements. Each plate contained three parallel channels, each making 15 turns, for a total of 45 rows. The UMAP system was used to obtain the channel width and height of each of those 45 rows for plate # 1 and for 21 rows for plate # 2 along the centerline of the plates. The laser triangulation probes were then used to measure profiles along the same centerline, from which we calculated channel width and height. The laser triangulation probe measurements were performed at 30 mm/s with a sampling interval of 1 μm.

As mentioned earlier, laser triangulation probes are extremely sensitive to material properties and therefore, we used plate # 1 to determine the horizontal offset *w* for the probing system (the average width of all rows determined from the UMAP system was subtracted from the average width of all rows determined using the dual-laser probe system to determine the offset). We then applied this offset for plate # 2 to determine channel widths. The results are shown in Figs. 16 and 17.

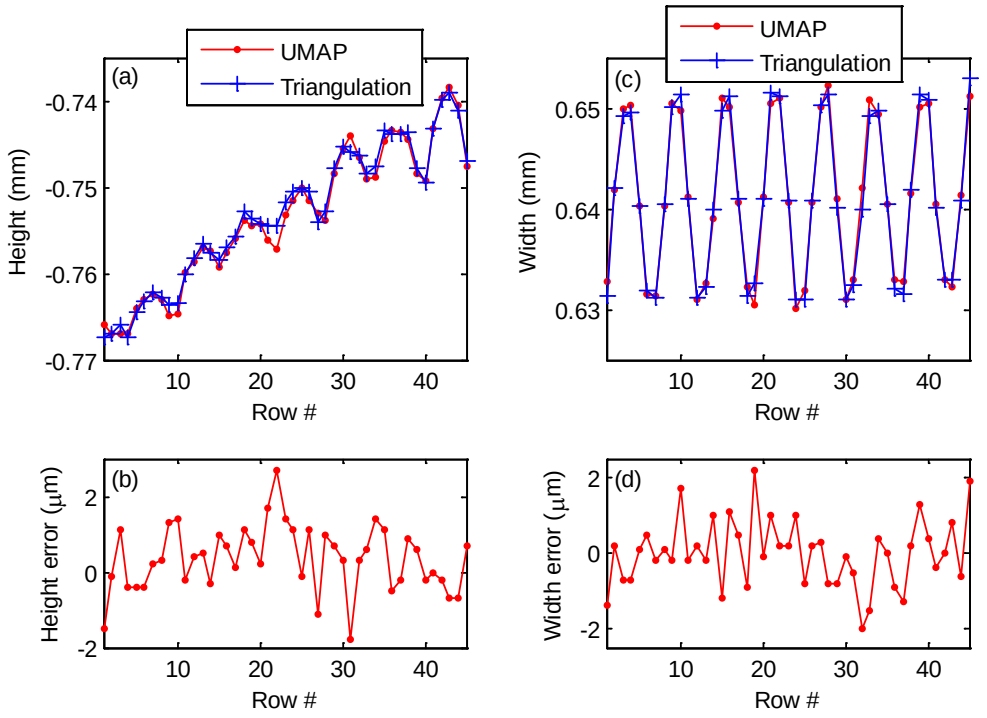

Fig. 16 *Plate # 1(a) Measured height of each row using both the UMAP and the dual probe laser triangulation system (b) Height error for each row (c) Measured width of each row using both the UMAP and the dual probe laser triangulation system (d) Width error for each row (note that the width errors shown here do not include any potential bias in the measurement because the probe offset w was determined from the measurement of this plate)*

Figs. 16(b) and 17(b) shows the height measurements with our non-contact probing system are within ±2 μm of the UMAP values. Fig. 17(d) shows that the width measurements are also within ±2 μm of the UMAP values when probe offset is calibrated with a master of similar material (in this case, we use widths values obtained from the UMAP on Plate # 1 as the master).

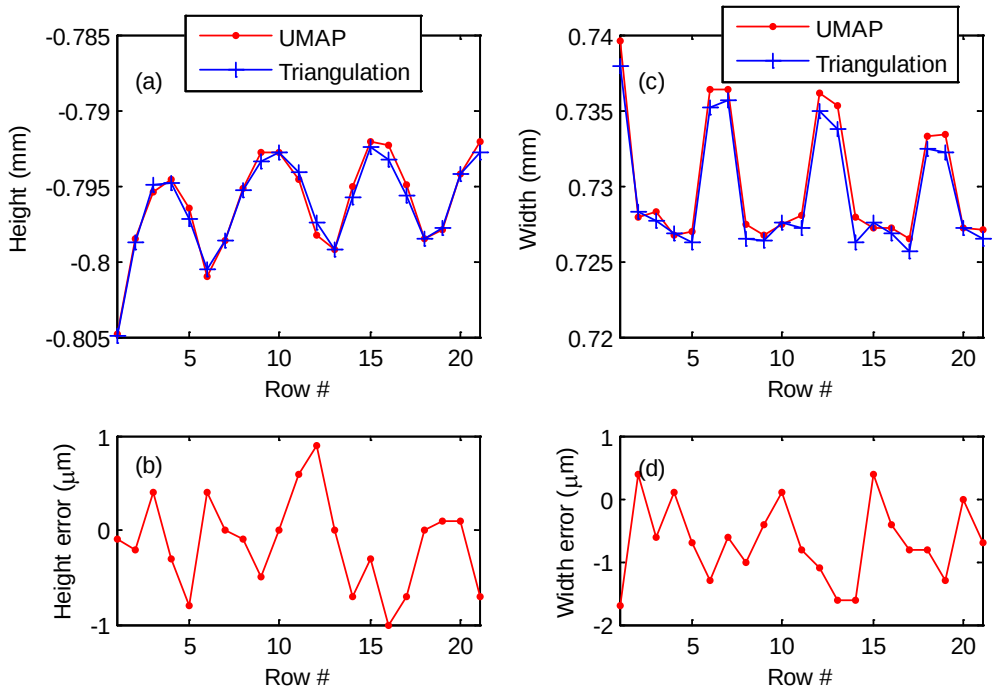

Fig. 17 *Plate # 2 (a) Measured height of each row using both the UMAP and the dual probe laser triangulation system (b) Height error for each row (c) Measured width of each row using both the UMAP and the dual probe laser triangulation system (d) Width error for each row (the errors do reflect any bias in the measurement, although none is apparent in the results)*

3.5 **Uncertainty in width and height measurements**

The error sources in a laser triangulation probe have been extensively studied before [2]. The laser triangulation probes are sensitive to bright-dark transitions, to secondary reflections near the intersection of two surfaces (such as near the intersection between a sidewall and the bottom of a channel), to material properties that cause volumetric scattering, part roughness, *etc*.

The error sources detailed in [2] impact measurements made on materials of different colors, parts with large form (for example, spherical or conical surfaces), *etc*. The measurements made on fuel cell plates however, are not affected by many of the issues described in that report. We do however notice the problem of secondary reflections near the bottom of the channel where some small portion of the data has to be discarded.

One potential source of large errors is related to the sensitivity of the probe to material properties. This may be related to the problem of volumetric scattering mentioned in [2]. In Section 5.2 we showed, via experiment, the influence of material property on the measured channel width. Because the system requires a calibration of the probe offset *w*, and this probe offset is material dependent, it becomes critical to calibrate the probe using a master made out a

material that is identical to the part under inspection. While this is a limitation of this measurement technology, it is a tradeoff to obtaining high accuracy in the measurements.

Table 5 Uncertainty budget for height and width measurements on graphite fuel cell plates with nominally vertical side walls

	Source	Uncertainty in height (μm)	Uncertainty in width (μm)
System parameters			
1	Uncertainty in the estimation of tilt angle θ	0.2	0.5
2	Uncertainty in the estimation of α	0.1	0
3	Uncertainty in the estimation of vertical offset between probes	0	
Probe			
4	Probe linearity	1.5	1.4
5	Probe repeatability	0.1	0.1
Stage			
6	*Z* straightness of the stage	0.9	
7	Pitch motion of the stage		1.0
8	Uncertainty in encoder readings		0.1
Part			
9	Part surface texture and form	0.1	0.1
10	Repeatability from parallel profiles on part	0.5	1
Alignment			
11	Non-zero α and *Y* displacement	0.4	
12	Part misalignment		0.1
13	Offset between probes along *Y* axis		0.5
Other			
14	Realizing the definition of the measurand	0.2	0.2
15	Uncertainty in the estimation of horizontal offset between probes (root sum square of above described terms)		2.1
	Combined standard uncertainty (k = 1)	1.9	3

The above uncertainty calculations are made under the assumption that channel height H = 1 mm and that the side walls are nominally vertical.

3.6 Errors as a function of measurement speed, tests at 30 mm/s and 100 mm/s

Table 6 shows the errors in width measurements on ceramic gage blocks at 30 mm/s and 100 mm/s. It can be seen that the errors at 30 mm/s and at 100 mm/s are nearly identical. Similar behavior is seen for height measurements, see Table 7. Figs. 18 and 19 show the results on height

and width measurements at the two speeds for the two graphite bipolar plates. The data at 100 mm/s is only slightly more noisier; the errors at 100 mm/s are within ±3 μm, while those at 30 mm/s are within ±2 μm.

Table 6: Width errors on ceramic gage blocks at 30 mm/s and 100 mm/s

	Error (μm)	
Nominal size (inches)	30 mm/s	100 mm/s
0.0625	3	2.3
0.1	-0.4	-0.8
0.125	-3.7	-3.4
0.2	-1	-1.1
0.25	0	0
0.3	0.7	0.3

Table 7: Height errors on ceramic gage blocks at 30 mm/s and 100 mm/s

	Error (μm)	
Nominal size (inches)	30 mm/s	100 mm/s
0.1	-1.9	-1.6
0.18	0.5	0.5
0.32	1	1

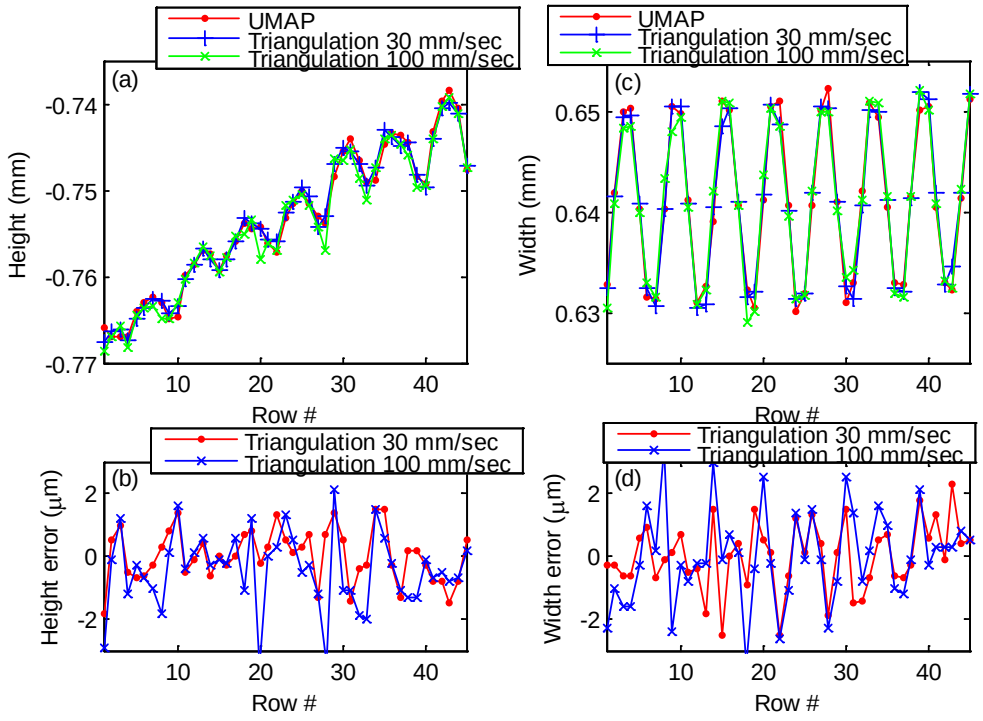

Fig. 18 *Measurement results on Plate # ZN at 30 mm/s and 100 mm/s. The depth errors are within ±3 μm.*

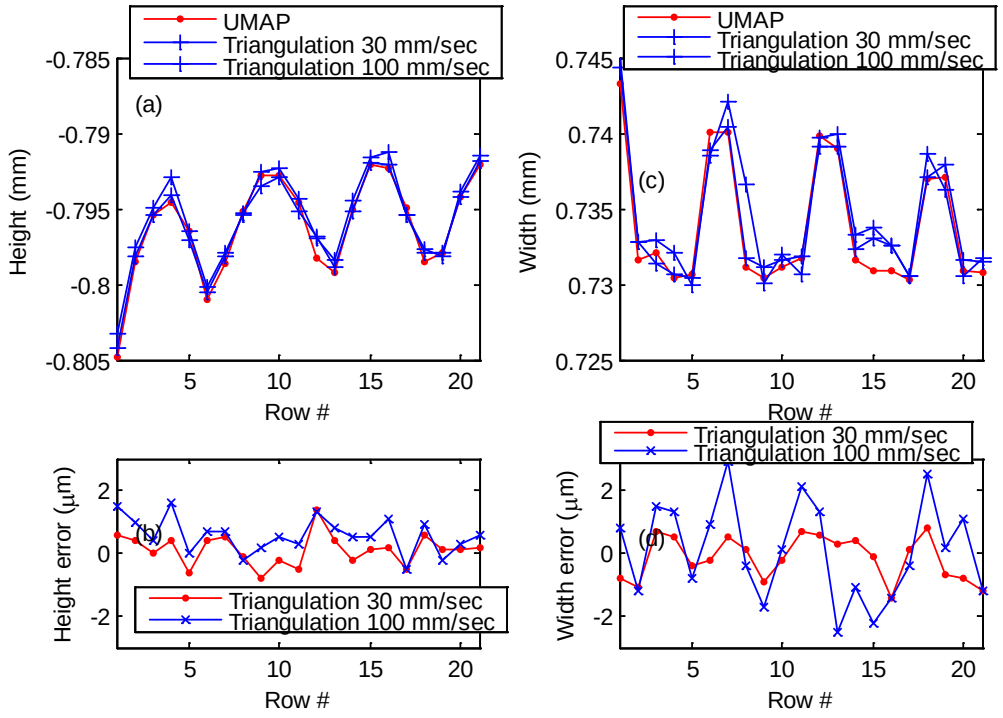

Fig. 19 *Measurement results on Plate # 1C/2 at 30 mm/s and 100 mm/s. The width errors are within ±3 μm. Depth errors are even smaller.*

3.7 Summary

In this section, we described the design, construction, and testing of a prototype system for the dimensional metrology of bipolar plate channel profiles. We presented a unique dual-probe configuration so that we can measure the side wall, and top and bottom of the channels. Our unique design requires the identification of several system parameters. We presented an approach for the calibration of these parameters and validated the system through measurements on calibrated objects such as gage blocks. We also presented a detail uncertainty budget for channel height and width. We performed measurements on actual fuel cell plates and compared those measurements to those made using a contact probe CMM. Our measurement and analysis shows width and height errors of less than ±1 μm on calibrated gage blocks and less than ±2 μm on channel width and height of fuel cell plates. We estimate an expanded uncertainty of 6 μm (k = 2) on channel width and 3.8 μm (k = 2) on channel height for graphite bipolar fuel cell plates with vertical side walls. We also compared the errors as a function of measurement speed and noticed little degradation in accuracy at 100 mm/s in comparison to 30 mm/s. We in fact tested the measurements at speeds as high as 500 mm/s and noticed acceptable accuracy levels (under 10 μm) up until 400 mm/s.

4 PLATE THICKNESS METROLOGY

4.1 System prototype

Plate thickness measurements can be performed using two probes in an arrangement shown in Fig. 20. The fuel cell plate is mounted on a raised platform on the translation stage. The two probes are mounted so that one probe measures the plate from the bottom while another measures from the top. The probes are aligned so that their lasers are along coincident vertical lines. Any deviation from this condition will result in measurement errors. We discuss methods to characterize these errors in the next section. It should be noted that opposed point thickness measurements requires two probes and so does channel width/depth measurements (for which we use two probes tilted in opposing directions but both looking down on the part). With the availability of additional probes, we will have the ability to perform all measurements in one setup.

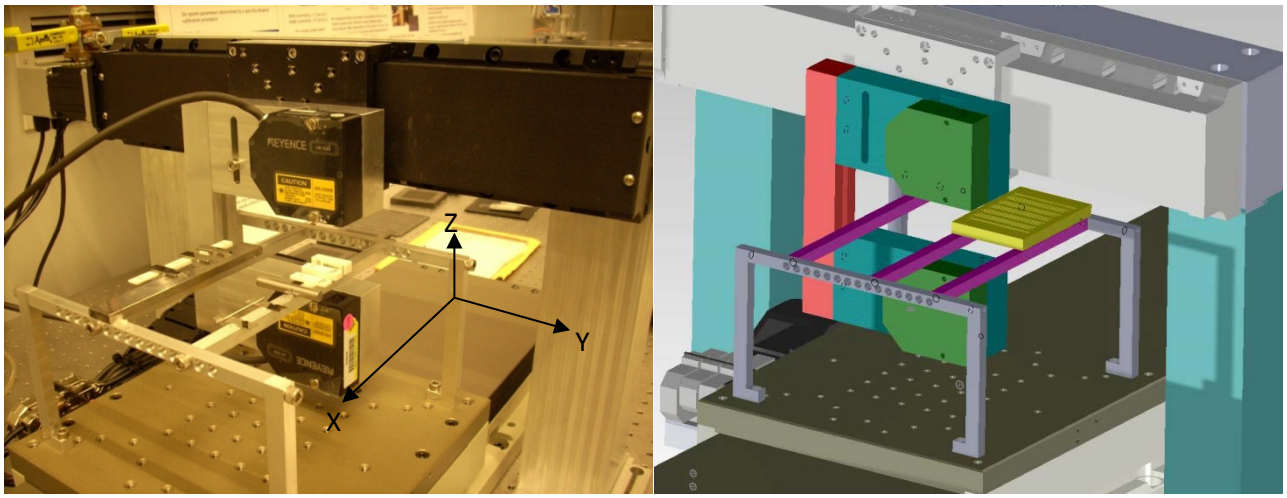

Fig. 20 *Photo and schematic of opposed probe configuration for thickness measurements.*

4.2 System parameters and calibration

There are several sources of error in our measurement. We describe these error sources and present an uncertainty budget here. We consider the following sources of error in thickness measurements:

1. *X, Y, Z* offsets for both top and bottom probes.
2. Tilt angles in *YZ* plane for both top and bottom probes.
3. Tilt angles in *XZ* plane for both top and bottom probes

The offset error occurs when the two probes do not read zero at the same point in space. This separation may be resolved along the X, Y, and Z directions. We compensate the measured data for the X and Z offsets as discussed below. We also present a method to estimate the Y offset; this is later used in the uncertainty budget. While we estimate the tilt angles of the probes, we do

not compensate the measured data; we simply use the estimates in the uncertainty budget for thickness.

Probe Z offset

Since thickness measurement is really the sum of the readings of the two probes, a Z offset error will directly affect thickness measurements. While measuring the thickness of one calibrated gage block (and comparing against known thickness) will provide an estimate of this offset, we measure thickness of multiple blocks and determine an average offset.

Probe X and Y offset

The X offset calibration is performed by mounting a cylinder so that its axis is parallel to the Y axis. The two probes then scan a profile across this cylinder. Best fit circles are constructed on the data and the shift along the X axis is used as the estimate for the X offset. In order to estimate the Y offset, a disk with sharp edges is placed on the table and scans are performed on chords away from the largest diameter (all scans are along X axis). From the measured chord lengths for the two probes (L_1 and L_2), and the known disk radius R, we estimate the Y offset.

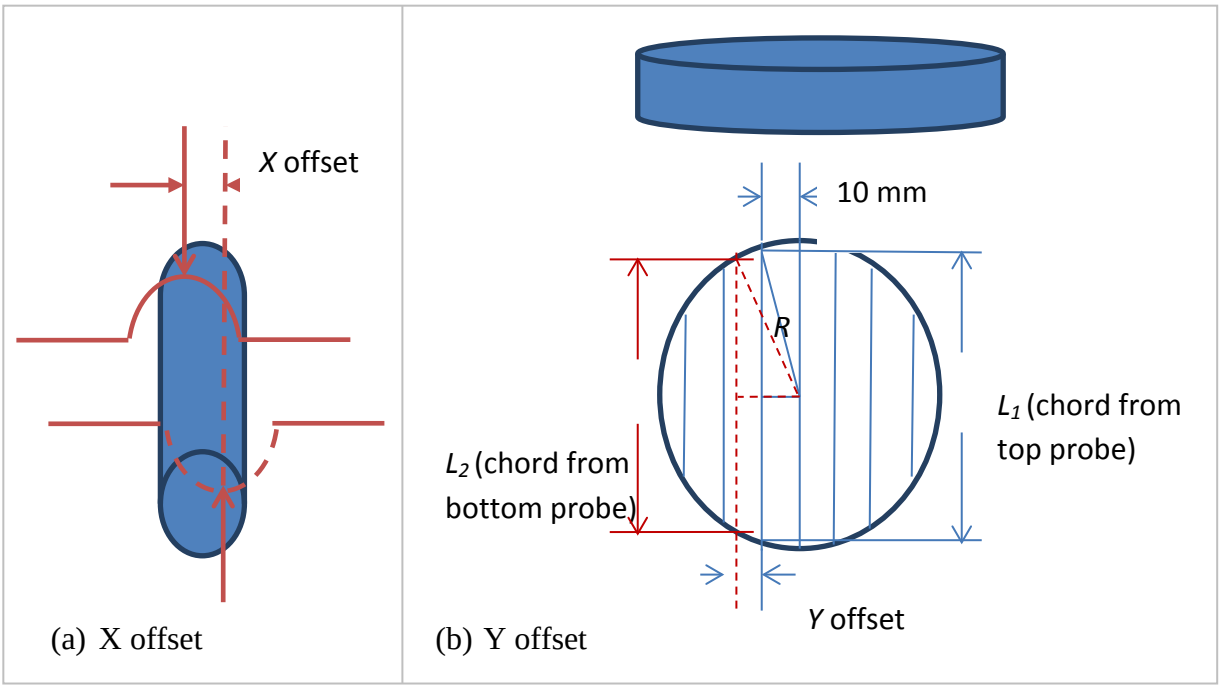

Fig. 21 *Estimating the X and Y offsets.*

Tilt angles

The probes can be tilted in both the XZ and the YZ planes. We estimate the magnitude of the tilts by measuring the thickness of several gage blocks of known thickness. Tilted probes will produce a larger measured thickness. This produces an upper bound on the tilt angle for the

probes. We manually adjust the tilt to obtain an upper bound of ±3º on the probe tilt and use this value in the uncertainty budget for thickness measurements.

4.3 Uncertainty budget for thickness measurements

We describe an uncertainty budget for thickness measurements of a nominal 4 mm thick gage block using our opposed probe configuration here.

Laser triangulation probes are sensitive to material/optical properties of the test artifact and suffer from linearity errors. Assuming the Z offset calibration suffers from a ±5 µm error due to the difference in material properties between the calibration artifact and the test artifact, and assuming a rectangular distribution, the standard uncertainty in the offset calibration will be $5/\sqrt{3} = 3$ µm. The manufacturer's specification for probe linearity is also ±5 µm, and therefore assuming a rectangular distribution, the standard uncertainty in thickness measurements will be $5/\sqrt{3} = 3$ µm.

The X and Y offsets will not introduce an error when measuring perfectly flat/parallel gage blocks if the block is aligned to have no tilt. On the other hand, if the block is tilted (we are assuming a bound of ±3º for the tilt and a rectangular distribution), and assuming a 50 µm error in the calibration of the X and Y offset, we estimate a standard uncertainty of 5 µm in thickness due to these offsets.

Assuming a bound of ±3º for the probe tilt in the XZ and YZ planes, we estimate a standard uncertainty of 3.5 µm for thickness of the 4 mm thick gage block due to probe tilt.

It is not clear yet how the stage motion errors will contribute to thickness measurement errors. Z straightness errors may not contribute much to thickness errors since it affects both probes in the same way. The rigidity (or lack of) of the fixture that holds the plate will perhaps contribute to thickness measurement errors, but we have not yet determined its precise influence. We are currently operating the stage at 30 mm/s. Increasing the speed will deteriorate measurement accuracy unless a more rigid fixture is designed.

Combining the terms above, we estimate a combined standard uncertainty of 10 µm, or an expanded uncertainty of 20 µm ($k = 2$) on thickness.

4.4 System validation using gage blocks

We measured several gage blocks of known thickness. The results are shown in Table 8. The largest observed errors were on the order of 7 µm.

Table 8 Results from measurements on gage blocks

	Nominal	Dev from Nominal (mm)
Webber	0.13 in	-0.0067
Webber	0.25 in	-0.0051
Mitutoyo	0.17 in	-0.0014
European	4 mm	-0.0020

4.5 Comparison of non-contact probe measurements with contact probe CMM

We took a thin stamped fuel cell plate and cut it by EDM perpendicular to the length of the channels approximately 1 mm away from the marked line scanned/measured with the non-contact measurement system. This was done so that the contact probe CMM can access the same location on the channels measured by the non-contact probe. The CMM data is used as the reference for comparison purposes.

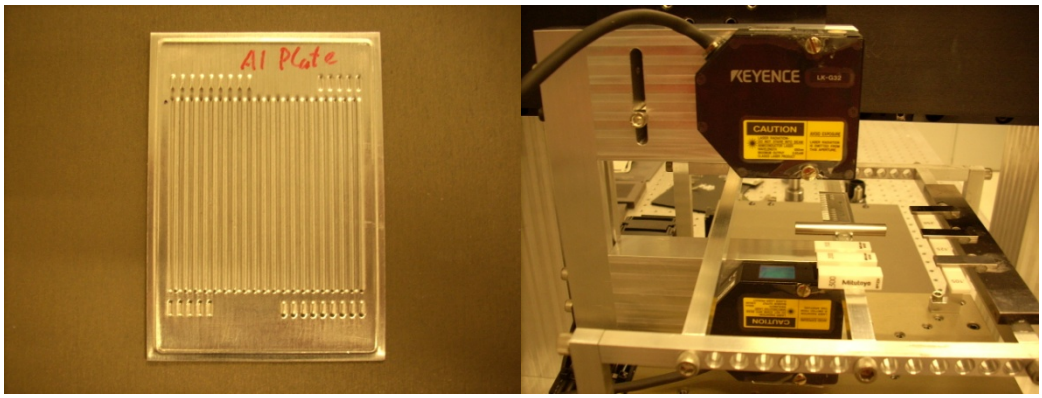

Fig. 22 *(a) Fuel cell plate (b) Dual non-contact probes*

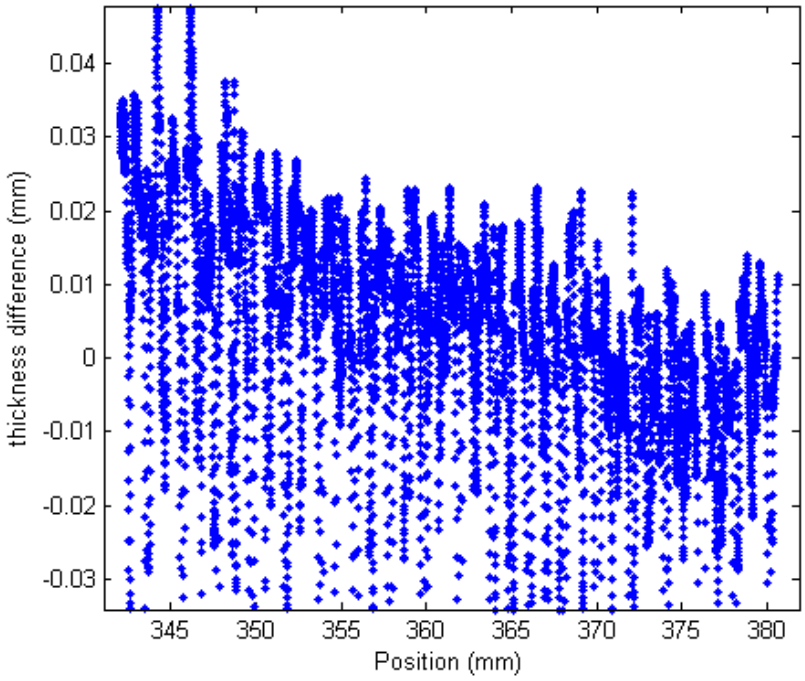

Fig. 23 *Thickness difference between touch probe and non-contact probe*

Fig.23 shows the thickness difference between the non-contact and the CMM data. Most of data points are within a 20 µm bandwidth, which is the thickness difference of top and bottom of the channels between two systems. For clarity, Fig. 24 shows the thickness differences at the top and bottom of the channels only.

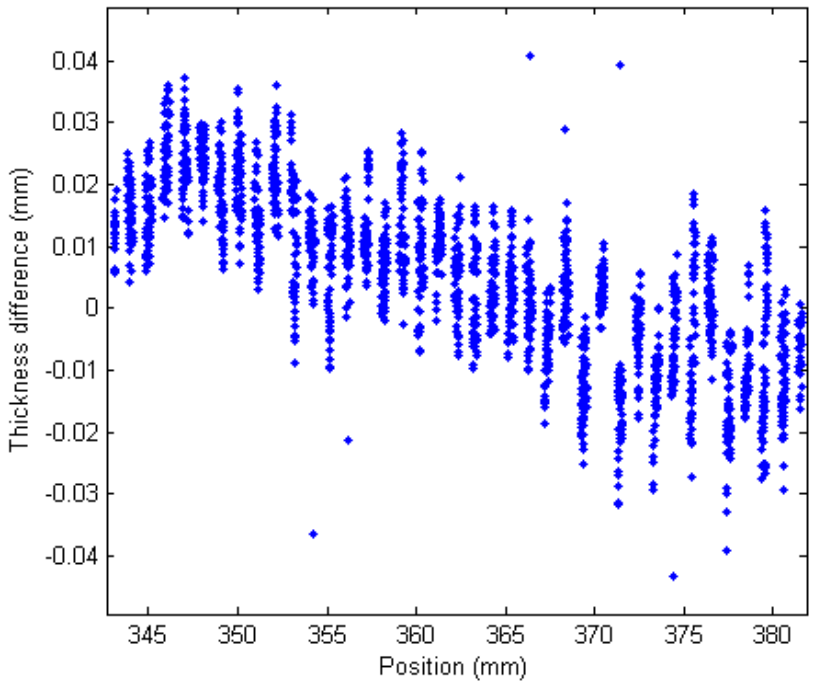

Fig. 24 *Thickness difference only at top and bottom part of the plate*

4.6 Summary

In this section, we described the measurement of plate thickness using an opposed probe configuration. We presented an approach to calibrate the different system parameters, discussed error sources, and tabulated an uncertainty budget. The expanded uncertainty in the thickness measurements for a nominal 4 mm gage block was determined to be 20 µm (k = 2). We compared measurement results obtained using our system to those obtained using a contact probe system on a thin stamped Aluminum plate, and the thickness differences were within 20 µm.

5 ANALYSIS OF NON-CONTACT DATA FROM FREE FORM CHANNEL PROFILES

During this period, we also developed mathematical techniques for the analysis of data from free form channel profiles. Profile filtering is generally used in surface texture analysis to partition a profile into different wavelength regimes such as roughness, waviness, and form. In dimensional analysis of high density data, filtering techniques can be applied to not only suppress measurement noise, but also used in outlier identification and removal and in the creation of a substitute geometry. In this work, we show how several recently introduced filters (spline, morphological, robust Gaussian regression) can be employed as enabling tools in the dimensional measurement of a fuel cell plate, where high density data is acquired using non-contact probes. We demonstrate how robust Gaussian regression and spline filters may be used to identify and suppress outliers and create a substitute geometry from which parameters of interest such as channel depth and width may be evaluated. We also show how morphological

filters are useful in correcting probe tip effects, and also show how the free form geometry of these flexible plates can be corrected using Gaussian regression filters without loss of edge data. As high density non-contact probe measurements become more prevalent, the distinction between dimensional and surface texture analysis will become less marked, and filtering techniques will be more commonly applied in the dimensional measurement and analysis of engineering artifacts.

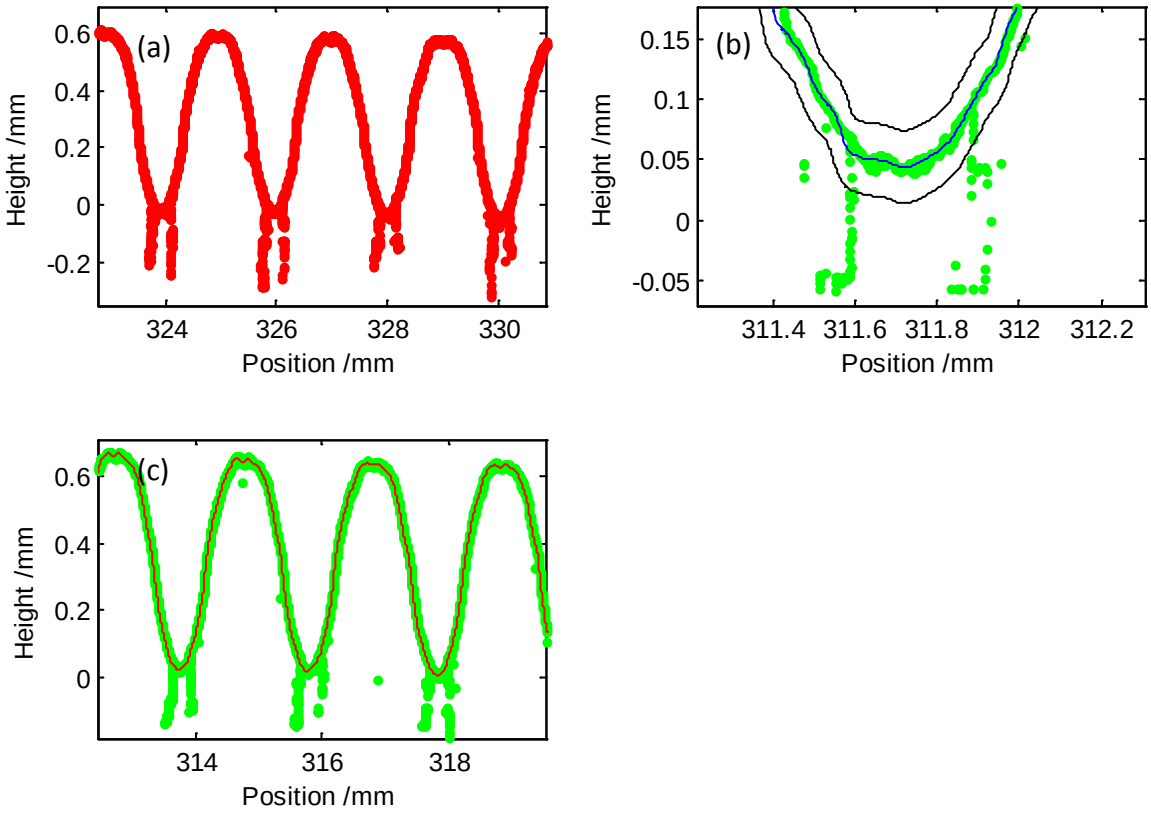

Fig. 25 *(a) Raw profile from non-contact system (b) robust Gaussian regression mean line along with an upper and lower boundary profiles for outlier identification (c) Spline mean line (the red line) after outlier identification and removal.*

We present here an overview of the methods in the context of a profile measurement made on a stamped fuel cell plate. The non-contact probe data across a channel are noisy, see Fig. 25. In addition, the data at the bottom of the channels show several streaks due to secondary reflections. The first task in the analysis of these data is to identify and remove outliers, and to create a substitute geometry. For this purpose, we first generate a mean line using the robust Gaussian regression filter with 0.08 mm cutoff. The robust filter is not influenced by small outliers and produces a mean line that reasonably hugs the texture. It may still be influenced somewhat by the large streaks of data at the bottom of the channels. In order to identify the data that comprise these large streaks and outliers, we then create two profiles that are displaced by a certain threshold (chosen by trial and error as 30 µm; this value is chosen to allow small surface features

to remain while omitting large outliers) from the Gaussian regression mean line. Simply translating the Gaussian regression mean lines above and below will produce an unequal spacing at the sidewalls and the top/bottom because of the different surface slopes. We therefore create morphological dilation and erosion profiles from the Gaussian regression profile; these serve as the upper and lower limits for the data points that represent the actual surface. Any points lying outside these limits are considered as outliers and are discarded. We then filter the resulting data set using a spline filter with 0.08 mm cutoff to obtain the substitute geometry.

We then remove the free form geometry of the plate using a robust Gaussian regression filter of 8 mm cutoff. The robust filter is not sensitive to edge effects and therefore, we do not have to discard the first and last half cutoffs. The profile and the robust Gaussian regression mean line are shown in Fig. 26(a), and the form removed profile is shown in Fig. 26(b).

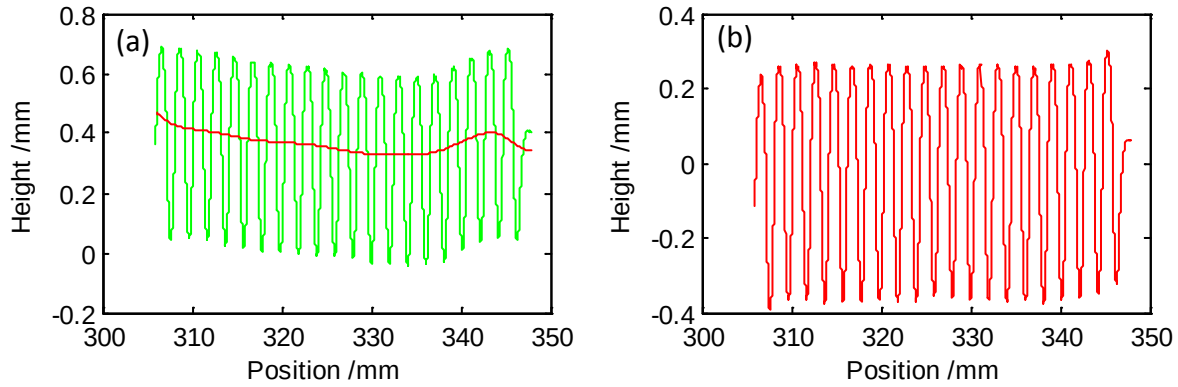

Fig. 26 *(a) Profile and the robust Gaussian regression mean line with 8 mm cutoff (b) Form removed profile*

The form removed profiles obtained from both the CMM and the non-contact probe are shown in Fig. 27. Because the two profiles are obtained from different instruments and therefore different coordinate systems, we determine the best overlap position using cross correlation. We then determine the vertical point-to-point differences between the profiles. The mean and standard deviation of these point-to-point differences are 1.5 µm and 10 µm, respectively. Most of the large differences happen at the side walls where the non-contact probe measures the surface at a grazing angle and therefore produces larger measurement errors [2]. The small value for the mean difference suggests that there is no bias (or vertical shift) between the two profiles.

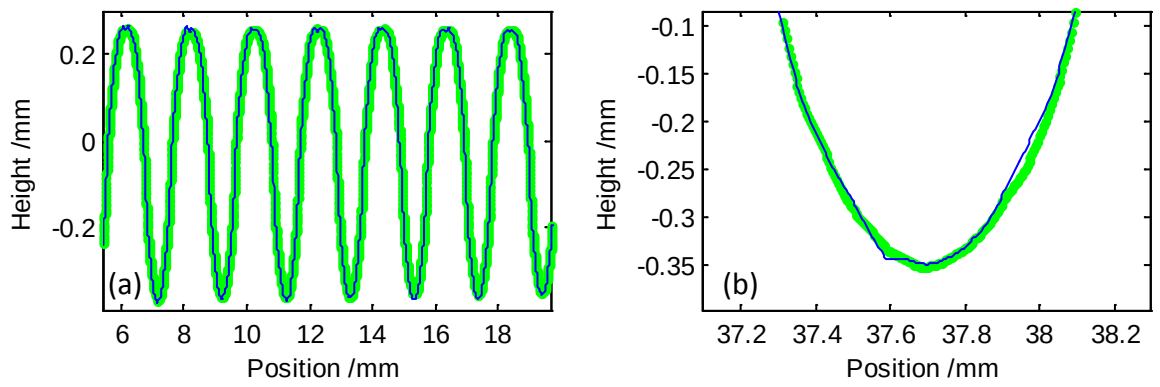

Fig. 27 *Form removed profiles from both the CMM (shown as a series of green dots) and the non-contact probe (shown as a solid blue line) (a) over a 14 mm portion of the profile (b) over just a 0.8 mm portion of the profile*

We define channel height as the distance between the average *Z* position of the two consecutive peaks to the valley between them. Because the channels have no land area, we consider the average over a 0.1 mm region, centrally located at the peak or valley, as the measure of the Z position. We calculate the channel heights for each of the seventeen channels, for both the CMM and the non-contact probe data, and then compute the differences. These differences range from -8 µm to 15 µm, with a mean difference of 5 µm and a standard deviation of 6 µm. The positive mean difference of 5 µm suggests that the non-contact probe may be estimating channel heights slightly larger than the contact probe CMM measurements, but nevertheless, this value is small in comparison to the linearity of the probes themselves, which is specified at ±5 µm.

6. CONCLUSIONS

As fuel cell plate manufacturing volume increases, there will be a need rapid cost effective non-contact measurement system that can be used for in-line process control. Manufacturers currently either visually inspect plates or use machine vision systems for verifying tolerances. Such methods do not provide the sub-10 µm accuracy that manufacturers are targeting. In this context, we have developed a prototype system that has been extensively tested and documented. The key technical features of our system and methods are:

- Developed using commercially available stages and triangulation probes
- Total system cost under $50,000
- Extensively documented error sources and constructed detailed uncertainty budgets that are available in the public domain
- Measurement capability includes channel profiles, height, width, side wall, top surface flatness, plate thickness, variation in thickness, etc.
- Measurement uncertainty on channel height and width of graphite bipolar plates are 6 µm (k = 2) on channel width and 3.8 µm (k = 2) on channel height
- Measurement uncertainty on thickness are 20 µm (k = 2) on artifacts with high quality surfaces.

- Measurement speeds tested ranged from 30 mm/s to 500 mm/s, with no noticeable degradation in accuracy until 400 mm/s.
- Developed mathematical techniques to process high density non-contact data across channels to determine features of interest such as height and width.

7. REFERENCES

1. Buzinski, M., Levine, A., Stevenson, W.H., Performance characteristics of range sensors utilizing optical triangulation, IEEE 1992 National Aerospace and Electronics Conference, 1230-1236 (1992).
2. A. Garces, D. Huser-Teuchert, T, Pfeifer, P Scharsich, F. Torres-Leza, E Trapet, Performance test procedures for optical coordinate measuring probes, Final project report, part 1, July 1993, European Communities Brussels, Contract No. 3319/1/0/159/89/8-BGR-D (30)
3. Xi, F., Liu, Y., Feng, H.-Y., Error compensation for three-dimensional laser scanning data, Int. J. Adv. Manuf.Technol., 18, 211-216 (2001).
4. Nick Van Gestel, Steven Cuypers, Philip Bleys, Jean-Pierre Kruth, A performance evaluation test for laser line scanners on CMMs, Optics and Lasers in Engineering 47(2009)336–342
5. Gabriele Guidi, Fabio Remondino, Giorgia Morlando, Andrea Del Mastio, Francesca Uccheddu, Anna Pelagotti, Performance evaluation of a low cost active sensor for cultural heritage documentation, Optical 3-D measurement techniques VIII, ISBN 3-906467-67-8, Vol 2, 2007, pp 59-69
6. Gabriele Guidi, Michele Russo, Grazia Magrassi and Monica Bordegoni , Performance Evaluation of Triangulation Based Range Sensors, *Sensors* 2010, *10*, 7192-7215
7. K-C Fan, A non-contact automatic measurement for free-form surfaces, Computer Integrated Manufacturing Systems, 10 (4), p 277-285, 1997
8. Godin, G., Rioux, M., Beraldin, J.-A., Levoy, M., Cournoyer, L., 2001: An Assessment of Laser Range Measurement of Marble Surfaces. Proceedings of the 5th Conference on Optical 3-D, Measurement Techniques, pp. 49-56, Vienna, Austria

8. PRODUCTS DEVELOPED UNDER THE AWARD AND TECHNOLOGY TRANSFER ACTIVITIES

Publications

Bala Muralikrishnan, Wei Ren, Eric Stanfield, Dennis Everett, Alan Zheng, and Ted Doiron, Applications of Profile Filtering in the Dimensional Metrology of Fuel Cell Plates, Measurement Science and Technology, 24(6), 2013

B. Muralikrishnan, W. Ren, D. Everett, E. Stanfield, T. Doiron, Performance evaluation experiments on a laser spot triangulation probe, Measurement: Journal of the IMEKO, 45(3) 2012, 333-343

Ted Doiron, Wei Ren, Eric Stanfield, Bala Muralikrishnan, and Chris Blackburn, Some high

accuracy measurements using a scanning system with a single point triangulation sensor, NCSLI Measure, 7 (4) 2012, pp. 34-39 (from the Proceedings of the NCSLI 2012)

B. Muralikrishnan, W. Ren, D. Everett, E. Stanfield, T. Doiron, Non-contact dimensional measurements of bipolar fuel cell plates, Annual meeting of the ASPE 2011, Denver CO.

B. Muralikrishnan, W. Ren, D. Everett, E. Stanfield, T. Doiron, Dimensional Metrology of Bipolar Fuel Cell Plates Using Laser Spot Triangulation Probes, Measurement Science and Technology, 22(7), July 2011

Presentations

Bala Muralikrishnan, Wei Ren, Dennis Everett, Eric Stanfield, and Ted Doiron, Dimensional Metrology of Bipolar Fuel Cell Plates Using Laser Triangulation Probes, poster presentation at the 2011 Fuel Cell Seminar, November 2011

Stocker, Stanfield, and Muralikrishnan, Metrology for Fuel Cell Manufacturing, Presentation to the FreedomCar Tech Team, March 16, 2011

Instruments or equipment

We purchased two Keyence LK-G32 laser spot triangulation probes, an Aerotech ALS 50060 stage for the *X* axis and an Aerotech PRO 115 stage for the *Y* axis. They are shown in Fig. 28.

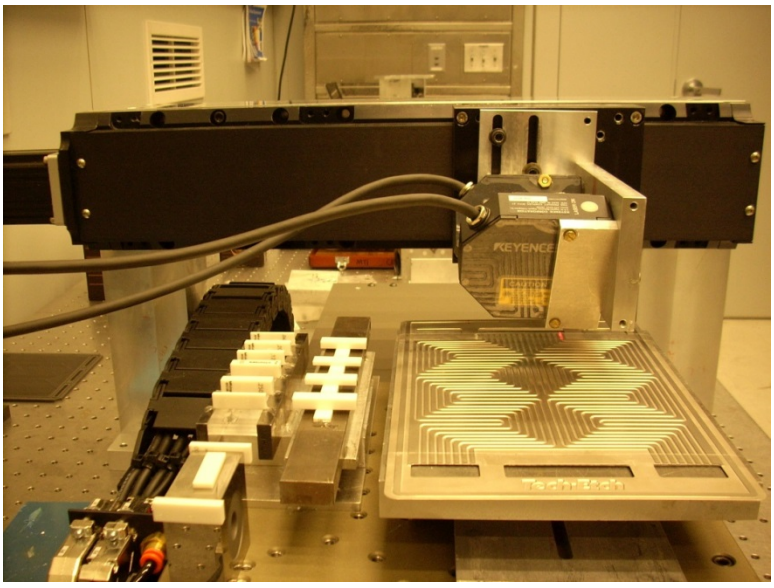

Fig. 28 *Equipment purchased through the award*

Networks or collaborations fostered

Faraday Technologies received an SBIR to investigate application of their patented pulsing electric field technique to optimization of chemical etching SS plates. We provided first evaluation of their plates in 2011. We received second set of plates and performed measurements and submitted a report to them in 2012.

TreadStone Technologies provided us with three different plates and we have measured them and provided results.

Numerous companies expressed interest in working with us at the Fuel Cell Seminar in 2011: **Dana Corporation** Germany, **3M**, **EnerFuel** in Florida, and **FuelCell Energy** in Connecticut. Both **Ballard** and **UTC Power** have engaged us to apply our capabilities in support of their plate manufacturing proposals.

Zeiss has expressed an interest in measuring fuel cell plates using their X-ray CT system and we are in the process of providing them some plates.

DISCLAIMER

Commercial equipment and materials are identified in order to adequately specify certain procedures. In no case does such identification imply recommendation or endorsement by the National Institute of Standards and Technology, nor does it imply that the materials or equipment identified are necessarily the best available for the purpose.

Subproject #3: Optical Scatterfield Metrology for Online Catalyst Coating Inspection of PEM Soft Goods

EXECUTIVE SUMMARY

The Department of Energy's (DOE) Fuel Cell Technologies Office (FCTO) Multi-Year Research, Development and Demonstration Plan (MYRDD) continues to identify *Low Levels of Quality Control and Inflexible Processes* as a key technical barrier in facilitating the widespread commercialization of fuel cells. From the onset, the objective of this project was to evaluate the suitability of Optical Scatterfield Metrology (OSM) as a suitable measurement tool for in situ process control of catalyst coatings. OSM is an optical microscopy technique developed at the National Institute of Standards and Technology (NIST). The technique enables dimensional measurement of sub-resolved features (smaller than the Rayleigh Resolution limit) by combining the high-magnification aspect of a bright-field microscope and the wavelength/angle control of a scatterometer. OSM was initially applied to optical measurements of micro- and nanometer scale semiconductor patterned repeating structures and has enjoyed a great deal of success in this arena. The successful application of OSM to the measurement of non-patterned, random catalyst coatings was the focus of this project. From our studies, both experimental and theoretical, we proved that OSM is sensitive to variations in catalyst loadings, on the order of 0.01 – 0.05 mg Pt/cm2, on PEM catalyst coated membrane (CCM) samples. From these investigations, we optimized a scatterometry-based instrument that was designed specifically for fuel cell research with potential scalability for manufacturing called the Large Aperture Projection Scatterometer (LAPS). With the LAPS, we were able to measure Pt loading variations at simulated webline speeds of 4 ft/min. There is nothing in principle impeding the measurement technique from measuring at fuel cell industry benchmark webline speeds of 30 ft/min.

COMPARISON BETWEEN ACTUAL ACCOMPLISHMENTS WITH THE GOALS AND OBJECTIVES

The objective of this project was to evaluate the suitability of OSM as a viable measurement tool for in situ process control of catalyst coatings. Samples were to be provided by industrial collaborators with variations in critical parameters (i.e. Pt and Pt alloy catalyst loading) and the inclusion of various types of defects. The research effort focused on verifying sensitivity of the OSM technique to performing platinum loading measurements on various samples, including Pt nanoparticle on carbon CCM samples and nano-structured thin film (NSTF) CCM samples from 3M. This phase included a broad array of experimental measurements and theoretical simulations. We were successful in demonstrating industrially relevant Pt loading sensitivities on the order of 0.01 mg Pt/cm^2. Electromagnetic scattering simulation capabilities were developed and improved via new model constructs and optical properties (*n & k*) measurements of CCM constituent materials. A new process control instrument was designed and built at NIST called the Large Aperture Projection Scatterometer (LAPS) that addresses various challenges in measuring Pt loading while providing a path for industrial scalability. It was also designed to

enhance localized intensity variations that are required for indicating the presence of localized macroscopic defects sub millimeter and larger. We met the objective of evaluating the suitability of the OSM technique for catalyst loading. We went beyond the objective listed above in applying what we learned to make a new instrument better suited to perform catalyst coating process control.

PROJECT SUMMARY

The project summary is organized as follows. We present an overview of the work in the Introduction in section 1. Results are reported chronologically by fiscal year for the project. Sections 2 through 5 describe the fiscal year results from 2010 to 2013 respectively. The contents are listed below.

1. Introduction
2. Fiscal Year 2010 Activities and Results
3. Fiscal Year 2011 Activities and Results
4. Fiscal Year 2012 Activities and Results
5. Fiscal Year 2013 Activities and Results
6. Conclusions
7. Future Work
   7.1 Theoretical and modeling work
   7.2 Experimental and instrumentation work
8. References
9. Products developed under the award and technology transfer activities

1. Introduction

The need for high-speed, in situ process control measurement techniques for controlling the quality of the platinum-based catalyst layer has been identified during numerous DOE sponsored and non-DOE sponsored workshops. Current techniques for the measuring variations in the various parameters of interest (e.g., scanning electron microscopy [SEM] and X-ray fluorescence [XRF]) are extremely expensive and not easily amenable to in situ application in a manufacturing production line. The Semiconductor and Dimensional Metrology Division (SDMD) of the Physical Measurement Laboratory (PML) at the National Institute of Standards and Technology (NIST) has created a technology called OSM [1] which has been developed as a process control technique for the semiconductor industry. One key aspect of OSM is the tailoring of the illumination at the sample of interest so that the desired measurement is optimized. This process is typically realized in a bright-field optical microscope, and this tailoring of the illumination in essence yields a combination of the best attributes of optical microscopy and scatterometry.

More precisely, this technique takes traditional optical metrology beyond the Rayleigh resolution criteria and focuses on the complex optical signatures of sub-wavelength size features. With a scatterfield-capable microscope, we can collect this type of data as a function of illumination angle of incidence, illumination source wavelength, focus height, and illumination source polarization state. Consequently we can study samples, both experimentally and theoretically, as a function of these parameters in order to identify parameter values that optimize the measurement system's sensitivity to a given measurand. In figure 1 (a) is a schematic of a scatterfield microscope. The incremental positioning of the black aperture in the beam path enables angle-resolved scans of samples. A picture of the NIST Scatterfield microscope is shown in figure 1 (b).

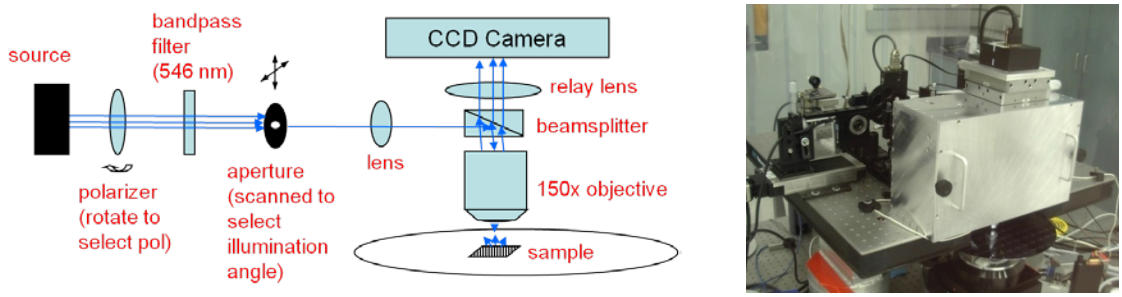

Figure 1. *(a) Schematic of a scatterfield capable microscope with aperture in illumination path for conducting angle-resolved scans, (b) Picture of the NIST Scatterfield microscope*

Prior to this project, this technique was in general applied to discrete, uniformly repeating structures as typically encountered in the semiconductor industry. Applying the OSM technique to random sub-wavelength structures has long been a goal, but this randomization presents inherent challenges. Even so, the underlying principles in this project are 1) that random sub-wavelength structures exhibit some type of repeatable optical signature, and 2) changes in these signatures can be correlated with changes in the various manufacturing parameters of interest to control the quality of the product. The overall goal of this project was to provide PEM, CCM and gas diffusion electrode (GDE) manufacturers with an automated high-throughput approach for performing process control inspection of Pt loading with sensitivity equal to or better than that currently provided with XRF and other parameters of interest simultaneously. **For dual-side simultaneous catalyst-coating operations, this method will provide the ability to concurrently perform Pt loading measurements on both sides of a CCM independently.** In contrast, XRF penetrates the membranes and yields a "total" sample loading measurement.

The OSM technique employs both simulation and physical measurement of samples. Simulation is a key aspect of the approach as it allows one to develop quantitative accuracy out of these sub-resolved optical signatures. Computational studies also provide a flexible and efficient platform

to evaluate and optimize measurement parameters even before samples are measured. Experimentally, the approach involved acquiring angle and wavelength resolved data on one of three in-house custom designed and fabricated scatterfield capable microscopes, a commercial ellipsometer, or a completely new in-house designed and built fuel cell research measurement instrument called the Large Aperture Projection Scatterometer (LAPS).

Through the four year duration of this project, there were three core areas of research that were pursued: 1) demonstrating the experimental sensitivity of OSM for its suitability as an in situ process control tool for catalyst coated fuel cell soft goods, 2) developing the necessary electromagnetic scattering simulation capability of various PEM soft goods, and 3) optimizing a new scatterometry-based process control instrument, designed and built specifically within this NIST fuel cell research effort. The experimental and theoretical accomplishments for the OSM technique as well as the accomplishments regarding the new LAPS instrument are presented below. The first two of these goals were addressed in FY 2010-2012, with the third core area yielding a prototype instrument in FY 2013.

Throughout the span of this project, our research has benefitted from buy-in and sample support from MEA manufacturers, as well as other experts in the field. From the beginning, we have actively engaged MEA manufacturers and industry experts in an effort to identify the critical parameters of the catalyst layer and to solicit from them sample packages that vary these parameters to enable us to conduct a sensitivity study of the proposed technique. Industry collaborators have included 3M, W. L. Gore, Hawaii National Energy Institute (HNEI), and the National Renewable Energy Laboratory (NREL).

The nature of the collaboration with NREL and its leveraging effect is notable. Specifically, we developed a collaborative agreement between NIST and NREL the two organizations. This agreement was described in a one-page summary that we sent to all of our industry partners in the fall of 2009. This summary explained a coordinated effort for achieving each of our project's goals justified by the related but complimentary nature of the NIST and NREL projects. This relationship enabled us to leverage our relationship with our industry partners together to maximize efficiency through the sharing of samples and information. In many cases non-disclosure agreements were streamlined among NREL, NIST, and industrial partners as our industry technical partners concurred with the proposed benefits and several NDAs were completed in this successful interagency relationship.

2. Fiscal Year 2010 Activities and Results

In 2010, our efforts were focused on simulation model development and experimental data collection based on 3M's NSTF CCM, the first sample set we received from a major supplier.

This first sample set included three NSTF CCMs with PtCoMn catalyst loadings of 0.10 mg/cm^2, 0.15 mg/cm^2, and 0.20 mg/cm^2. Experimentally we collected data which successfully demonstrated that the OSM technique is sensitive to catalyst loading. Multiple measurements were made on several scatterfield-capable microscopes. These microscopes yielded the necessary span of wavelength variation and angular illumination control to determine optimized measurement conditions. Activities leading up to successful measurements included developing custom data acquisition and analysis code, careful alignment and characterization of our scatterfield tools, making supporting SEM measurements to verify sample quality, and experimenting with sample mounting techniques. Figure 2 shows angle-resolved reflectivity data from this sample set. **The sensitivity of the technique for this specific CCM is on the order of 0.01 mg/cm^2**. This is very comparable to the inline XRF systems available. Figure 2 shows the final reflectivity data for two different runs. The first run involves three repetitive measurements at the same location on each sample (figure 2 (b)) thus representing what we refer to as base repeatability. The second run involves three repetitive measurements on each sample (figure 2(c)), but each measurement is at a different location.

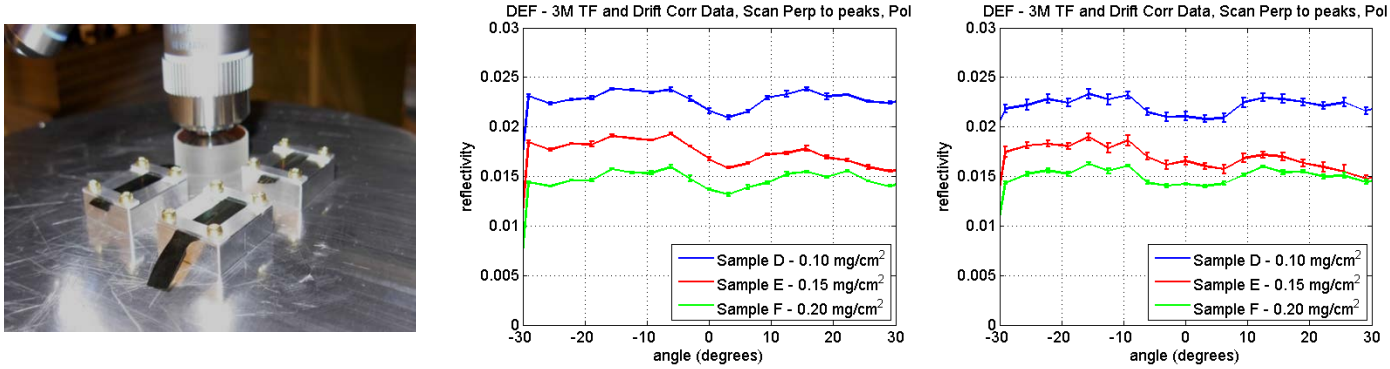

(a) (b) (c)

Figure2. *(a) An example of 3M NSTF samples mounted on a scatterfield microscope, Final reflectivity results for variable illumination angle scans using 3M NSTF with PtCoMn catalyst samples where the difference in size of the error bars for each data point represents the difference between (b) repeated measurements at the same location and (c) repeated measurements at different locations on each of the three different loading*

Figure 3 is additional data supporting sensitivity of the tool to catalyst loading; in these measurements, the wavelength of the illumination source is varied at a fixed angle. Data were collected varying different instrument parameters, illumination angle and wavelength, not only to show sensitivity to the parameter of interest, but also in an attempt **to determine the settings**

that optimize this sensitivity. These two instrument parameters, illumination angle of incidence and illumination wavelength, are only a few of the variables that have been tested and that can be tuned based on the application.

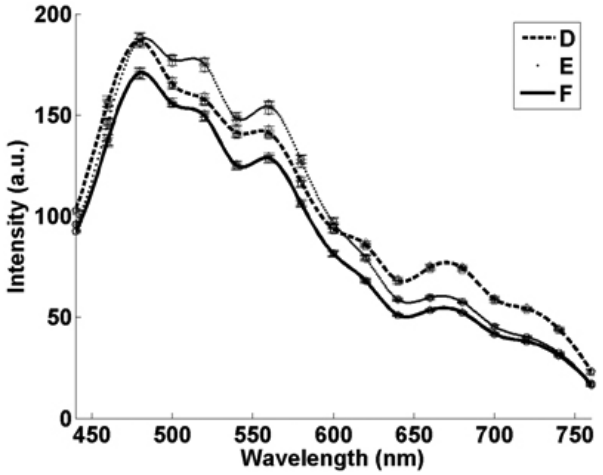

Figure 3. *Wavelength-resolved scan of 3M NSTF with PtCoMn catalyst samples*

Simulation model development was concurrent with this experimental evaluation. Figure 4 shows a 6 layer model constructed built in a commercial 3D FEM electromagnetic scattering package to represent a 3M NSTF catalyst layer. In Figures 5 (a) through 5 (c), we show the angle-resolved scans for this 6 layer model as a function of polarization at three different illumination source wavelengths: 193 nm, 450 nm, and 800 nm respectively. Each curve represents a different loading indirectly; the parameter varied in the model was the ratio of air to Pt volume. The whisker material was fixed at sixty percent. The ratios of air to Pt vary from seven to zero. For example, an air to Pt ratio of 7 is arrived at by sixty percent whisker material, thirty-five percent air, and five percent Pt (ratio = 35/5 = 7). These results were preliminary results, as at that time we did not yet have optical properties for any of the constituent materials in the catalyst layer. Air and Pt optical indices of refraction were known, but the 3M specific materials in the layer (perylene and ionomer) were unknowns requiring estimation. Obtaining accurate optical materials information for the constituent materials in the catalyst layers was a priority, one that would be addressed heavily in FY 2011 and 2012.

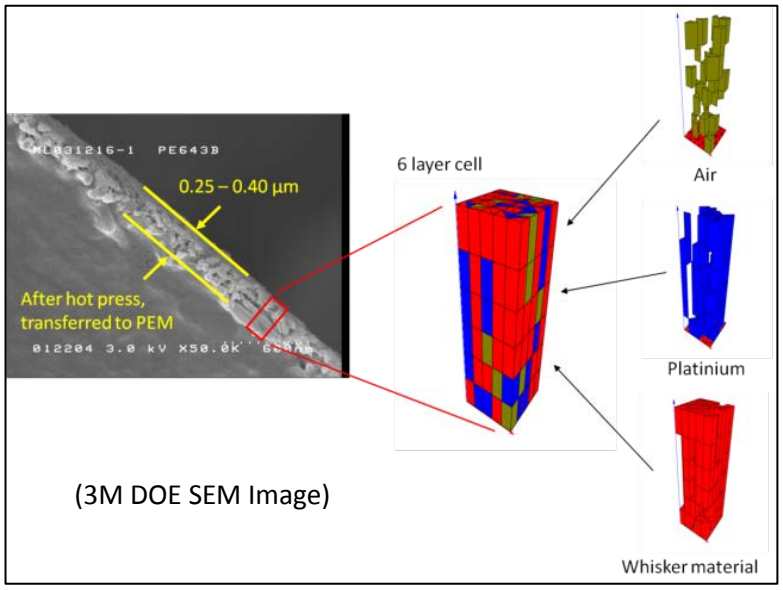

Figure 4. *6 layer preliminary simulation model for 3M NSTF CCM*

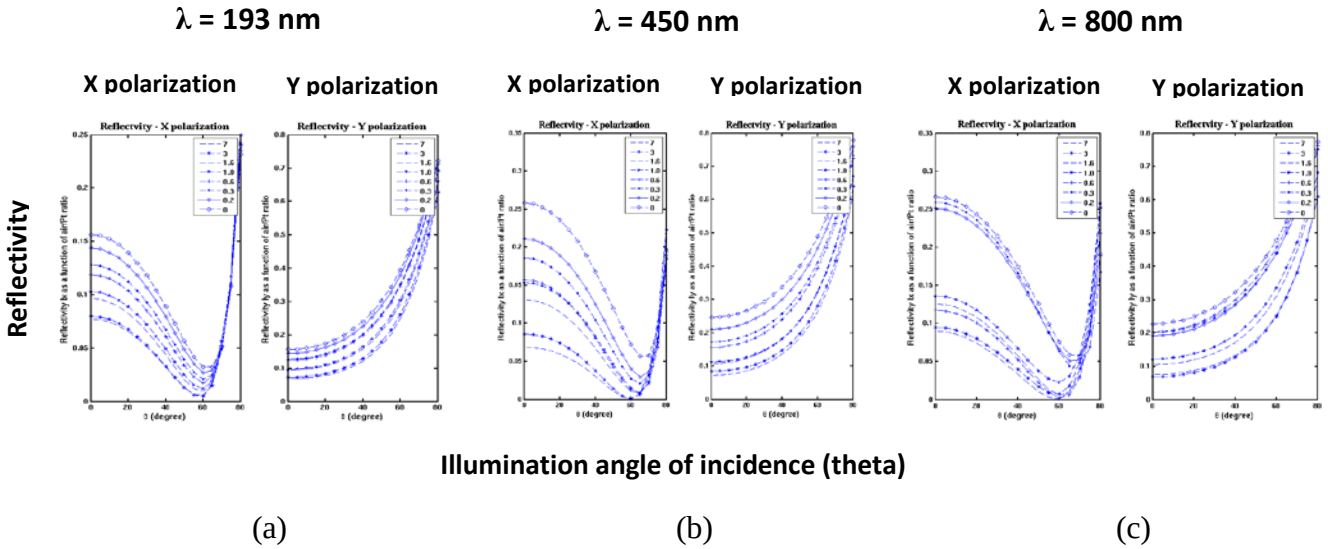

Figure 5. *Simulation result for angle-resolved scans of the 6 layer model at wavelengths a) 193nm, b) 450 nm, and c) 800 nm for different air to Pt ratios.*

Figure 6 shows our initial efforts in fuel cell defect metrology. We provided within the NIST/NREL/industry collaboration fabricated defects using dual-beam SEM/gallium FIB in support of NREL's desire to expand their membrane defect study to sub 150 um features.

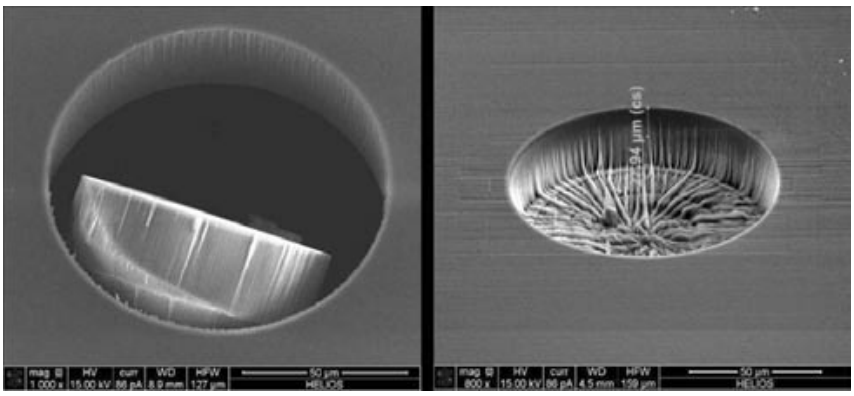

Figure 6*. 100 um diameter through hole and 100 um diameter cavity/blind hole 12 um depth membrane*

3. Fiscal Year 2011 Activities and Results

By FY 2011, this project garnered greater support from CCM manufacturers, specifically through the supply of samples by which sensitivity studies could be performed. CCM manufacturers were also helpful in establishing a benchmark catalyst loading sensitivity of 0.01 mg/cm^2, which is equivalent to that of the online XRF tool currently used. We had demonstrated that the technique was sensitive to changes in catalyst loading at the benchmark level based on a sample set of 3M Pt alloy NSTF-type CCMs reported above. However, to test the applicability of the method across a range of samples from various manufacturers, a more thorough investigation was required that demonstrated the tool's capabilities on many of the common types of CCMs being manufactured. These included 3M's NSTF CCM with pure Pt and Pt alloy catalysts and the different conventional Pt on carbon-based CCMs made by several manufacturers. These additional sensitivity results are discussed below. In addition, analytical models for each type of CCM were tested to develop greater accuracy. In the development of these models, we again relied heavily on CCM manufacturers to supply specialized samples so that we could experimentally obtain optical constants for the constituent materials which are critical to ensuring modeling accuracy.

Figure 7 shows angle-resolved reflectivity data from 3M NSTF pure Pt CCM samples with loadings of 0.05 mg/cm^2, 0.10 mg/cm^2, 0.15 mg/cm^2, and 0.20 mg/cm^2. For three of these for samples, the Pt loading sensitivity was on the order of 0.03 to 0.05 mg/cm^2. Data from a fourth sample, not shown, was highly asymmetric. Thorough investigation of the experimental and sample conditions was made to understand this asymmetry and the lower sensitivity relative to our benchmark.

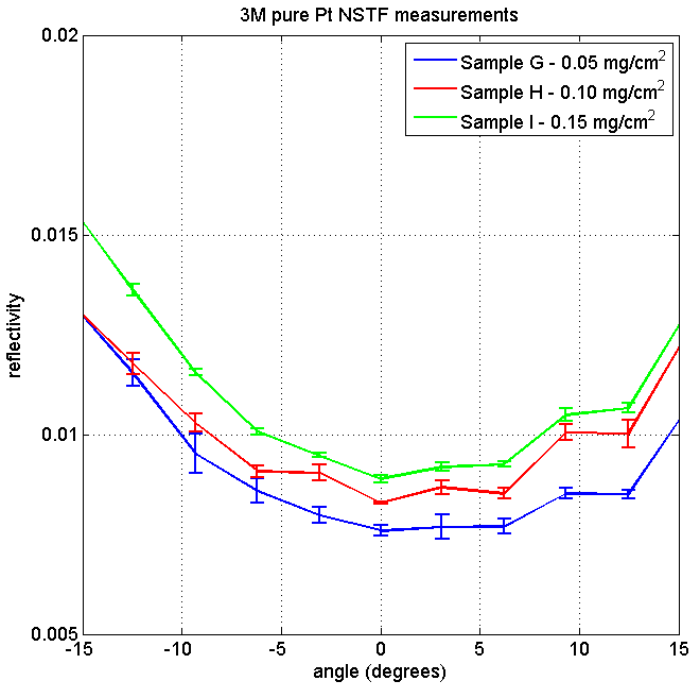

Figure 7. *3M NSTF pure Pt sample loading data. (NOTE: The separation between the curves relative to the error bars is a measure of the sensitivity)*

Two issues were apparent in data acquisition. First, the reflectivity signature versus illumination angle for the 0.20 mg/cm^2 (not shown in figure 7) appeared non-symmetrical in comparison to the other three samples. Second, visual inspection showed that this set of pure Pt samples was not as opaque as the pure Pt alloy samples. This raised questions about light transmission through the sample and the effects of back-reflected light from the from the substrate or sample holder material, as either of these factors may have contributed to the increased variability as indicated in the calculated sensitivity level, which was short of the 0.01 mg/cm^2 target.

From a reversal study, it was determined that the 0.20 mg/cm^2 sample inherently caused the asymmetry. Specifically, we performed a physical reversal of the sample. From this data seen in figure 8, the asymmetry for the suspicious sample rotated with the 180 degree reorientation of the sample (figure 8 (b), but similar measurements using one of the other well-behaved samples (figure 8 (a)) did not show an asymmetry that rotated with the sample, thus the non-symmetrical behavior of the 0.20 mg/cm^2 measurement was a sample effect. Further investigation using atomic force microscope [AFM] confirmed a larger than normal asymmetry of the unique macrostructure geometry. As this asymmetry is unimportant to the performance of the fuel cell, we were advised to find a way to make the measurement insensitive to this effect. This example is shown to demonstrate that sample-to-sample variation increases the challenge of these optical measurements.

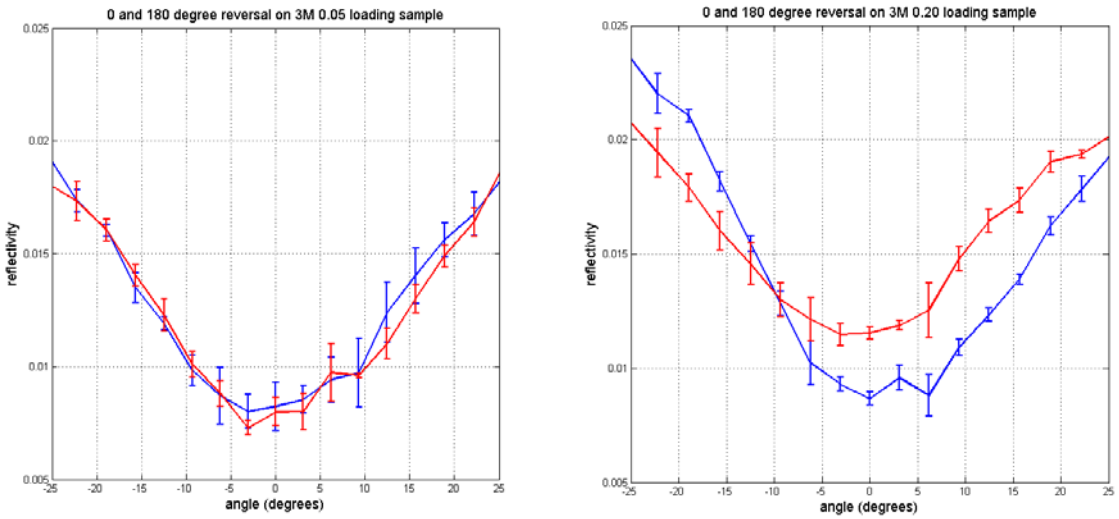

(a) (b)

Figure 8. *(a) 0 and 180 degree reversal data for the 0.05 mg/cm^2 sample, (b) 0 and 180 degree reversal data for the 0.20 mg/cm^2 sample, which displays the asymmetric behavior.*

With sensitivity demonstrated on both sets of 3M NSTF samples (pure Pt and Pt alloy), we investigated the applicability of the technique to a conventional Pt on C CCM sample set from W.L. Gore & Associates. Loadings in this set included 0.10 mg/cm^2, 0.20 mg/cm^2, 0.30 mg/cm^2, and 0.40 mg/cm^2 (A510/M710.18/C510). We performed experiments varying the angle of illumination and wavelength on two different tools. For the angle-resolved measurements, sensitivity was demonstrated on the order of 0.03 to 0.04 mg/cm^2. These data are shown in figure 9.

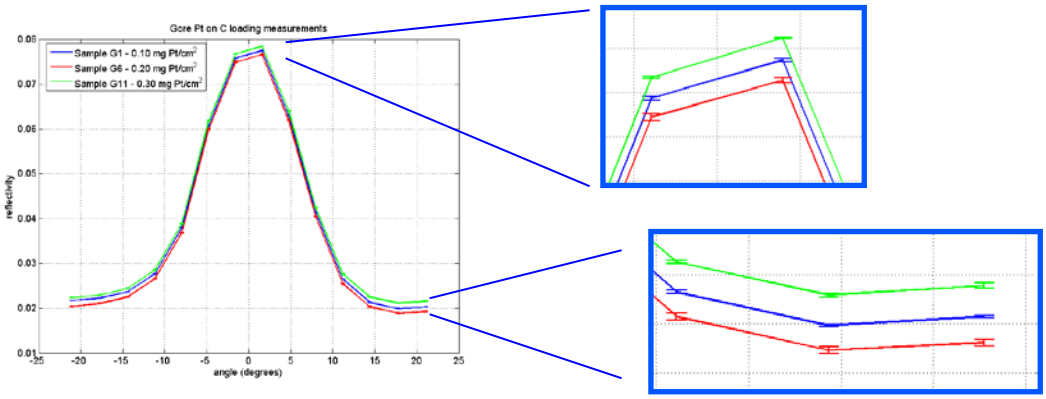

Figure 9. *Angle-resolved data on W. L. Gore Pt on C sample set*

Excellent static repeatability (multiple measurement scans at the same location) was shown for the wavelength-resolved measurements. Performing wavelength resolved measurements at five

locations on multiple days revealed variations in loading from one location to the next (on the scale of several millimeters apart), which makes the overall repeatability worse, most likely due to loading variations across these samples. This static repeatability and localized variation data are shown in figure 10.

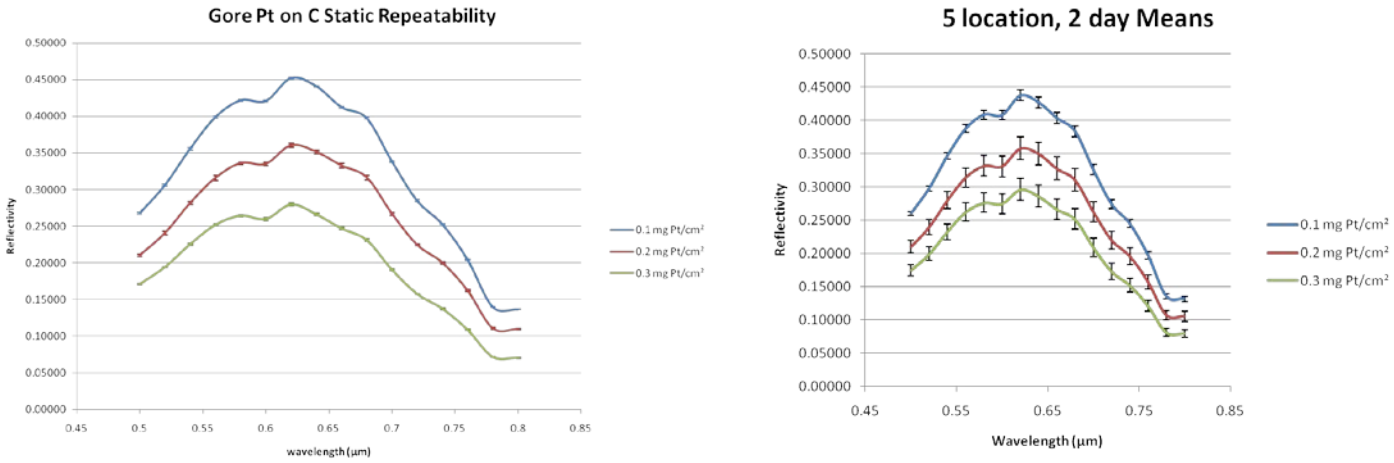

(a) (b)

Figure 10. *(a) Wavelength-resolved static repeatability data on W. L. Gore Pt on C sample set, (b) Wavelength-resolved multiple location data on W. L. Gore Pt on C sample set*

Electromagnetic scattering simulations provide a flexible and efficient method to evaluate the various parameters that have an effect on the actual physical measurement. To address possible errors within the electromagnetic models, the strengths and weaknesses of the models as applied to fuel cell structures were thoroughly vetted. The various model-specific input parameters affecting convergence were studied. We ran simulation convergence tests on three different models. On our 2D rigorous couple-wave analysis (RCWA) model, we investigated the number of orders. With our 3D finite-difference time-domain (FDTD) and finite element method (FEM) models, we investigated domain size, grid size, and grain size.

However, accurate simulation requires accurate inputs to the models, such as target dimensions, layer thicknesses, surface roughness, materials optical properties (complex index of refraction), etc. To address the lack of optical property data on CCM constituent materials, NIST procured and took delivery of a spectroscopic ellipsometer. This instrument was able to be used in two modes. It was used in a scatterometer mode to acquire angle- and wavelength-resolved data on fuel cell samples. It was also used in an ellipsometer mode, which enabled measurements of material optical properties (*n & k*) that were critical to the modeling effort. Using this new ellipsometer, NIST began ellipsometric measurements of special constituent material samples provided by our industry collaborators. We measured bare PEM samples provided by 3M and

W. L. Gore. Given the surface roughness of these layers an effective medium approximation (EMA) was attempted to measure the n and k of these materials.

An EMA allows for the optical properties of composite materials to be approximated by a uniform effective medium. A schematic of an EMA is shown in figure 11(a). It is an acceptable approximation when the length scales associated with the local variations in permittivity are small compared to the wavelength of light in the media. We used a generalized anisotropic Bruggeman EMA to model the effective medium layers. This model can be derived from the generalized form of Maxwell Garnett's EMA (figure 11(b)) using the expression for the polarizability of ellipsoidal particles where ε_{eff} is the effective medium permittivity, ε_0 is the permittivity of the host medium, and ε_i and f_i are the permittivities and volume fractions of each of the M materials.

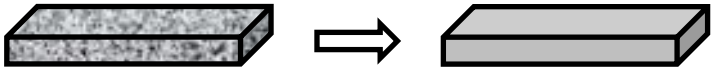

$$\frac{\varepsilon_{\text{eff}} - \varepsilon_0}{\varepsilon_0 + L(\varepsilon_{\text{eff}} - \varepsilon_0)} = \sum_{i=1}^{M} f_i \frac{\varepsilon_i - \varepsilon_0}{\varepsilon_0 + L(\varepsilon_i - \varepsilon_0)},$$

(a) (b)

Figure 11*. (a) Schematic of an EMA (b) Generalized form of Maxwell Garnett's EMA*

For the bare PEM samples, the surface roughness exceeded the criteria for applying the EMA. However, we successfully applied an EMA approach to measure a Gore CCM as a whole to determine the average *n & k* of the entire CCM. This is not the same as being able to measure the optical properties of each constituent material in the CCM and run simulations. Using this *n & k*, we tested our model to see if it generated reflectivity data that was on the same scale and trended the same as the wavelength-resolved experimental data. The data in figure 12 (a) is an angle-resolved experimental data set taken at a wavelength of 620 nm for the Gore CCM. In figure 12 (b), this experimental data is shown overlaid on the theoretical data. This is a promising result showing good qualitative agreement trending correctly as a function of illumination angle of incidence.

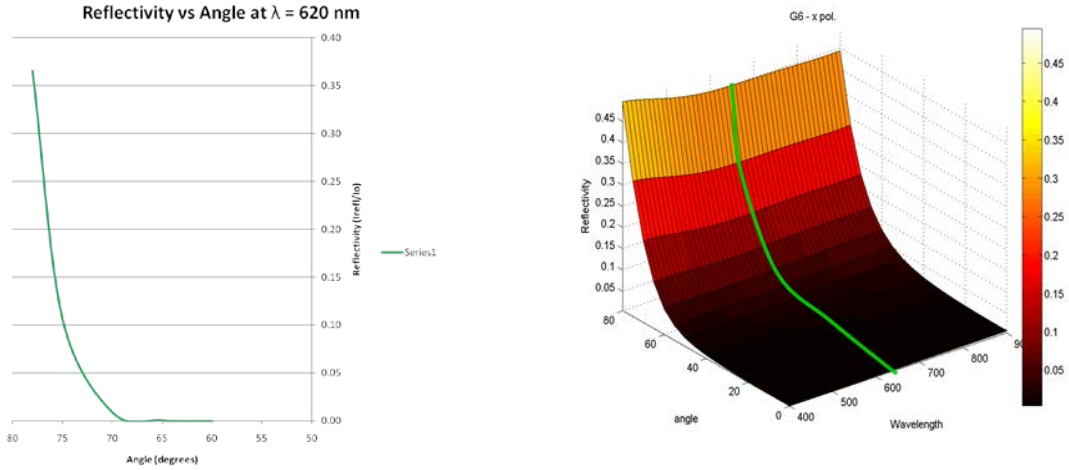

(a) (b)

Figure 12*. (a) Experimental EMA W. L. Gore CCM data, (b) W. L. Gore experimental vs theoretical data*

4. Fiscal Year 2012 Activities and Results

Further pursuing model development and improvement for accurate CCM electromagnetic scattering models, we collaborated with 3M to generate samples that would allow us to measure the optical properties of CCM constituent materials. The first sample set of annealed perylene coated Si wafers yielded a surface texture that made spectroscopic ellipsometry (SE) measurements extremely difficult; a second, unannealed sample set yielded a smoother surface and useful SE measurements for extracting an *n & k* for perylene PR149. Pictures and SEM images of these samples are shown in figure 13. While these optical constants are for bulk perylene and do not exactly match the optical properties of the crystal structure of the annealed perylene whiskers, these values provided an invaluable *n & k* starting point for perylene PR149 in the modeling. The *n & k* data for bulk perylene PR149 are shown in figure 14.

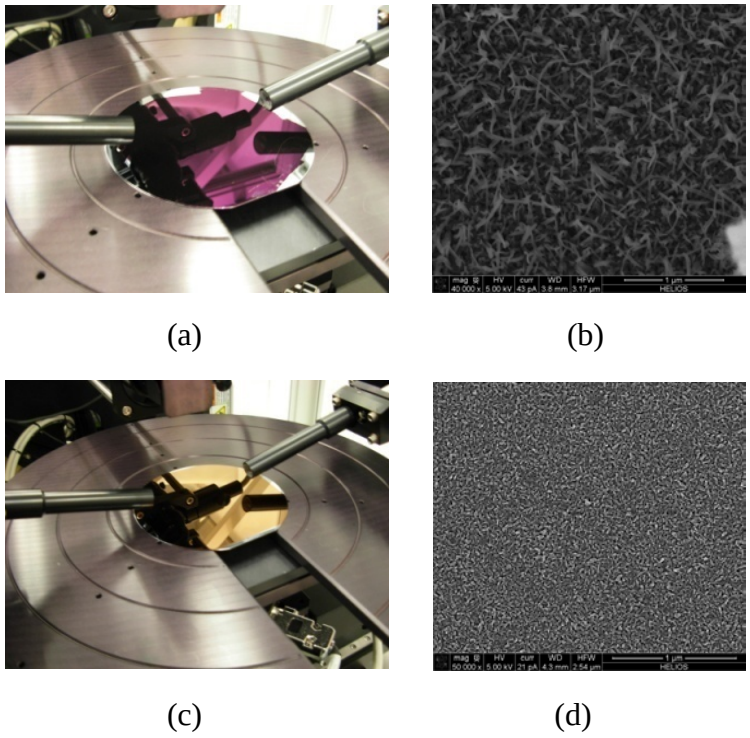

(a) (b)

(c) (d)

Figure 13*. (a) picture of 3M perylene PR149 annealed sample, (b) SEM image of 3M perylene PR149 annealed sample, (c) picture of 3M perylene PR149 unannealed sample, (d) SEM image of 3M perylene PR149 unannealed sample*

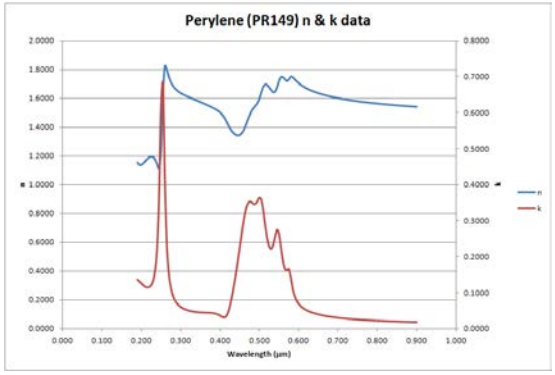

Figure 14*. Perylene PR149 n & k data as function of wavelength*

With these new *n & k* data, we performed two modeling tests. The first was a two-dimensional model-to-model comparison. One benefit to using the effective medium approximation is that the modeling can be performed more quickly using a 2D model rather than a fuller 3D

implementation. We compared a 2D RCWA model to a 2D FEM model. These results are shown in figure 15. Achieving qualitative agreement between our 2D models builds confidence in results that are obtained from either model in the future. The simulation was of a 3M NSTF CCM with a 0.250 μm effective medium approximation (EMA) catalyst coating on a top of a 20 μm finite ionomer substrate. This set of simulations was run as angle-resolved scans. Both polarizations trended the same direction with similar reflectivity values as a function of angle. This represented an incremental step forward, showing that our 2D models had qualitative agreement with new optical property data that is closer to the actual physical sample. The increased oscillations in the RCWA output (figure 15 (b)) were likely a result of the thin-film interferometric effect from the bilayer.

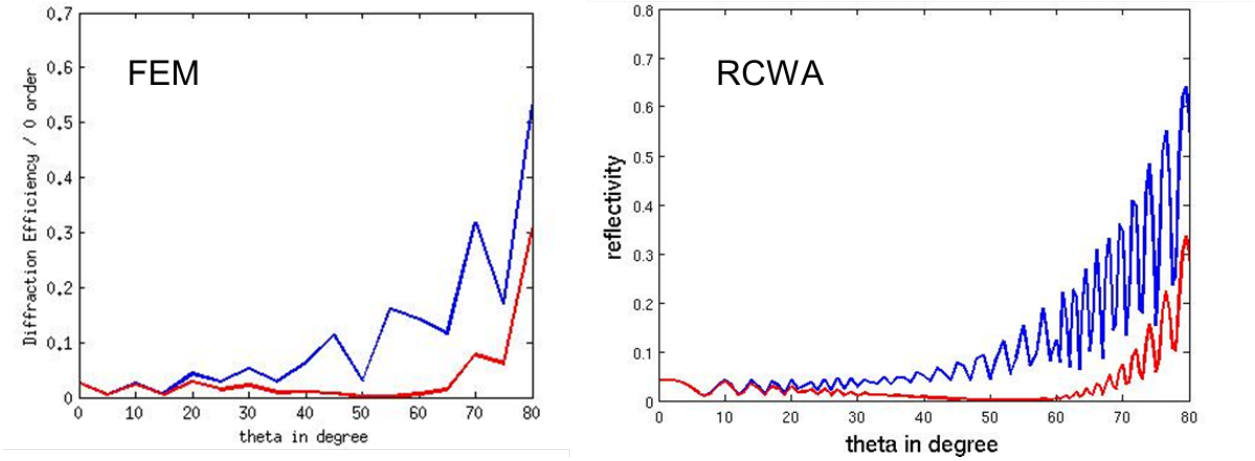

(a) (b)

Figure 15*. (a) 2D FEM model results for a 3M NSTF CCM, (b) 2D RCWA model results for a 3M NSTF CCM*

The second test was a theory to experiment comparison. The wavelength-resolved experimental data were acquired on a 3M 0.1 mg /cm^2 NSTF CCM sample using our commercial ellipsometer in the scatterometer mode. For the simulation, a wavelength scan at a 70 degree illumination angle of incidence was performed on a 2D model of this triangular structure built in the FEM code. The actual meshed model is seen in figure 16. There is promising qualitative agreement with both the theory and experiment having similar reflectivities and trending the same as a function of wavelength. The simulation data is shown in figure 17 (a) and the experimental data in figure 17(b). Other angles of incidence give very different values of reflectivity with 65 degrees yielding an order of magnitude less reflectivity and 75 degrees yielding 5 times more reflectivity. The blue simulation and green experimental curves are s-polarization data and the red simulation and pink experimental curves are p-polarization data.

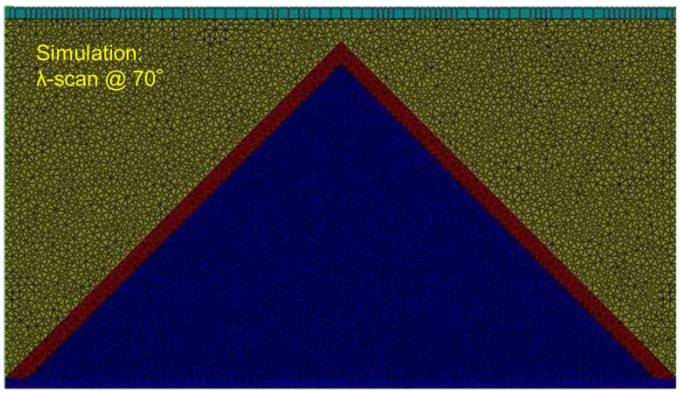

Figure 16. *2D FEM model of 3M NSTF triangular CCM structure*

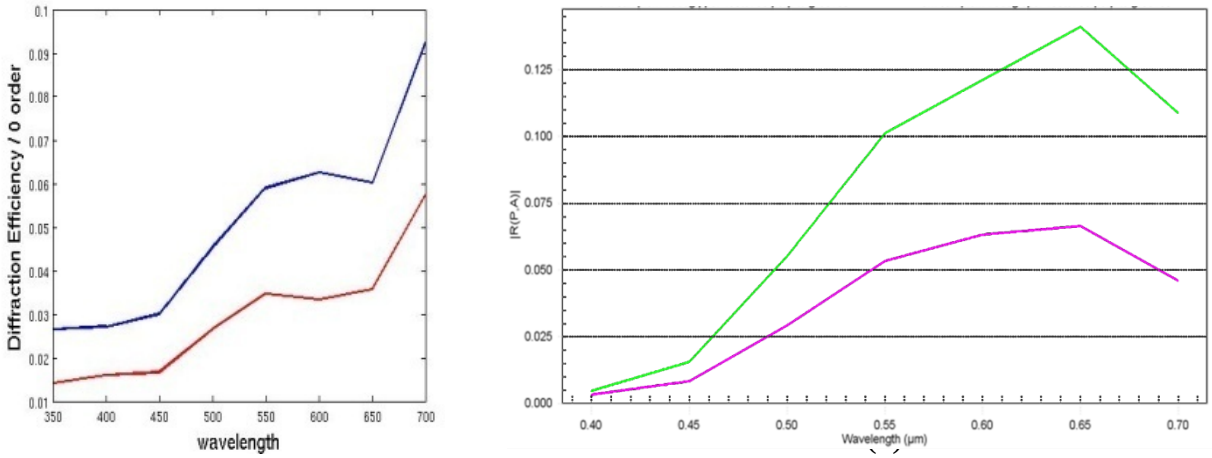

Figure 17. *(a) 2D FEM simulation data of a 0.10 mg/cm^2 3M NSTF CCM, (b) Experimental data on a 0.10 mg/cm^2 3M NSTF CCM*

The modeling of CCMs presents a challenge for several different reasons, one of them being the randomness and magnitude of the surface roughness. To study this problem, we built a structure in the three-dimensional FEM model consisting of pillars with varying heights and cross-sections. This was designed to represent both 1) the surface texture created from hot pressed Pt-coated perylene whiskers in the 3M NSTF CCM as well as 2) the surface texture from 50 nm to 100 nm carbon grains in a carbon-Pt nanoparticle CCM. Preliminary simulations were run to understand the effects of roughness on reflectivity as a function of grain size and illumination angle of incidence. This pillar modeling structure is shown in Figure 18. The model consists of air (in gold) between pillars atop an EMA catalyst layer (in purple), which contains Pt, perylene, air, and ionomer. There are not yet definitive results from this study given the computational requirements of 3D FEM simulations.

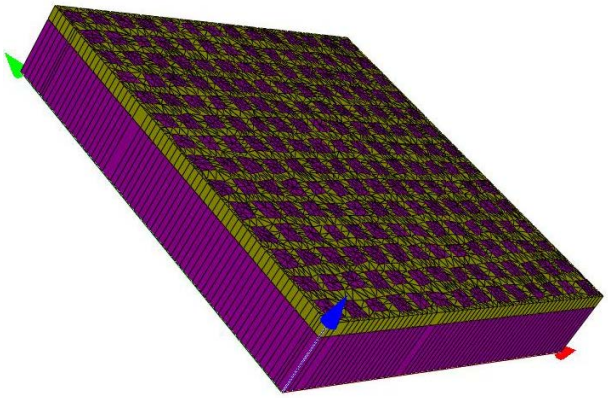

Figure 18. *FEM-based roughness modeling structure*

In addition, some initial simulation demonstrations were performed. The first was a pinhole defect simulation. We ran simulations of a 300 nm and a 500 nm pinhole defect as a function of wavelength, polarization, and illumination angle of incidence. Sensitivity to the change in diameter of the pinhole was observed. The second simulation was a demonstration of the capability of OSM to perform simultaneous independent single-sided measurements of a double-coated CCM. In this simulation, we compared results from: 1) a 20-μm PEM layer coated with 0.06 mg/cm^2 on one side and nothing on the other side to 2) a 20-μm PEM layer coated with 0.06 mg/cm^2 on one side and 0.03 mg/cm^2 on the other. We were able to observe that an optimal set of simulation measurement parameters (wavelength, polarization, illumination angle of incidence, etc.) existed that minimized the influence of the 0.03 mg/cm^2 side on the measurement of the 0.06 mg/cm^2 side. **This observation demonstrated the flexibility to tune an optical system to a given measurement task**.

With these data, we assessed the strengths and weaknesses of making fuel cell loading measurements using 1) OSM and 2) traditional scatterometer (using our ellipsometer in a scatterometer mode). Traditionally, OSM is realized using a high-magnification imaging tool with small spot size on the order of tens to hundreds of micrometers. It is an open architecture design which permitted us to completely customize and engineer the illumination and collection paths for fuel cell measurements. With this flexibility, we were able to measure the reflectivity of various CCM samples as functions of polarization, wavelength, and illumination angle of incidence. The experimental fuel cell data we generated, for example, were images acquired as a function of the parameters mentioned above and processed to determine reflectivity. The determined reflectivity is proportional to Pt loading.

However, there remained open issues with using OSM in a high-magnification instrument to perform Pt loading measurements. First, vertical motion of the sample on a webline could introduce complications due to a change in focus. Second, the low reflectivity nature of the

CCM samples caused a low signal-to-noise ratio in our measurements. Third, wavelength scanning on our Scatterfield microscope is not ideal (alignment of optical components is dependent on illumination wavelength). Although a high-magnification instrument is sensitive to local defects and localized Pt loading variations, in the final analysis a non-imaging solution is strongly suggested for these Pt loading measurements, similar to a scatterometer.

With the purchase of the commercial ellipsometer in 2011, we addressed some of the issues identified above. The ellipsometer was purchased primarily as a tool for measuring optical property determination of fuel cell materials. It also had the added benefit of using it in a scatterometer mode allowing us to make reflectivity measurements as a function of illumination angle of incidence and wavelength. The design of the ellipsometer caters to the semi-conductor industry, utilizing a small spot diameter ranging from a few millimeters to a few hundred micrometers, in order to enable process control of line width and positioning using the smallest possible targets. We were able to successfully measure the optical properties of some CCM constituent materials (perylene). The instrument worked very well in measuring Pt loading on Gore CCM samples as a function of wavelength. Although this instrument addressed some of the issues, a few key ones remained. Because of its small spot size, the issue of vertical motion of the sample still remained as well as unwanted sensitivity to local defects and sample positioning. There also remained the need to make dynamic measurements of samples at webline speeds.

What was required was a scatterometry-based tool in which the illumination was optimized for the measurement of Pt loading – the application of OSM on a scatterometer. With these issues remaining, we began the design of a new dedicated fuel cell research instrument. The intent of pursuing the design and fabrication of a new measurement instrument is that it would be the best candidate for becoming an in situ process control solution for making loading measurements and performing defect detection. We investigated scatterometric-based approaches without high magnification. We evaluated four different configurations taking into consideration cost, manufacturability, ease-of-use, failure modes, functionality, and ability to address our open issues. The four different configurations are show in figure 19 and are as follows: 1) wide illumination beam, 2) scanned illumination beam, 3) single source and single detector, and 4) multiple source and multiple detector.

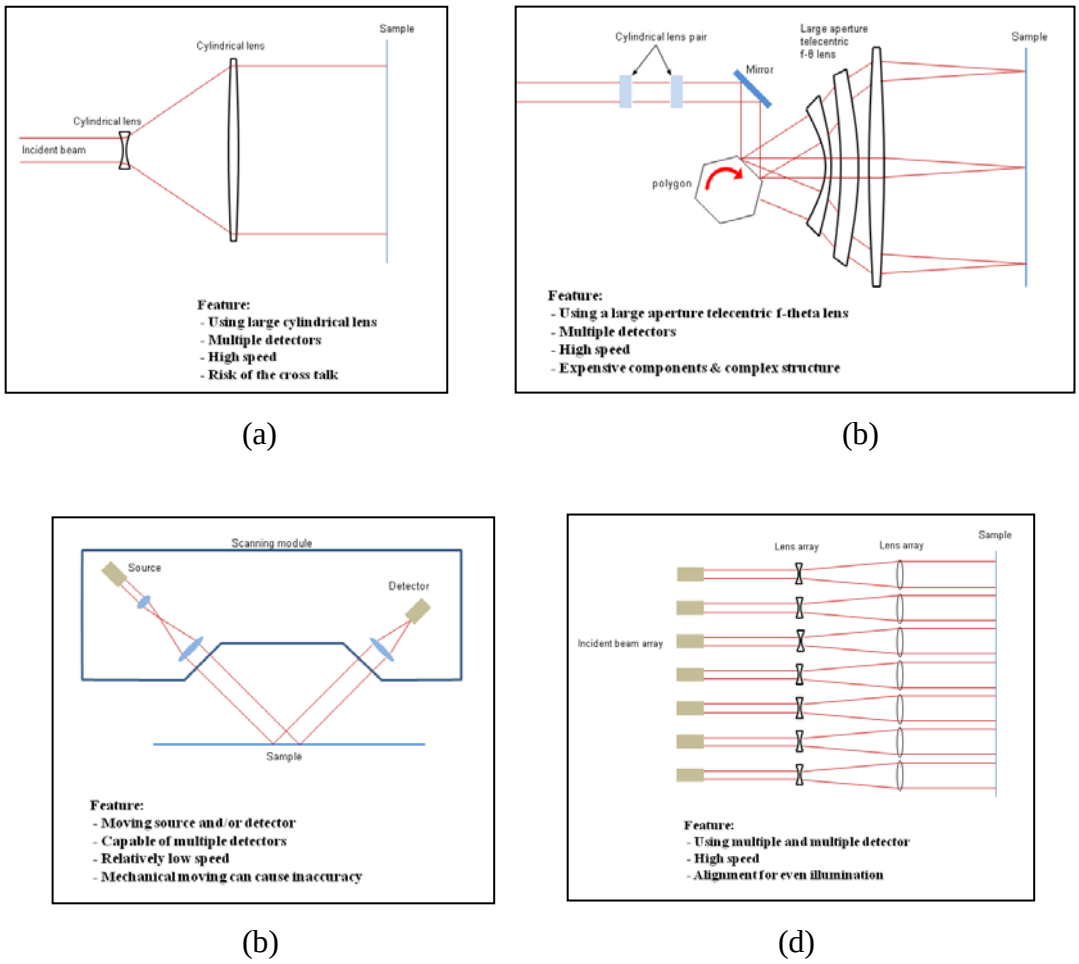

Figure 19. *Scatterometry based fuel cell instrument design configurations (a) Wide illumination beam, (b) Scanned illumination beam, (c) Single source and single detector, (d) Multiple source and multiple detector*

We decided on the multiple source and multiple detector configuration. We called this new instrument the Large Aperture Projection Scatterometer (LAPS). The LAPS had a built-in adjustable large spot size (ranging from two to twelve millimeters) in addition to a stage system to permit dynamic loading measurements. After settling on the configuration, we performed a complete optical design for the multiple source and multiple detector approach. The optical layout for this configuration is shown in figure 20.

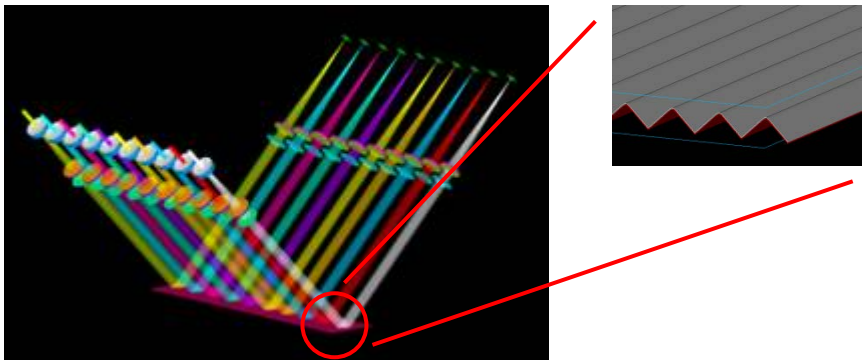

Figure 20. *Multiple source, multiple detector LAPS configuration optical layout*

5. Fiscal Year 2013 Activities and Results

In FY2013, efforts focused on designing, developing, and building the LAPS instrument. To repeat, the motivations for building this tool, compared to the performance of OSM and our commercial ellipsometer include: large spot size for data averaging, better signal to noise (than OSM), and the ability to make loading measurements at benchmark webline speeds. Activities leading to the finished LAPS instrument included: 1) completing mechanical design, 2) procuring instrumentation, 3) fabricating required parts, 4) developing optical and mechanical alignment procedures, 5) aligning and testing the tool, 6) writing LabVIEW motion control and data acquisition routines, 7) making initial characterization measurements of known materials to validate proper function.

With this instrument, dynamic measurements (simulating webline) of catalyst coated samples were successfully taken. With the angular control of the LAPS, it also provided additional capability to study the diffraction patterns generated by 3M NSTF samples. The LAPS currently exists as a single arm of the proposed multiple-source multiple-detector measurement instrument. The vision is to bring the technology to the point of a commercially available instrument for catalyst coating and defect inspection. As a commercially available instrument, it would be a scalable solution where the end-user could add/subtract source/detector pairs to meet the process control requirements of their webline. A schematic and picture of the instrument is shown in figures 21 (a) and 21 (b) respectively. The instrument consists of an illumination and collection arm. The illumination arm contains the green diode laser source and beam expansion optics. The collection arm contains the detector and focusing optics for placing the reflected light onto the detector. The 1D stage used at this point allowed for making initial loading measurements at speeds up to 4 ft/min. While recognizing this was short of the benchmark 30 ft/min, this initial stage was useful in developing the data acquisition as a faster stage was being obtained.

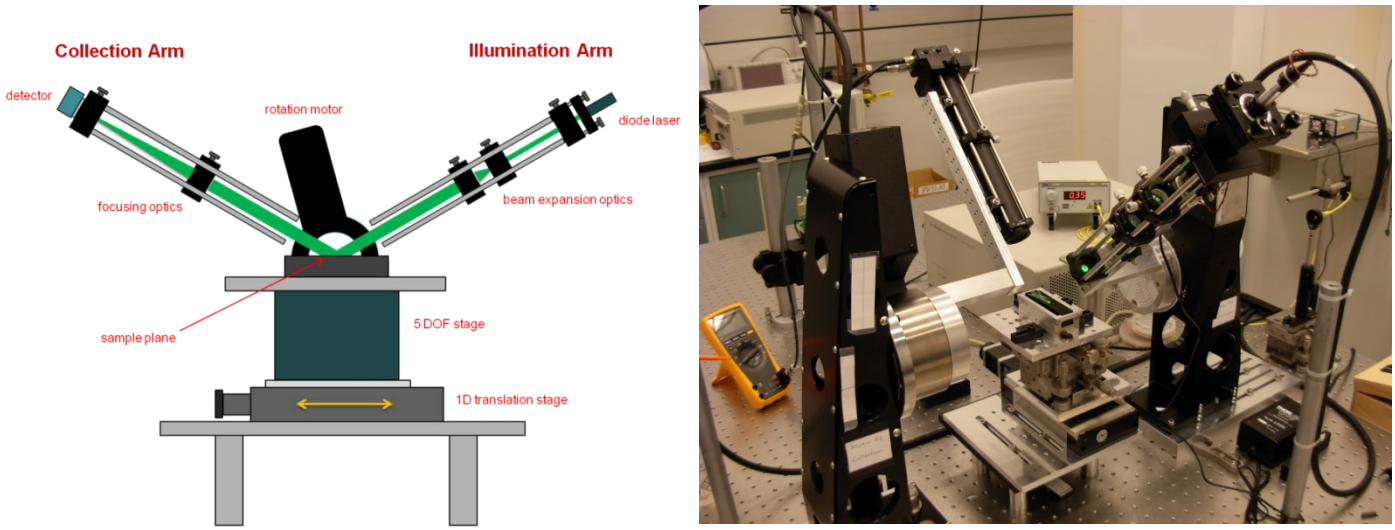

Figure 21. *(a) Schematic of the LAPS instrument, (b) Picture of completed LAPS instrument*

Preliminary dynamic loading measurements were made on Gore Pt on Carbon CCM samples (A510/M710.18/C510). Measurements were made up to a speed of 4 ft/min. Here the illumination and collection arm angles were set equal and fixed as the samples were scanned underneath at different speeds. Four sample loadings, 0.10 mg/cm^2, 0.20 mg/cm^2, 0.30 mg/cm^2, and 0.40 mg/cm^2, were measured. At these slower speeds, there is good sensitivity and repeatability. There did not appear to be any dependence on velocity. A graph of the the measured intensity for each of the four loadings as a function of velocity is seen in figure 22.

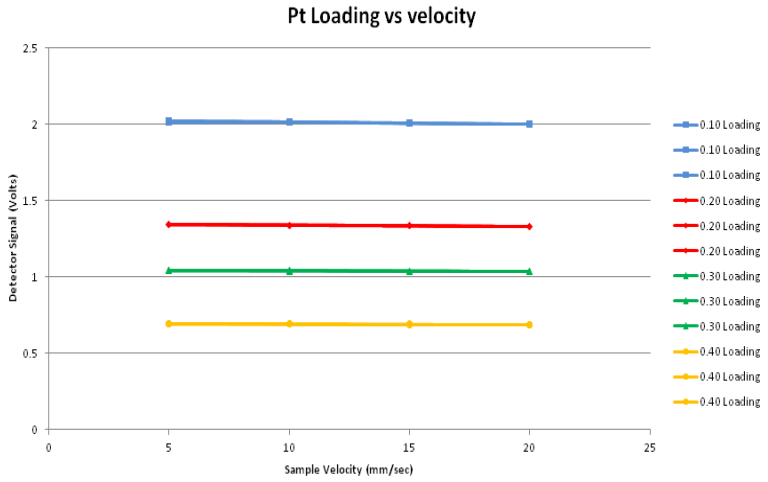

Figure 22. *Dynamic loading measurements of Gore Pt on Carbon CCM samples (NOTE: graph shows the maimum velocity of 20 mm/sec, which is about 4 ft/min)*

An added benefit of the LAP S instrument was good angular control of the illumination and collection arms. This permitted us to begin to analyze the diffraction patterns generated by the 3M NSTF CCM samples. When these samples are illuminated perpendicular to the triangular

substrate on which the catalyst layer exists, a diffraction pattern is produced. The 3M NSTF sample is essentially a grating. The diffraction is shown figure 23. A close up shown in figure 23 (b) reveals the orders of the pattern.

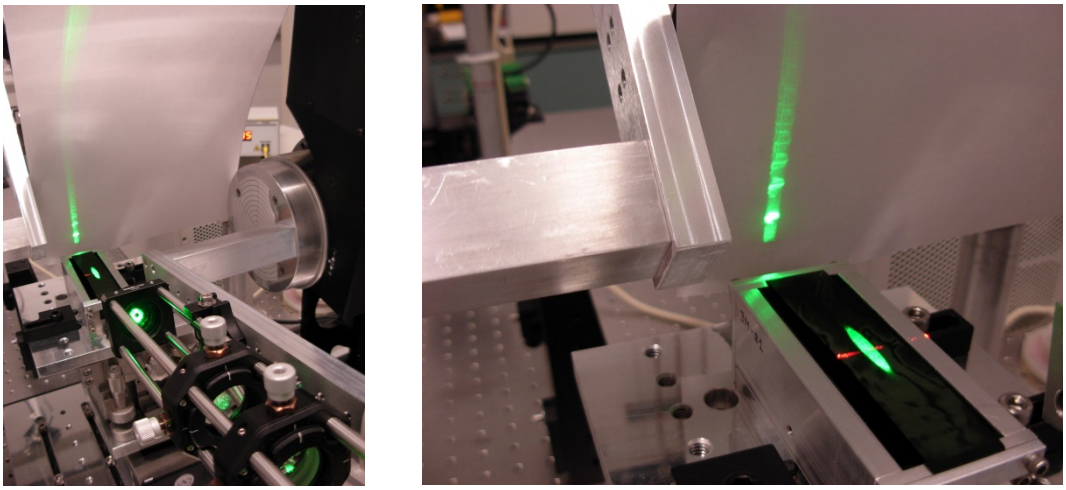

(a) (b)

Figure 23*. (a) 3M NSTF CCM diffraction pattern generated on LAPS instrument, (b) close up of the diffraction pattern*

We successfully measured the diffraction pattern as a function of Pt loading on the 3M NSTF PtCoMn alloy samples. The diffraction pattern presented a new measurement challenge that requires further study. The amplitudes of the different peaks contain key information about the materials and surface characteristics. In this measurement, the illumination arm is held at 80 degrees and the collection arm is scanned from 80 to 30 degrees. Studying this pattern to determine the best method to measure it effectively remains a priority. Certain peaks showed excellent sensitivity to Pt loading. The LAPS is shown in a collection arm scan mode in figure 24 (a). In figure 24 (b), the diffraction pattern scan results of three different loadings (0.10 mg/cm^2, 0.20 mg/cm^2, and 0.30 mg/cm^2) are shown graphed on a log scale.

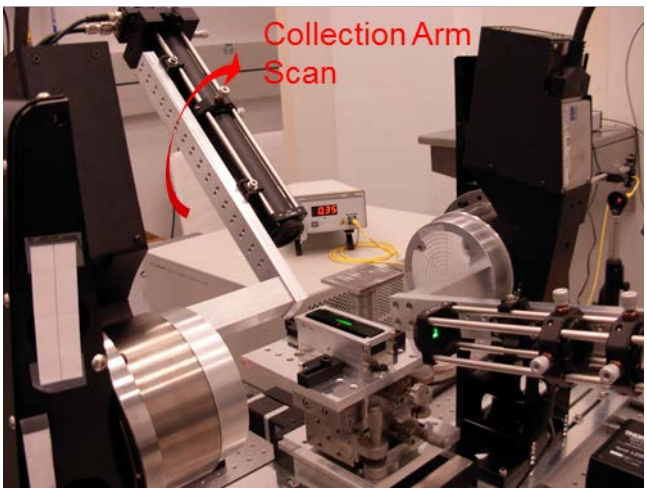

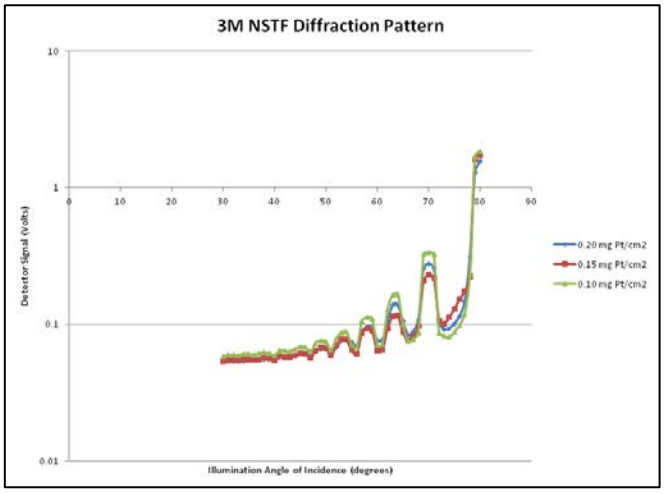

(a) (b)

Figure 24*. (a) LAPS instrument in a collection arm scan mode, (b) 3M NSTF PtCoMn alloy CCM diffraction pattern results graphed on log scale*

Demonstrating catalyst loading measurements at typical webline speeds was a priority. Figure 25 shows the final configuration of the LAPS instrument with a new high-end 1D linear motor stage from Newport Corporation with 6.3 inches of travel and capable of moving at a maximum speed of 59 ft/min. As FY2013 concluded, we fabricated parts, wrote LabVIEW motion control and data acquisition code, and realigned the tool with new parts installed. This instrument is ready to acquire data at benchmark webline speeds.

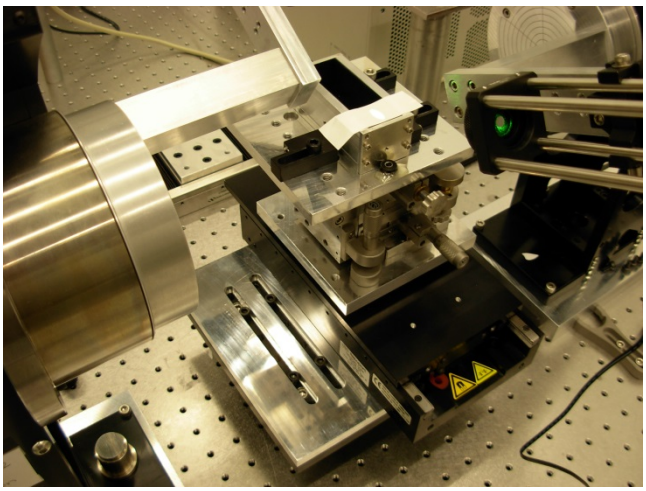

Figure 25*. LAPS instrument with new linear stage installed*

6. Conclusions

In evaluating the suitability of OSM as an in situ process control tool for catalyst coatings over the duration of this project, we made substantial advances, both experimentally and theoretically,

in furthering state-of-the-art in fuel cell manufacturing metrology. Experimentally, using OSM, we successfully demonstrated Pt loading measurement sensitivities at the level of competing technologies with our best sensitivity values on the order of 0.01 mg/cm^2. To further understand the underlying measurement science and develop the necessary rigor, we designed and built a custom optical metrology tool called the Large Aperture Projection Scatterometer (LAPS) specifically for making fuel cell loading and defect detection measurements. The tool is now operational. We acquired initial LAPS loading data on Gore (as function of velocity) and 3M (diffraction pattern) samples. This new tool will be used to measure large format samples at typical webline speeds of 30 ft/min and greater. As simulation is also a vital part of enabling rigor in the OSM approach, we improved existing and developed new modeling capabilities tailored to simulating the optical response of catalyst coatings. This effort involved measuring optical properties of catalyst coating constituent materials, designing new model constructs, and testing 2D and 3D catalyst coating models. We demonstrated qualitative theory-to-experiment agreement for catalyst coatings.

7. Future Work

Optics holds the highest potential for cost-effective, non-destructive, and high throughput quantitative in situ process control solutions for fuel cell catalyst coating manufacturing. Harnessing these inherent attributes of optical technologies requires a complete understanding of the scattering of light by these complex materials, which is achieved through proper combination of accurate simulations and optimized experiments. The optical scatterfield metrology approach joins highly sensitive measurements with accurate modeling to enable quantitative process control. The full realization of optics-based catalyst coating metrology will involve the maturation of the LAPS technique coupled with a rigorous simulation basis.

7.1 Theoretical and modeling work

The most pressing challenge to achieving quantitative fuel cell manufacturing metrology is to develop the simulation infrastructure to enable the underlying rigor with acceptable uncertainties and sensitivities. Although we have demonstrated initial theory to experiment data fits, different manufacturers, using different methods and materials for their membranes, requires adaptability of the methodology. Hence, a flexible model is necessary that allows different geometrical parameters and normalization procedures. Once a robust modeling and fitting algorithm has been established, the method will be more broadly applicable to different membrane types. To achieve this level of quantitative fuel cell manufacturing metrology, there remains significant work in properly measuring the optical properties of the CCM constituent materials. In addition, the catalyst coating models require complex enhancements in order to more closely replicate the actual physical samples (i.e., surface roughness, material ratios, defects, etc.). For this methodology to become a robust effective metrology solution, we need to be able to accurately model the samples to generate quantitative simulation data. It should be noted that the same modeling and data fitting procedures have been broadly applied to three dimensional nanometer

structures for the semiconductor manufacturing industry and achieved sub-nanometer uncertainties and resolution.

7.2 Experimental and instrumentation work

Equally challenging is bringing the capabilities of the LAPS for multiple-beam, dual-side metrology out of the laboratory and into a manufacturing environment. This transition will require both a more robust design as well as a more thorough understanding of the scattered signal. The current LAPS research prototype instrument is ready to make loading measurements of larger format samples at webline speeds of 30 ft/min or greater. To obtain the best possible measurement, comprehensive characterization and calibration of the LAPS tool is required. Scaling this hardware architecture to increasing throughput will require additional design work and research. Further study is necessary to understand the full potential of the diffraction and scattering of the periodic 3M NSTF samples and to optimize the instrumentation for loading and defect determination. Continued investigation is vital to understand the applicability of OSM and LAPS to performing fuel cell catalyst coating defect inspection. Additional industry input is needed to determine the types, sizes and distributions of defects that cause real performance losses in fuel cells. A partnership with a leading optical metrology toolmaker should be pursued to assist in developing a marketable OSM and/or LAPS process control measurement system.

8. References

R.M. Silver, B.M. Barnes, R. Attota, J. Jun, M. Stocker, E. Marx, and H. Patrick, “Scatterfield Microscopy for Extended Limits of Image-Based Optical Metrology,” Applied Optics, Vol. 46, No. 20 (2004).

9. Products developed under the award and technology transfer activities

Presentations

Stocker, Stanfield, and Muralikrishnan, Metrology for Fuel Cell Manufacturing, Presentation to the FreedomCar Tech Team, March 16, 2011

Stocker M, Goasmat F, Qin J, Silver R, Barnes B, Stanfield E. Optical Scatterfield Microscopy for PEMFC Catalyst Coating Manufacturing Process Control. Poster session presented at: Fuel Cell Seminar and Exposition 2011; 2011 Oct 31 – Nov 3; Orlando, FL.

DISCLAIMER

Appendix A

Static Contact Angle Measurements on AXF-5QCF Flow Field

Report Number: **NIST-2012-06-MichiganTech**

Date of Report: June 28, 2012

Contributors: J. S. Allen
V. Konduru

Contact: **Jeffrey S. Allen**
Mechanical Engineering - Engineering Mechanics
Michigan Technological University
815 R. L. Smith Building
1400 Townsend Drive
Houghton, Michigan 49931
(906) 487-2349
jstallen@mtu.edu

1 Cleaning Procedure

Five sets of contact angle data were collected on the flow field plate. The fluid used was distilled water. Before each data set, the plate was cleaned. For the first data set, the plate was cleaned using methanol. It was then rinsed under running distilled water. This procedure was repeated and then the plate was dried using nitrogen. For the second data set, the plate was cleaned using isopropanol. It was then rinsed under running distilled water. The plate was then cleaned using methanol and distilled water and then dried with nitrogen. For the third and all the subsequent data sets, the plate was cleaned using isopropanol and distilled water twice, dried with nitrogen and then placed in a vacuum desiccator for 30-40 minutes.

2 Test Method

The drops were deposited on the plate using a screw syringe and the image of the drop was captured by a long-distance microscope connected to a CCD camera. From the drop image, the drop profile is obtained. This drop profile is then fit to the theoretical Laplace curves that are obtained from numerical integration of the Laplace-Young equation, which relates the pressure difference that exists across an interface due to interfacial tension and hydrostatic pressure. The Laplace curve that results in minimum error with respect to the image is the theoretical drop profile from which the contact angle is obtained.

2.1 Test Locations

Drops were deposited on the channel side of the plate along the edge marked 'B-1' with an adjacent arrow marked on the surface. Approximately 10 drops were deposited during each data set and an attempt was made to place the drops in the same location as the first data set. These locations are highlighted with green circles in Figure 1. After the fourth cleaning, drops were also deposited on an orthogonal edge (edge 2, yellow circles in Figure 1) of the plate as well as on the channel lands of the flow field (red circles in Figure 1 and Figure 2). For the channel land tests, if a drop touched the edge of the land the data was rejected during analysis as the measurement would not be accurate due to contact line pinning. Only the drops that were entirely within the channel boundary were considered for analysis. For the fifth data set, drops were deposited on the backside of the plate. An attempt was made to place the drops directly opposite the locations tested during the first four data sets. After the sixth cleaning, drops were deposited on the corners of the plate on the channel side (blue circles labeled 'A - D' in Figure 1).

3 Results

The test results are provided in Table 1. The drop diameter in mm, drop volume in μm, and static contact angle in degrees are provided. As it was not possible to precisely place drops in the same

location as the first data set, the contact angle that was observed varies slightly from data set to data set.

In theory, a drop placed on a smooth surface is expected to be axisymmetric. However due to the rough surface of the plate, it becomes inherently difficult to obtain axisymmetric drops. To minimize the error that accompanies the asymmetry of the drops, the drops were visually inspected from the top and only the drops that appeared fairly symmetric to the naked eye were selected for contact angle measurements. To check the uncertainty in the results due to this asymmetry, orthogonal views of the drops were captured for the drops placed on the corners of the plate ('A - D' in Figure 1). The difference in contact angle obtained for the two different views is about ± 2-3°.

3.1 Channel Side

The range of contact angle observed on the channel side of the plate is 75° - 90°Åfter the fourth cleaning, the difference in the minimum and the maximum contact angles at any location was found to be approximately 10° - 15°Å similar difference was also observed for the drops placed on the second edge of the plate. One particular location on the plate (marked with a white circle in Figure 1) exhibited a considerably higher contact angle than the drops placed in other locations. Subsequent drops placed on the same location during different data sets showed a similar trend. The drops deposited at the corners of the plate (A-D) after the sixth cleaning showed a similar hysteresis variation in wettability of the surface (Figures 3-4).

The drops deposited on the channel lands were restricted by the available space and only small drops could be deposited. Contact angle variation of 10° was observed which is similar to other results.

3.2 Back Side

Drops placed on the backside of the flow field plate showed a much higher contact angle (94° - 104°) than the drops placed on the channel side of the plate. The surface appears less wetting with contact angle consistently greater than 90°.

4 Conclusion

The surface of the plate is not smooth due to the irregular present on the surface. From visual inspection it was observed that there exists dark and bright regions on the surface. This indicates some form of material inhomogeneity in the plate. The local wettability being a function of the surface chemistry as well as the roughness, a large variation in contact angle is observed.

The heterogeneity of static contact angle does not appear to be due to the surface grooves, which uniformly affect the measurement everywhere. The large variation in static contact angle likely indicates that the material composition is non-uniform. Non-uniformity of the material,

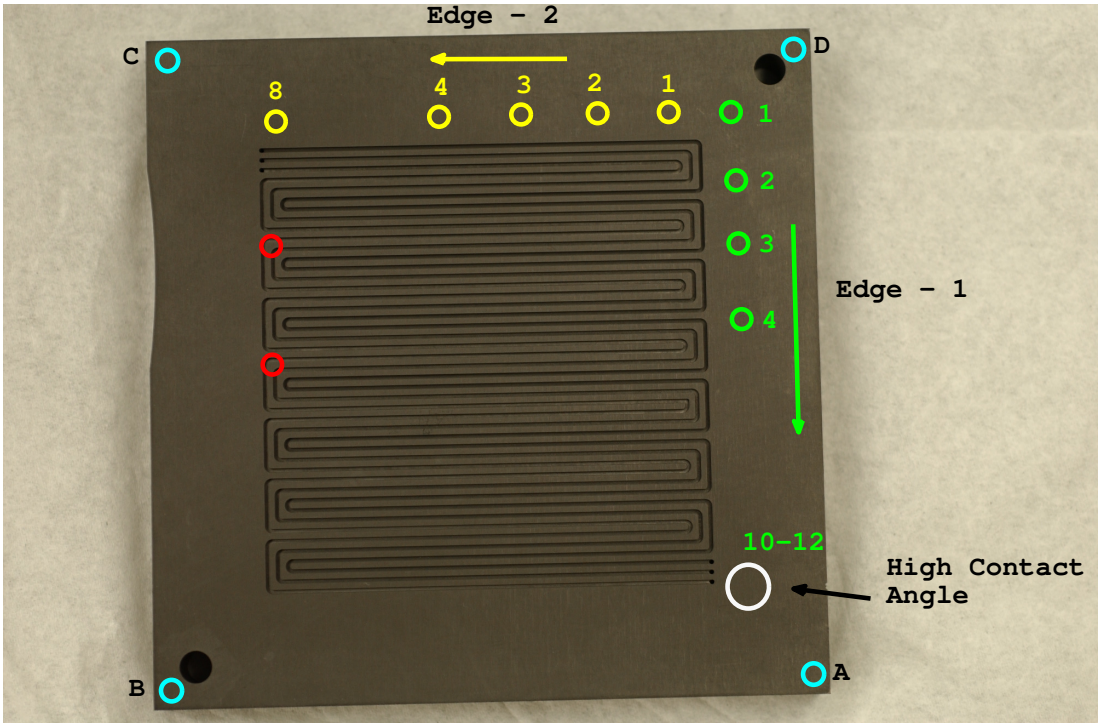

Figure 1. Drop locations on channel side of the flow field plate

resulting in large contact angle variation, could have a significant impact on the movement of liquid water through these channels during fuel cell operation.

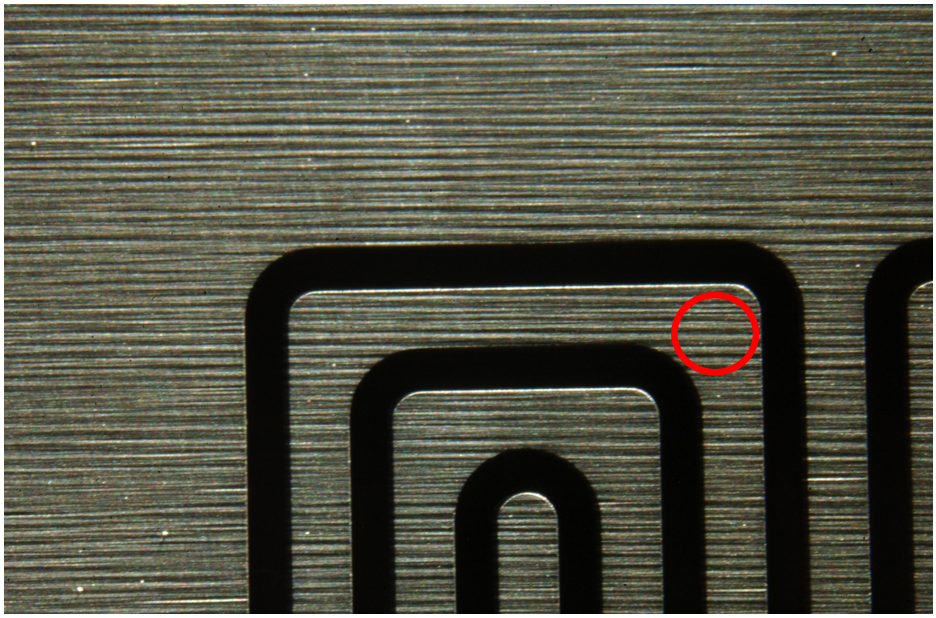

Figure 2. Drop locations on the channel lands of the plate.

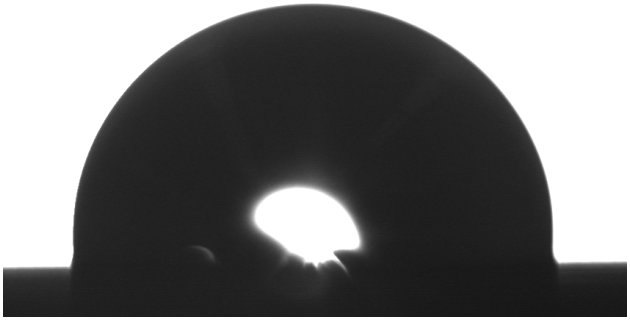

Figure 3. Image of the drop at location 'C' in Figure 1.

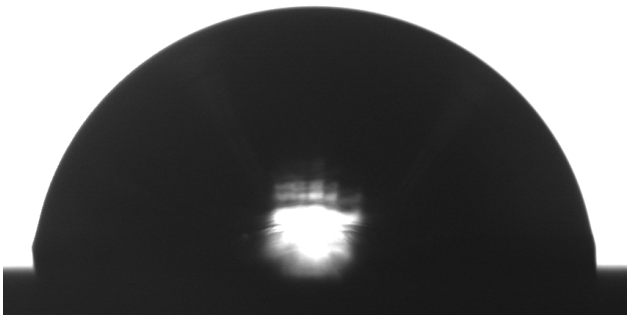

Figure 4. Image of the drop at location 'D' in Figure 1.

Table 1. Diameter of sessile drop (mm), drop volume (μl), and static contact angle (degrees) at various locations illustrated in Figure 1.

	edge 1												**edge 2**			**channel land**			**back side**		
	1st Cleaning			**2nd Cleaning**			**3rd Cleaning**			**4th Cleaning**			**4th Cleaning**			**4th Cleaning**			**5th Cleaning**		
Loc	Dia	Vol	θ	Dia	Vol	θ	Dia	Vol	θ	Dia	Vol	θ	Dia	Vol	θ	Dia	Vol	θ	Dia	Vol	θ
1	1.46	3.8	68.6	1.64	6.6	78.0	1.55	5.2	74.5	1.43	4.0	73.3	1.50	5.3	80.7	0.56	0.2	68.4	1.22	4.3	99.1
2	1.72	6.5	69.7	1.65	6.5	77.6	1.71	7.1	76.0	1.49	4.9	76.8	1.57	5.7	79.2	0.57	0.2	73.1	1.39	5.4	96.2
3	1.60	5.7	74.7	1.66	7.4	82.5	1.58	6.4	80.4	1.54	5.5	77.6	1.51	5.1	80.6	0.66	0.4	70.0	1.40	7.1	104.8
4	1.70	6.6	73.8	1.59	6.6	82.2	1.53	5.7	81.7	1.69	5.7	77.7	1.55	5.5	79.8	0.55	0.2	73.7	1.54	8.4	98.3
5	1.71	6.4	70.8	1.57	6.3	79.5	1.59	6.7	83.3	1.58	6.0	79.9	1.60	5.5	73.5	0.53	0.2	73.3	1.52	7.5	96.2
6	1.71	6.4	71.0	1.56	6.8	84.9	1.70	7.4	79.5	1.48	4.8	78.5	1.50	5.1	78.2	0.44	0.1	77.3	1.48	6.4	94.1
7	1.71	6.5	72.7	1.54	6.6	86.8	1.62	7.1	82.0	1.53	5.4	77.3	1.47	5.0	79.1	0.48	0.2	79.1	1.45	7.0	95.3
8	1.76	7.2	71.8	1.59	7.1	83.5	1.45	5.5	85.1	1.56	6.3	82.4	1.49	5.4	82.5	0.55	0.2	74.4	1.43	6.5	95.2
9	1.76	8.1	70.6	1.49	6.4	88.1	1.25	3.9	89.8	1.51	5.6	80.9				0.55	0.2	73.3	1.30	5.2	95.0
10	1.55	6.5	86.8	1.52	6.3	85.0	1.09	2.5	88.0	1.50	5.6	82.8				0.58	0.3	75.5			
11	1.70	9.1	90.6	1.46	5.6	86.0															
12	1.69	7.9	84.8																		

	corners					
	6th Cleaning					
	Grooves $\perp$ to viewing plane			**Grooves parallel to view**		
Loc	Dia	Vol	θ	Dia	Vol	θ
A	1.23	4.6	102.6	1.21	4.5	105.1
B	1.27	3.6	83.5	1.24	3.3	82.8
C	1.06	2.5	91.5	1.10	2.7	94.9
D	1.29	3.4	80.4	1.21	3.1	82.9

5 Surface Images

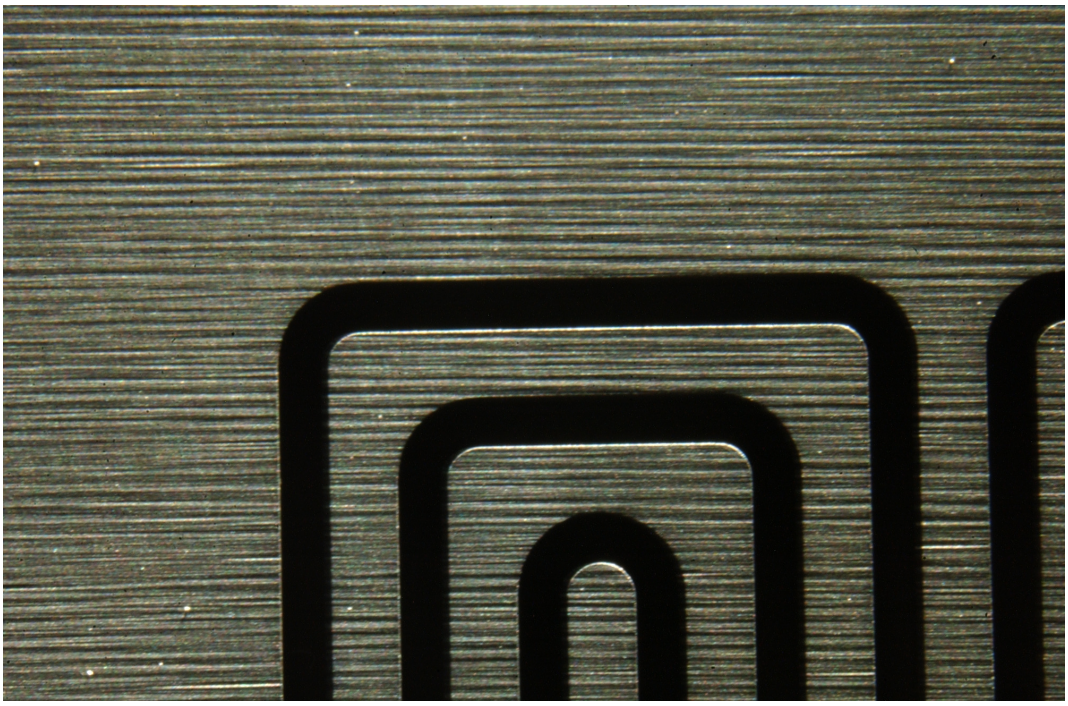

Figure 5. Channel side of the plate . . .

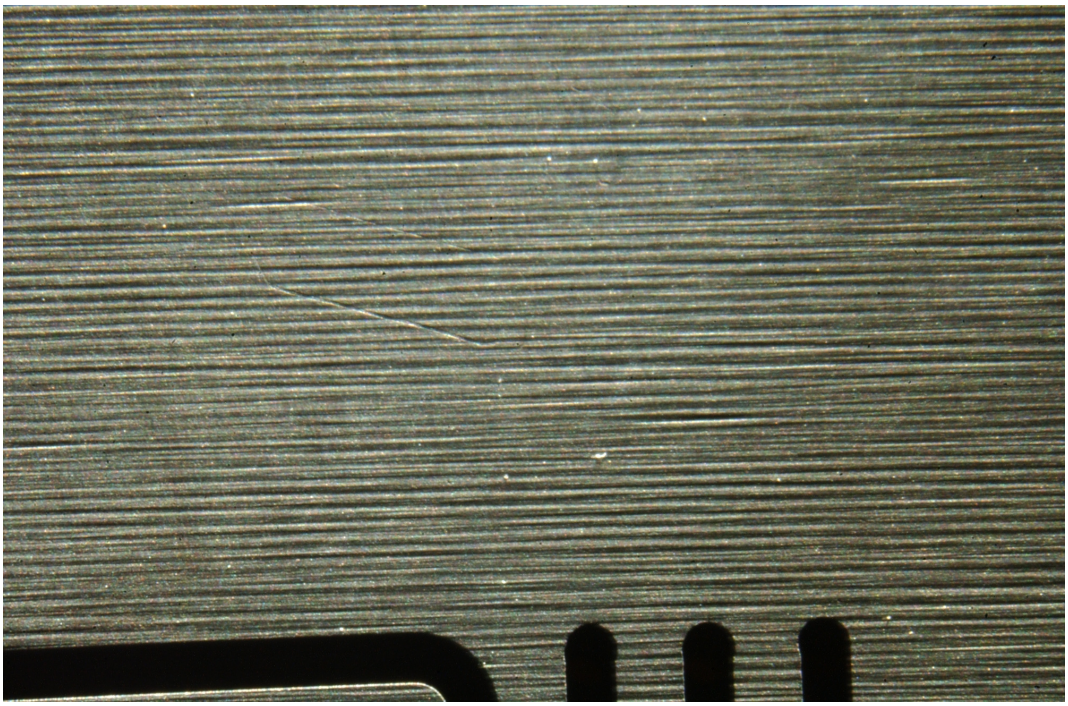

Figure 6. Channel side showing the region with higher contact angle . . .

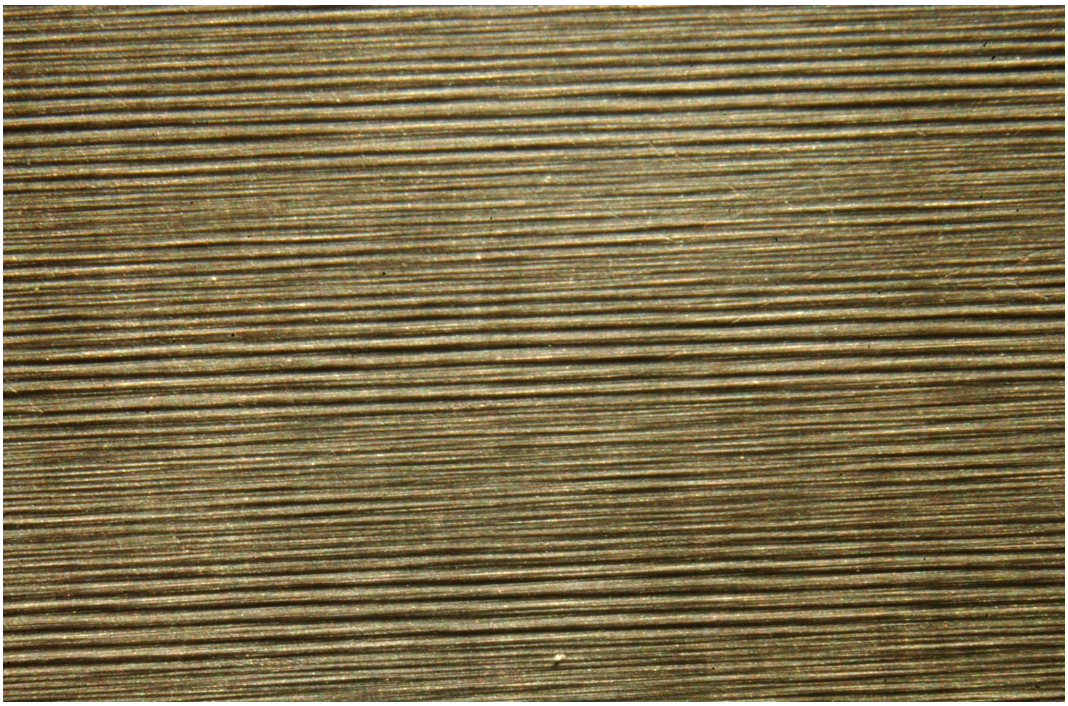

Figure 7. Back side of the plate. Alternate thick and fine grooves are visible

Static Contact Angle Measurements on AXF-5Q Part #5 Cathode Flow Field

Report Number: **NIST-2012-08-MichiganTech**

Date of Report: August 21, 2012

Contributors: J. S. Allen
V. Konduru

Contact: **Jeffrey S. Allen**
Mechanical Engineering - Engineering Mechanics
Michigan Technological University
815 R. L. Smith Building
1400 Townsend Drive
Houghton, Michigan 49931
(906) 487-2349
jstallen@mtu.edu

1 Cleaning Procedure

Four sets of contact angle data were collected on the flow field plate. The fluid used was distilled water. Before each data set, the plate was cleaned. After the plate was cleaned, it was placed in a vacuum desiccator for 30-40 minutes to allow the the plate to dry. Before the first data set, the plate was cleaned using methanol and isopropanol and was washed under running distilled water. This procedure was repeated and then the plate was dried using the Nitrogen gas. For the second data set, the plate was cleaned using methanol only. It was then washed under running distilled water and then dried with Nitrogen gas. For the third and and fourth data set, the plate was cleaned using isopropanol and distilled water and then dried with Nitrogen gas.

2 Test Method

The drops were deposited on the plate using a screw syringe and the image of the drop was captured by a long-distance microscope connected to a CCD camera. From the drop image, the drop profile is obtained. This drop profile is then fit to the theoretical drop profiles that are obtained from the Laplace-Young equation (Equation 1), which relates the pressure difference that exists across an interface to the interfacial tension and the principal radii of curvature. The theoretical profile that results in minimum error represents the ideal drop profile from which the contact angle is obtained.

$$\Delta P = \sigma \left(\frac{1}{R_1} + \frac{1}{R_2} \right) \tag{1}$$

where σ is the interfacial tension, ΔP is the pressure difference across the interface, R_1 and R_2 are the two principal radii of curvature at the apex of the drop.

In theory, a drop placed on a smooth surface is expected to be axisymmetric. However due to the rough surface of the plate, it becomes inherently difficult to obtain axisymmetric drops. To minimize the error that accompanies the asymmetry of the drops, the drops were visually inspected from the top and only the drops that appeared fairly symmetric to the naked eye were selected for contact angle measurements.

2.1 Test Locations

Drops were deposited on the channel side of the plate along two edges of the plate. 9-10 drops were deposited during each data set on each edge and an attempt was made to place the drops in the same location as the first data set. These locations are are shown in Figures 1-3. After the third cleaning, drops were also deposited on the channel lands, as shown in Figure 4. After the fourth cleaning, drops were deposited on the back side of the plate as shown in Figure 5. Drops were deposited on the two edges that corresponded to the edges on the channel side of the plate used in previous data sets.

3 Contact Angle Results

The test results are provided in Table 1. The drop diameter in mm, drop volume in μm, and static contact angle in degrees are provided. As it was not possible to precisely place drops in the same location as the first data set, the contact angle that was observed varies slightly from data set to data set.

3.1 Channel Side

The range of contact angle observed on the channel side of the plate is 90° - 104°. The mean contact angle for all the three data sets is 96°. The drops deposited on the channel lands were restricted by the available space and only small drops could be deposited. The contact angles observed on the channel lands were similar to the contact angle seen on the surface of the plate. The mean contact angle of 101° was observed on the channel lands which is marginally higher than the mean contact angle observed on the plate. This increase can be attributed to drop pinning at the edge of channel lands. The plate appears to have a uniform wettability, however, drop pinning can severely affect the wetting characteristic if the drops rest on the pores on the surface.

3.2 Back Side

Drops placed on the backside of the flow field plate resulted in contact angles of 82° - 90°with a mean contact angle of 86.5°. This is smaller the the contact angles observed on the channel side of the plate.

4 Other Observations

The surface of the plate is not smooth and pores are visible. On visual inspection, fingerprints were seen on the surface of the plate as shown in Figures 6 - 7. After multiple cleaning with methanol and isopropanol, the fingerprints could not be removed and appears permanent. This indicates careful handling is necessary to prevent contamination of the flow field plate.

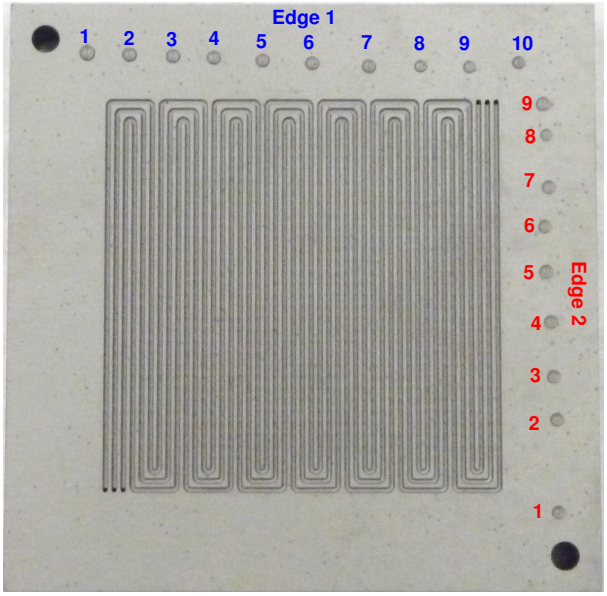

Figure 1. Drop locations on channel side of the flow field plate, Set1

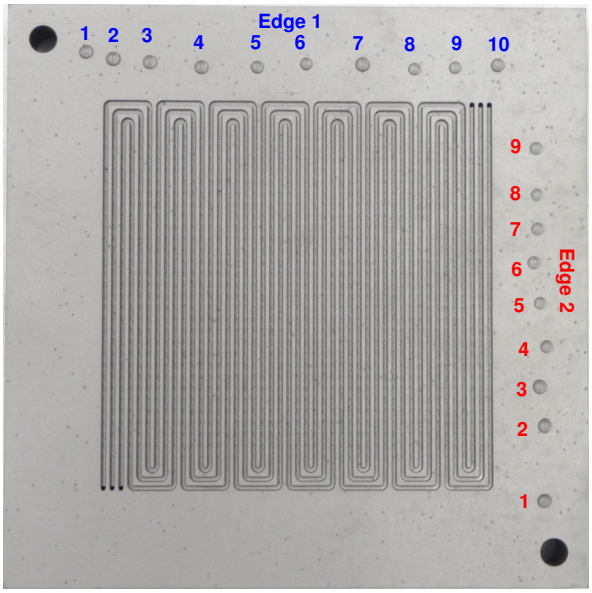

Figure 2. Drop locations on channel side of the flow field plate, Set2

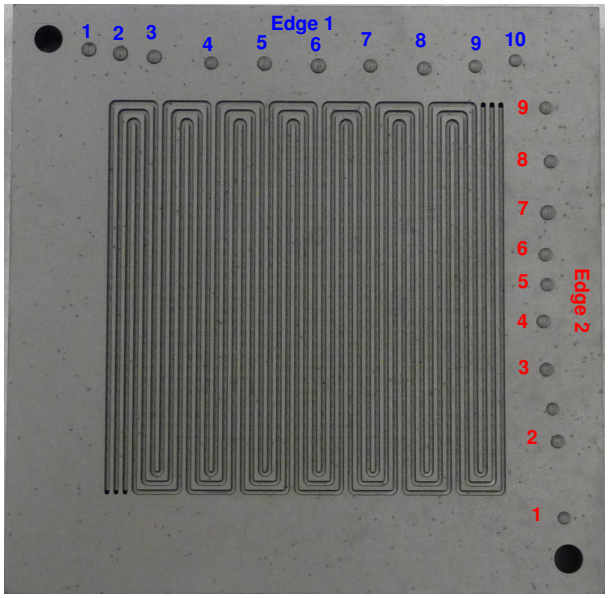

Figure 3. Drop locations on channel side of the flow field plate, Set3

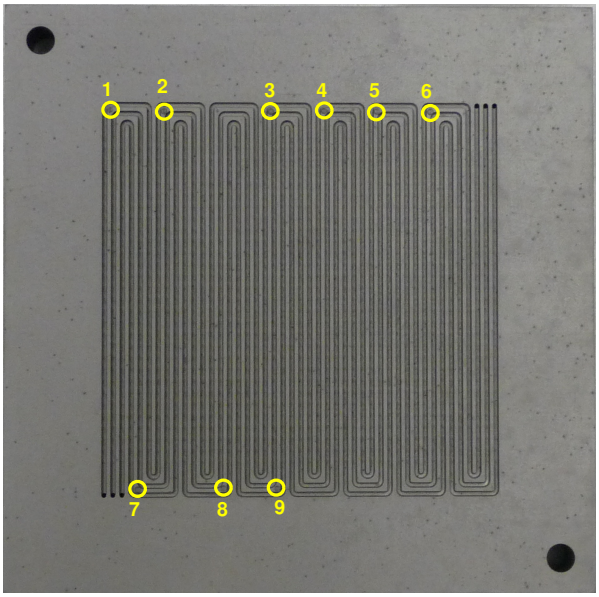

Figure 4. Drop locations on channel land of the flow field plate, Set3

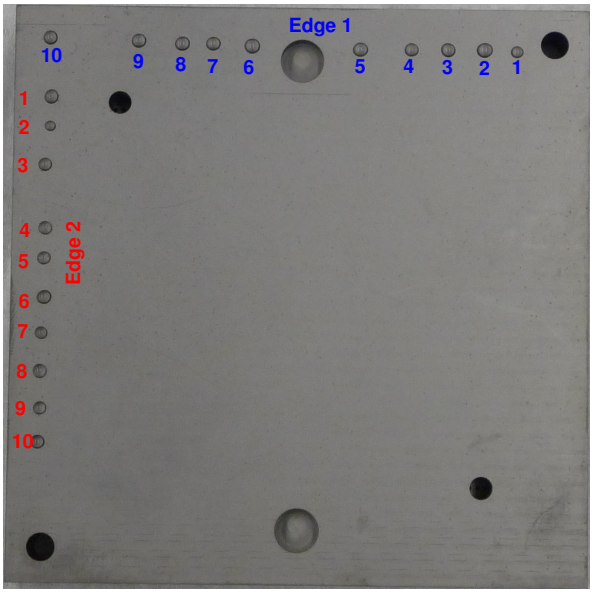

Figure 5. Drop locations on back side of the flow field plate, Set4

Table 1. Diameter of sessile drop (mm), drop volume (μl), and static contact angle (degrees) at various locations illustrated in Figure 1-5.

	1st Cleaning						2nd Cleaning						3rd Cleaning								
	Edge 1			Edge 2			Edge 1			Edge 2			Edge 1			Edge 2			Channel Land		
Loc	Dia	Vol	θ	Dia	Vol	θ	Dia	Vol	θ	Dia	Vol	θ	Dia	Vol	θ	Dia	Vol	θ	Dia	Vol	θ
1	2.68	5.6	96.0	2.19	3.5	100.6	2.44	4.3	96.5	2.44	3.7	90.4	2.61	5.2	95.4	2.21	3.4	98.1	1.19	0.6	99.0
2	2.62	4.8	91.6	2.23	3.6	99.9	2.53	4.4	94.6	2.57	4.5	93.9	2.63	4.5	90.3	2.36	4.0	95.9	0.99	0.4	102.3
3	2.53	4.5	94.5	2.25	3.7	100.4	2.49	4.8	99.0	2.60	4.4	89.3	2.66	5.0	92.5	2.22	3.3	96.4	1.04	0.4	102.1
4	2.46	4.5	97.4	2.31	3.9	99.3	2.46	4.4	96.4	2.23	3.2	96.5	2.40	3.8	94.3	2.37	4.2	98.9	0.96	0.3	105.3
5	2.45	4.1	93.4	2.42	4.3	97.7	2.28	3.4	95.0	2.17	3.1	97.2	2.56	4.6	92.7	2.40	4.0	95.1	1.06	0.4	102.6
6	2.46	4.2	94.6	2.24	3.6	99.3	2.13	3.0	98.0	2.22	3.4	97.4	2.66	5.1	92.6	2.28	3.8	99.9	1.14	0.5	98.3
7	2.43	4.1	95.4	2.38	4.0	96.7	2.60	4.5	89.3	2.22	3.6	100.5	2.49	4.2	92.4	2.35	4.1	98.5	1.04	0.4	99.6
8	2.23	3.3	95.9	2.05	2.7	96.8	2.23	3.4	97.5	2.05	3.2	104.2	2.52	4.7	96.6	2.59	5.0	96.4	1.00	0.4	103.8
9	2.19	3.2	97.4	2.44	4.2	96.2	2.23	3.4	96.8	2.20	3.5	101.7	2.29	3.5	95.2	2.40	3.9	93.3	0.91	0.3	103.7
10	2.23	3.3	96.1				2.41	3.9	94.1				2.32	3.6	94.4						

	Back Side					
	4th Cleaning					
	Edge 1			Edge 2		
Loc	Dia	Vol	θ	Dia	Vol	θ
1	2.25	2.7	86.4	2.56	3.7	84.7
2	2.85	5.1	83.4	1.83	1.6	89.9
3	2.54	3.7	86.0	2.34	3.1	88.1
4	2.49	3.8	89.3	2.39	3.6	90.9
5	2.71	4.6	85.9	2.29	3.0	88.8
6	2.76	4.6	84.4	2.43	3.1	83.1
7	2.60	3.8	83.2	2.20	2.4	84.5
8	2.63	4.0	83.7	2.49	3.7	87.8
9	2.56	3.9	86.3	2.28	2.8	87.5
10	2.49	3.5	85.1	2.40	2.8	81.1

5 Surface Images

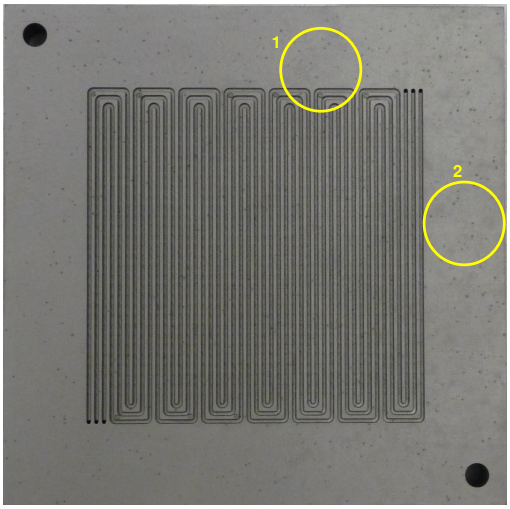

Figure 6. Visible fingerprints on channel side of the plate ...

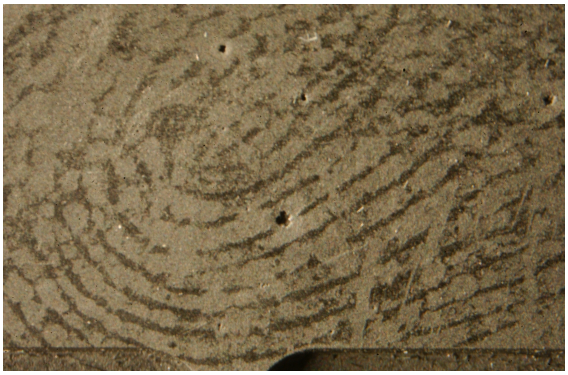

Figure 7. Magnified view of fingerprint at location 1